Frequency Response Analysis Based on Concentration Inputs for the Study and Diagnosis of Polymer Electrolyte Membrane Fuel Cells

Dissertation
zur Erlangung des akademischen Grades

Doktoringenieur
(Dr.-Ing.)

von: M. Sc. Antonio Sorrentino
geb. am: 20. Mai 1987
in: Napoli

genehmigt durch die Fakultät für Verfahrens- und Systemtechnik der Otto-von-Guericke-Universität Magdeburg

Promotionskommission: Prof. Dr.-Ing. Frank Beyrau (Vorsitz)
          Prof. Dr.-Ing. Kai Sundmacher (Gutachter)
          Prof. Dr.-Ing. Wolfgang Bessler (Gutachter)
          Prof. Dr. Fabio La Mantia (Gutachter)

eingereicht am: 7. Januar 2021
Promotionskolloquium am: 16. Juli 2021

Zusammenfassung

Polymer-Elektrolyt Brennstoffzellen (PEMFC) gelten als eine der vielversprechendsten sauberen Alternativen zum Verbrennungsmotor. Die Leistungsfähigkeit und die Lebensdauer müssen jedoch erheblich verbessert werden, um PEMFC auf dem Markt wettbewerbsfähig zu machen.

Eine übermäßige Anwendung von PEMFCs kann zu fehlerhaften Zuständen und Degradationsmechanismen führen, die zu einer irreversiblen Senkung der Leistung und einer Verringerung der Zelllebensdauer führen. Um Minderungsstrategien zu entwickeln, die es ermöglichen, den hieraus resultierenden Materialabbau der verschiedenen Zellkomponenten zu begrenzen und die Lebensdauer zu verlängern, sind effiziente Diagnosewerkzeuge erforderlich, die in der Lage sind, fehlerhafte Bedingungen zu erkennen.

In dieser Arbeit wurde eine neuartige Frequenzganganalyse als Alternative zur elektrochemischen Impedanzspektroskopie (EIS) auf Basis von Partialdruckänderungen als Eingangssignal zur Untersuchung der Polymerelektrolytmembran Brennstoffzellen (PEMFC) entwickelt. Ziel war es, die Beschränkungen der EIS in Bezug auf die Identifizierung und Diagnose von PEMFCs zu überwinden. EIS scheitert häufig beim Trennen der Beiträge verschiedener Prozesse aufgrund der Kopplung der Auswirkungen verschiedener dynamischer Phänomene mit ähnlichen Zeitkonstanten in den Spektren. Die vorgeschlagene Technik, die als konzentrationsalternierende Frequenzgangsanalyse (abgekürzt CFRA) bezeichnet wird, impliziert die Anregung der PEMFC durch Materialzufuhr, welche durch einen periodischen Partialdruck eines oder mehrerer gasförmiger Reagenzien in verschiedenen Frequenzen gekennzeichnet ist. Die erhaltene elektrische Leistung, Strom oder Spannung, hängt von der auf die Brennstoffzelle angewendeten Regelung ab, voltastatisch oder galvanostatisch.

Nach der Theorie linearer Systeme könnte die Auswirkung im Zusammenhang mit einem dynamischen Verfahren durch die Änderung der Art des Inputs und/oder Outputs besser beobachtbar oder nachweisbar sein, was zu selektiverer Information in der Übertragungsfunktion führen könnte. Daher bestand die Hauptmotivation für die Anwendung partieller Druckeingänge darin, die Möglichkeit zu prüfen, selektive Anteile sich überlappender Phänomene auf PEMFC-Leistungsverluste zu messen, welche in EIS-Spektren an andere Beiträge gekoppelt oder überhaupt nicht erkannt würden. In einem ersten Schritt wurde die Fähigkeit der CFRA theoretisch mit Hilfe eines eindimensionalen dynamischen PEMFC Modells untersucht. Berücksichtigt wurden

dabei die wichtigsten physikalisch-chemischen Prozesse, welche das transiente Verhalten beeinflussen. Hierfür wurden CFRA-Spektren für Sauerstoff- und Wasserpartialdruck Inputs unter galvanostatischen und voltastatischen Bedingungen der Brennstoffzelle berechnet. Die Fähigkeit von CFRA, selektiv nur spezifische Dynamiken in Abhängigkeit von der verwendeten Ein-/Ausgangskonfiguration zu erkennen, konnte bestätigt werden.

Übertragungsfunktionen mit Sauerstoffpartialdruckschwingungen als Eingangssignal unter galvanischer Steuerung enthielten nur Dynamiken im Zusammenhang mit dem Massentransport des Sauerstoffs innerhalb des Kanals. Gegensätzlich hierzu, wurden zusätzliche Dynamiken der Wassersorption in die Nafion-Membran im Spektrum im voltastatischen Zustand beobachtet. Beide experimentellen Techniken waren unsensibel auf die Dynamik des Ladens und Entladens der Doppelschicht und alle anderen Phänomene mit Zeitkonstanten niedriger als der Transport von Gas im Kanal. Zusätzlich stiegen die Größen der Übertragungsfunktionen mit der Erhöhung des Massentransportwiderstands. Auf Grund dieser Besonderheit eignet sich die CFRA mit Sauerstoffpartialdruckschwingungen als Eingangssignal für die Bewertung des Einflusses von Wasserakkumulation in der Kathode.

Die CFRA-Übertragungsfunktionen, bestimmt durch die Anwendung von Wasserpartialdruckschwingungen als Input, wurden hauptsächlich durch die Dynamik im Zusammenhang mit der Wassersorption in der Nafion-Membran beeinflusst. Darüber hinaus macht die Proportionalität zwischen dem Wassergehalt in der Membran und der Größe der Übertragungsfunktionen die CFRA mit Wasserpartialdruckschwingungen zu einem Instrument, das zur Bestimmung der Austrocknung des Elektrolyten anwendbar ist.

Anschließend wurde eine Identifizierbarkeitsanalyse hinsichtlich der wichtigsten Parameter durchgeführt, welche die Leistung der Brennstoffzelle beeinflussen. Es wurde gezeigt, dass mittels CFRA eine zuverlässigere Parameterschätzung durchführt werden kann als mit der EIS. In diesem Zusammenhang zeigten die durch die Anwendung von Wasserpartialdruckschwingungen als Eingangssignal durchgeführten CFRAs die besten Leistungen, womit diese sich als die bestgeeignete Methode für die Anwendung als Onboard-Diagnosetool herausstellte.

Um die theoretischen Ergebnisse zu validieren, wurde ein Versuchsaufbau entwickelt, der in der Lage ist, gleichzeitige periodische Schwingungen von Sauerstoff- und Wasserpartialdruck zu erzeugen, um CFRA-Experimente durchzuführen. Es wurde ein experimentelles Protokoll zur Analyse der gesammelten Daten und zur Bestimmung der CFRA-Übertragungsfunktionen im Frequenzbereich erstellt.

Anschließend wurden CFRA-Spektren mit Hilfe des Versuchsaufbaus und des hierfür etablierten Verfahrens experimentell unter den gleichen stationären Bedingungen gemessen, die auch in der theoretischen Studie zuvor angenommen wurden. Die CFRA-Spektren, die durch die Verwendung von Sauerstoffpartialdruckschwingungen gewonnen wurden, spiegelten alle in den theoretischen Ergebnissen beobachteten Merkmale wider und bestätigten die Fähigkeit, die Dynamik des Massentransports im Kanal selektiv detektieren zu können. Die Verwendung von Wasserpartialdruckschwingun-

gen als Eingangssignal ermöglichte hauptsächlich die Dynamik der Wassersorption im Nafion zu erkennen, wie bereits in den Simulationen beobachtet wurde. Alle bestimmten CFRA-Spektren zeigten jedoch Muster bei höheren Frequenzen, die nicht vorhergesagt wurden. Es wird angenommen, dass diese Merkmale auf Phänomene zurückzuführen sind, die im Modell nicht berücksichtigt wurden. Als mögliche Erklärungen wurden insbesondere der Transport von flüssigem Wasser in der Kathode und Resonanzphänomene identifiziert. Die letztgenannte Hypothese wurde durch Simulationen unterstützt, die mit einem vereinfachten PEMFC-Kanalmodell durchgeführt wurden.

Die Zuverlässigkeit der Parameterschätzung, die durch die Anpassung eines einzelnen CFRA- sowie EIS-Spektrums an das Modell erzielt wurde, konnte anschließend verglichen werden, um die am besten geeignete Frequenzgangtechnik zu ermitteln, welche in modellbasierten Onboard-Diagnosewerkzeugen angewendet werden sollte. Hierzu wurde die Identifizierbarkeitsanalyse auf Basis des gleichen Konzepts der theoretischen Studie zuvor und unter Berücksichtigung der Einstellungen in den Experimenten wiederholt. Es wurde festgestellt, dass der Ladungstransferkoeffizient und Diffusionskoeffizient von Sauerstoff nicht korrekt zusammen geschätzt werden können, da sie in allen Fällen stark korreliert sind. Allerdings wurden die durch die Verwendung von Wasserpartialdruckschwingungen durchgeführten CFRA als die zuverlässigste Technik für die Parameterschätzung bestätigt.

Anschließend wurde das Konzept der gekoppelten Übertragungsfunktion weiterentwickelt, das als lineare Kombination von CFRA-Übertragungsfunktionen beider Partialdruckschwingungen als Input definiert ist. Aufgrund der unterschiedlichen qualitativen Form der Spektren in Abhängigkeit von der Befeuchtung des Mediums in die Brennstoffzelle, konnten die gekoppelten Übertragungsfunktionen als hilfreich bei der Detektion des Austrocknens der Membran aufgrund von Fehlfunktionen externer Befeuchtungssysteme identifiziert werden.

Schlussfolgernd hat sich die CFRA als experimentelle Technik erwiesen, welche die EIS ergänzt und in der Lage ist, die Beiträge des Gastransports und der Wassersorption in Nafion von der Gesamtleistung zu unterscheiden. Diese Merkmale sind ein vielversprechendes Instrument für Onboard-Diagnosetools, um die Mehrdeutigkeit der EIS zu überwinden.

Summary

Polymer electrolyte fuel cells (PEMFCs) are considered as one of the most promising clean alternatives to replace the combustion engine. However, their efficiency and durability need to be significantly improved to make PEMFCs competitive in the market.

The prolonged use of PEMFCs exposes them to several faulty conditions that enhance degradation mechanisms and lead to irreversible loss of performance and decreased lifetime. Therefore, efficient diagnostic tools are required in order to identify these faulty conditions and develop respective mitigation strategies.

In this thesis, a novel frequency response analysis was developed to study PEMFC dynamics. The analysis is based on concentration inputs as an alternative, yet conceptually similar approach to conventional electrochemical impedance spectroscopy (EIS), and aims to overcome the limitations of the latter with respect to PEMFC diagnosis. EIS often fails to separate the contributions of different processes due to the coupling in the spectra of the effects of dynamic phenomena with similar time constants. The proposed technique, named concentration-alternating frequency response analysis (abbreviated CFRA), utilizes periodic inputs of partial pressure of one or more feed components at different frequencies to probe PEMFC dynamics. The electric output obtained, current or voltage, depends on the control regime applied to the fuel cell which would be respectively voltastatic or galvanostatic.

According to the linear system theory, by changing the type of input and/or output, the impact related to a specific dynamic process could be more detectable than others leading to more selective information contained in the transfer function. Following this principle, the primary motivation of using partial pressure inputs was to verify the possibility to separate the contributions of overlapping dynamic processes to PEMFC performance losses which would be coupled to other ones in EIS spectra or not detected at all.

As a first step, the capabilities of CFRA were theoretically investigated with the help of one-dimensional dynamic model, spatially distributed along the sandwich coordinate and including the main physico-chemical processes that determine the transient performance. As a result, theoretical CFRA spectra for oxygen and water partial pressure inputs under galvanostatic and voltastatic conditions were calculated and the capability for selective detection of individual dynamics was confirmed. The transfer functions based on oxygen pressure input under galvanostatic conditions contained

only dynamics related to the mass transport of the oxygen inside the channel. On the contrary, the water sorption dynamics in Nafion membrane was observed under voltastatic operations. Both experimental techniques were insensitive to the dynamics of double layer charging or any other phenomena with time constants lower than the gas transport in the channel. Additionally, the transfer function magnitudes increased with the mass transport resistance. This feature makes CFRA by oxygen pressure inputs suitable for the evaluation of cathode flooding.

On the other side, CFRA transfer functions based on water pressure inputs were predominantly influenced by the dynamics related to water sorption in Nafion. Furthermore, the proportionality between the water content in the membrane and the magnitude of the transfer functions under galvanostatic conditions makes CFRA by water pressure perturbations useful to gauge electrolyte dehydration.

Finally, an identifiability analysis was performed which confirmed that CFRA offered a more reliable parameter estimation than EIS. In particular, CFRA based on water pressure perturbations showed the best performance with respect to parameter estimation, which makes this method the most suitable for application as onboard diagnostic tool among the others.

In order to validate the theoretical findings, an experimental setup producing simultaneous periodic perturbations of oxygen and water pressure was developed, alongside a protocol for data analysis and determination of CFRA transfer functions.

Then, using the setup and the established experimental procedure, CFRA spectra were experimentally determined. The CFRA spectra obtained by using oxygen pressure inputs agree well with the theoretical ones, confirming the theoretically predicted capability to detect selectively the gas transport dynamics in the channel. On the other hand, the use of water pressure inputs allowed to detect mostly the dynamics of water sorption in Nafion, as likewise observed in simulations. However, all the collected CFRA spectra showed patterns at higher frequencies which were not seen in the simulations. These features were assumed to be due to phenomena that were not accounted in the model. In this context, the transport of liquid water on the cathode side and resonance phenomena were discussed as possible contribution. The latter hypothesis was supported by simulations of a a simplified PEMFC channel model spatially distributed along the axial coordinate.

The reliability of the estimation by fitting CFRA and EIS spectra with the model was compared in order to determine the most suitable frequency response technique for model-based onboard diagnostic tools. For this, the identifiability analysis from the theoretical study was adjusted considering the experimental settings and repeated. It was found that the charge transfer coefficient and oxygen effective diffusivity cannot be estimated correctly together because they were extremely correlated in all the cases. On the other hand, CFRAs performed by using water pressure perturbations were confirmed to be most reliable techniques for parameter estimation.

Finally, the concept of coupled transfer function was advanced, defined as a linear combination of CFRA transfer functions obtained by two simultaneous partial pressure inputs. Due to the different qualitative shape of the spectra depending on the humid-

ification of the fuel cell feed, the coupled transfer functions were found to be helpful in the detection of drying out of the membrane caused by malfunctioning of external humidification systems.

To conclude, CFRA proved to be highly useful experimental technique complementary to EIS capable to discriminate the contributions of gas transport and water sorption in Nafion from the overall performance. These features candidate it as a promising onboard diagnostic tool, overcoming the ambiguities of EIS.

Preface

In the context of this dissertation, five articles were published, which are partially included in the manuscript. The chapters containing parts of these articles are listed in the following.

- An extensive review of the main degradation mechanisms and faulty states of polymer electrolyte membrane fuel cells (PEMFC) was performed in Sorrentino et al. [1]. A reduced version of this work is presented in the Chapter 2.

- Several frequency response analysis methodologies based on nonelectrical inputs and/or outputs employed to diagnose PEMFCs were reviewed in Sorrentino et al. [1]. In the same article, a mathematical framework rooted in linear system theory to evaluate systematically the sensitivity of a general transfer function to parameters related to certain processes is introduced. This work is partially presented in the Chapter 3.

- A theoretical analysis investigating the capabilities of the concentration-alternating frequency response analysis (CFRA) as novel diagnostic tool for PEMFCs is presented in the Chapter 4. Part of the results shown in this study together with the developed model were published in Sorrentino et al. [2].

- In the Chapter 5, a detailed description of the experimental setup and protocol designed to perform CFRA experiments and determine the spectra in frequency domain is presented. Part of this chapter was discussed in Sorrentino et al [3] and Sorrentino et al. [4].

- The experimental validation of the theoretical results is discussed in the Chapter 6. The same findings are reported in Sorrentino et al. [4].

- The concept of coupled CFRA transfer function is introduced in the Chapter 7 together with an experimental and model based analysis of the related spectra. All the results shown in this chapter were reported in Sorrentino et al. [5].

[1] A. Sorrentino, K. Sundmacher, and T. Vidakovic−Koch. Polymer electrolyte fuel cell degradation mechanisms and their diagnosis by frequency response analysis methods: a review. *Energy*, 13(21):5825, 2020.

[2] A. Sorrentino, T. Vidakovic−Koch, R. Hanke−Rauschenbach, and K. Sundmacher. Concentration−alternating frequency response: A new method for studying polymer electrolyte membrane fuel cell dynamics. *Electrochimica Acta*, 243:53−64, 2017.

[3] A. Sorrentino, K. Sundmacher, and T. Vidakovic−Koch. Guide to concentration alternating frequency response analysis of fuel cells. *Journal of Visualized Experiments*, 154(1−2):e60129, 2019.

[4] A. Sorrentino, K. Sundmacher, and T. Vidakovic−Koch. Decoupling PEMFC dynamics through frequency response analysis based on concentration inputs. *Electrochimica Acta*, 390:53, 2021.

[5] A. Sorrentino, T. Vidakovic−Koch, and K. Sundmacher. Studying mass transport dynamics in polymer electrolyte membrane fuel cells using concentration−alternating frequency response analysis. *Journal of Power Sources*, 412:331−335, 2019.

Contents

Abbreviations

AC	Alternating current
BC	Boundary conditions
CFRA	Concentration-alternating frequency response analysis
DAE	Differential algebraic equations
DEA	Dead end anode
EC	Equivalent circuits
ECSA	Electrochemically-active surface area
EHD	Electro-hydrodynamic
EIS	Electrochemical impedance spectroscopy
EPIS	Electrochemical-pressure impedance spectroscopy
ETIS	Electrothermal impedance spectroscopy
FDI	Fault detection and isolation
FRA	Frequency response analysis
FTA	Flow through anode
GDL	Gas diffusion layer
HCA	Hydrogen circulation anode
HEA	Hydrogen ejector anode
HECII	Hydro-electrochemical impedance imaging
HOR	Hydrogen oxidation reaction
LIT	Lock-in thermography
LST	Linear system theory
MEA	Membran electrode assembly
MISO	Multiple input single output
PDE	Partial differential equation
PEMFC	Polymer electrolyte fuel cell
PTFE	Polytetrafluorethylen
ODE	Ordinary differential equations
ORR	Oxygen reduction reaction
PI	Photo-electrochemical impedance
RH	Relative humidity
SISO	Single input single output
TI	Thermo-electrochemical impedance

Symbols

Latin

ai_0	Product of specific catalyst area and current density	A m^{-2}
A	State space matrix	-
A_{cell}	Area of the electrode	m^2
B	Controllability matrix	-
C	Observability matrix	-
C_α	Concentration	mol m^{-3}
C^{DL}	Double layer capacity	F m^{-2}
D	Transmission matrix	-
D_α	Diffusivity coefficient	m^2 s^{-1}
E	Voltage	V
F	Faraday constant	C mol^{-1}
F_i	Generic state function	-
$F_{\alpha,in}$	Inlet volumetric flow rate	m^3 s^{-1}
$F_{\alpha,out}$	Outlet volumetric flow rate	m^3 s^{-1}
G_i	Nonlinear output function	-
j	Current density	A m^{-2}
J_α	Diffusive flux	mol m^2 s^{-1}
$K_{H2,ad}$	Hydrogen adsorption constant	Pa
$K_{H,ox}$	Hydrogen oxidation constant	mol m^{-2} s^{-1}
K_{H+}	Electroosmotic drag constant	-
H	Generic transfer function	-
H^{CH}	Channel height	-
i	Imaginary unit	
I	Total current	A
I_n	Identity matrix	-
L	Observation error vector	-
L^{CH}	Channel length	-
L_{setup}	Length tube in CFRA setup	-
L_{step}	Length transition region	m
m_{EW}	Molecular weight of Nafion	Kg m^{-3}
N_w	Water flux through the membrane	mol m^{-2} s^{-1}

O	Observation vector	-
P	Matrix of right eigenvalues	-
P_α	Partial pressure	Pa
P_{tot}	Total pressure	Pa
Q	Matrix of left eigenvalues	-
r	Radius of the tube	M
r_i	Residual	-
r_{HOR}	Reaction rate of hydrogen oxidation reaction	mol m^{-2} s^{-1}
r_{ORR}	Reaction rate of oxygen reduction reaction	mol m^{-2} s^{-1}
R	Universal gas constant	mol J^{-1} K^{-1}
S	Transfer function of the oxygen sensor	-
S_p	Sensitivity matrix	-
t	Time	s
t^{CL}	Catalyst layer thickness	m
$\bar{u}$	Gas average velocity	m s^{-1}
V	Volume of the channel	m^3
W	Input vector	
W^{CH}	Channel width	
x	Sandwich coordinate	m
X	State variables vector	
y	Axial coordinate	m
y_α	Molar fraction	-
Y	Input vector	-

Greek

α	Charge transfer coefficient	-
β	Normal input matrix	-
γ	Normal output matrix	-
ε	Porosity	-
ζ_E	Voltastic CFRA transfer function	A Pa^{-1}
ζ_I	Galvanostatic CFRA transfer function	V Pa^{-1}
ζ_E'	Coupled voltastic CFRA transfer function	A Pa^{-1}
ζ_I'	Coupled galvanostatic CFRA transfer function	V Pa^{-1}
η	Overpotential	V
θ_i	Generic parameter	-
κ_{H^+}	Proton conductivity in Nafion	S m^{-1}
$\lambda_{H_2O}^M$	Water content in Nafion	-
λ_i	Eigenvalue	-
Λ_i	Diagonal eigenvalues matrix	-
ξ	Electroosmotic drag force	-
ρ_{EW}	Density Nafion	kg m^{-3}

ω	Angular frequency	Hz
τ	Time constant	Hz
τ_t	Tortuosity factor	-
ϕ	Simulation vector	-
ϕ_α	Adimensional dispersion coefficient	-
Φ	Ohmic voltage loss	V

Superscripts

0	Nominal value	
a	Anode	
c	Cathode	
CH	Channel	
CL	Catalyst layer	
DL	Double layer	
eff	Effective value	
GDL	Gas diffusion layer	
M	Nafion membrane	

Subscripts

c	Critical value
$diff$	Parameter related to diffusion process
dp	Dew point value
el	Electric quantity
hyd	Hydraulic flux
HOR	Hydrogen oxidation reaction
i	Index
in	Inlet
j	Index
k	Index
kin	Kinetic parameter
K	Parameters subset
m	Index
n	Index
ORR	Oxygen oxidation reaction
out	Outlet
ref	Reference value
$step$	Quantity related to step experiments
w	Water
α	General component
Ω	Interface

Chapter 1

Introduction

It is widely accepted that global warming is caused by CO_2 emissions and that their reduction is mandatory in order to mitigate it. Considering that almost 23% of the CO_2 emissions is due to the transportation sector [1], the development of vehicles based on zero CO_2 emission technologies will be crucial for the development of a decarbonized society. In this respect, polymer electrolyte fuel cells (PEMFC) are being targeted as one of the most promising clean alternative to replace the internal combustion engine. Aside from their high efficiency, zero emissions and silent operations, the main reasons which make PEMFC more attractive than lithium ions battery systems for the automotive sector are the higher power densities, fast start up times, capability of covering larger driving distances (> 450 Km), fuel refueling in few minutes and the possibility to be inserted in a more sustainable hydrogen economy cycle [2]. Because of these features, they have found early niche applications in forklift trucks, remote back/up power and fuel cell bus deployment which are expanding in the last years. Moreover, a substantial improvement of the energy density and reduction of costs due to material improvements and enlargement of infrastructures is expected in the years to come with respect to other technologies. However, efficiency and operating life will need to be significantly improved to make PEMFC competitive in the market.

The working principles of PEMFCs are described in detail in the literature [3, 4] and are therefore here not repeated. The performance losses in PEMFCs are mainly related to specific dynamic processes occurring within the cell during operations. The most influential are: (i) mass transport of oxygen in the cathode flow fields and catalyst layer, (ii) charging of the double layer taking place in parallel with faradaic reactions at the catalyst interface, (iii) sorption of water in the Nafion membrane. They determine concentration polarization losses, charge transfer resistance and ohmic resistance of the cell respectively. The impact of all these phenomena on the global performance highly depends on the parameters related to the structural properties of the cell materials, as well as on the operating conditions. The prolonged use of PEMFCs exposes these components to several degradation mechanisms which lead to irreversible lowering of the performance and decrease of the cell lifetime. Most commonly degradation leads to: (i) loss of active catalyst area, (ii) membrane thinning, (iii) loss of hydropho-

bicity of the gas diffusion layer (GDL), (iv) mechanical failure of the membrane. Degradation is accelerated by operation under faulty conditions like: (i) flooding of the electrodes, (ii) dehydration of the Nafion membrane, (iii) reactants starvation, (iv) presence of impurities in the fuel or oxidant feeds. Therefore, a deep understanding of the dynamic processes governing each of these faulty states is necessary in order to develop mitigation strategies able to limit material degradation and prolong the cell lifetime. This can succeed only upon developing efficient diagnostic tools capable to identify the contribution of specific processes to the PEMFC performance.

Frequency response analysis (FRA) techniques have been used successfully to separate different phenomena acting in parallel and to evaluate their individual contributions to the total efficiency losses. Electrochemical impedance spectroscopy (EIS) is the most commonly used frequency response methodology applied to PEMFC. It consists of exciting the cell by a sinusoidal electric input (current or cell potential) at different frequencies, measuring the complementary electric output, and analyzing the input/output correlation by the means of linear system theory (LST). However, EIS often fails to separate the contribution of different phenomena due to the coupling in the frequency spectra of dynamic processes with similar time constants. For this reason, in many instances, it is difficult to identify the mechanism which dominates the performance of PEMFCs through EIS. In the last years, for the study of different electrochemical systems, it has been proposed that the use of specific nonelectrical inputs instead of electrical ones could generate a response containing only the the contributions of a single or few specific processes, minimizing the coupling issues. Based on this, several other FRA techniques for electrochemical studies have been proposed. Recently, the first successful applications of this concept have been developed for PEMFC systems using, among others, back pressure and flow field temperature as inputs [5,6].

Following this strategy, the aim of this thesis was the development of a FRA technique alternative to EIS, based on concentration inputs for the study and diagnosis of PEMFC. The novel methodology, named concentration-alternating frequency response analysis (CFRA), consists of the application of a feed to the cell characterized by a periodic concentration of one or more reactants. A periodic current or voltage is obtained as output depending on the electric control applied to the cell, respectively voltastatic or galvanostatic. Transfer functions based on the used input/output configuration were formulated by the same means used for EIS. Specifically, perturbation of oxygen and water partial pressures sent to the cathode side of the cell were employed as input, since the processes contributing to most of PEMFC losses are acting on this part of the cell which is characterized by a sluggish electrochemical reaction. Our expectations, supported by the theory, were that the use of oxygen and water pressure as inputs could selectively detect and extract the contribution of the gas mass transport dynamics and water transport in the GDL and in the membrane, in order to get an indication of specific faulty conditions and reversible performance losses related to these processes.

The manuscript is organized according to the following structure. At first, the main

degradation mechanisms are described in relation to the faulty states enhancing them (Chapter 2). Then, a brief review of the most used diagnostic techniques for the study of PEMFC and fault identification is conducted with a detailed focus on the EIS. The ambiguities on the interpretation of the patterns observed in the EIS, which are especially verified in the low frequency part of the spectra (f< 1 Hz), and its limits as diagnostic tool are discussed. Afterwards, the state of art of FRA methodologies based on nonelectrical input and/or outputs is discussed with a particular attention to the novel ones applied to PEMFC (Chapter 3). Additionally, a general mathematical framework based on LST is formulated in order to asses the quantification of information contained in a general transfer function related to a certain input/output configuration, and evaluate the possibility to study specific dynamic phenomena. The results of a theoretical study to investigate the capability of the CFRA as diagnostic tool for PEMFC are presented in the Chapter 4. At first, a one dimensional model of a PEMFC containing all the main physico-chemical processes influencing the dynamics was formulated and validated by classic EIS spectra. Then, CFRA experiments were simulated confirming the possibility to evaluate separately the contribution of different dynamic processes, otherwise coupled in the EIS spectra, on the fuel cell performance also with the help of the developed mathematical framework. Additionally, a sensitivity analysis was performed in order to evaluate the reliability of the parameter estimated through model fitting of the spectra of the different FRA techniques. In order to validate the theoretical results, a setup capable to produce a feed with simultaneous periodic pressure of oxygen and water has been developed to perform CFRA experiments. The obtained results are discussed in detail in the Chapter 5. A procedure to process the collected data by the means of spectral analysis together with a protocol to evaluate the individual contribution to the electric response of the double concentration inputs was defined in order to determine the CFRA transfer function. Subsequently, this procedure was applied to validate the theoretical results (Chapter 6). CFRA spectra were measured at different steady state conditions showing the predicted skill to separate contributions of phenomena like oxygen mass transport and sorption of water in the membrane. However, discrepancies with the simulations were also observed at higher frequencies. Possible processes that led to these patterns are discussed. Moreover, the quality of the parameter estimation performed by fitting a single CFRA and EIS spectrum with the model was again evaluated. The purpose of this analysis was evaluating which FRA technique were the most suitable to be applied in model based on-board diagnostic tool. Finally, the concept of coupled transfer function, which is defined as a linear combination of oxygen and water CFRA transfer function is introduced in the Chapter 7. Due to their dependency on the the humidification of the cell feed, the coupled transfer functions were helpful in the detection of starvation conditions due to malfunctioning of external humidifiers. A summary of the results is given in the last part of this work.

Chapter 2

Degradation mechanisms related to faulty operating conditions of PEMFCs and their diagnosis by EIS

The prolonged use of PEMFCs exposes them to several degradation mechanisms which lower reversibly or irreversibly their performances and decrease their lifetime. The performance losses are dramatically accelerated under different operating modes and faulty conditions which are frequently occurring during many of their applications, as for example in the automotive sector. Two strategies are generally adopted in order to mitigate the effects of such harmful operating conditions: (i) the synthesis of more durable materials and cell designs, (ii) the development of real time diagnostic tools integrated in control systems enabling to minimize the faulty states.

In this chapter, different degradation mechanisms in relation to the faulty states enhancing them are described (Section 2.1). Then, a brief review of the use of the EIS for characterization and diagnostic of PEMFCs is presented in Section 2.2. The current ambiguities in the interpretation of the patterns observed in the EIS spectra and its limits as diagnostic tool are discussed.

2.1 Faulty states and degradation mechanisms

The most relevant faulty states for stationary and mobile applications of PEMFCs include poor water management which results in the phenomena of flooding and dehydration, reactants starvation, and presence of contaminants in the fuel and in the oxidant streams. The relations between these detrimental operating conditions, the various type of degradation and their effects are depicted in the Figure 2.1. Following this scheme, an overview of the irreversible degradation mechanisms with respect to the faulty states enhancing them is presented in this section.

Irrreversible degradations:

Degradation mechanisms:

Effects:

Faulty conditions:

Thermal Ostwald ripening

Proton reduction reaction

Electrochemical Ostwald ripening

Loss of ECSA

Flooding

Platinum dissolution

Catalyst thinning

Increment of electronic resistance

Dehydration

Carbon corrosion

Catalyst particle detachment

Lowering of the mechanical strength of the catalyst

Starvation

Radicals and peroxide attack on Nafion

Membrane thinning

Lowering of the mechanical strength of the membrane

Presence of contaminants in the feed

Adsorption impurities on the catalytic sites

Pinholes formation

Increment of the gas crossover

Accumulation impurities in Nafion membrane

Blockage of catalytic sites

Lowering of protonic conductivity

Ion exchange with protons of the sulphonic groups in the ionomers

Figure 2.1: Schematic of the relations between faulty conditions, degradation mechanisms, irreversible degradation, and their effects.

2.1.1 Performance losses and degradation mechanisms associated to inefficient water management

Water management plays a central role in the PEMFC performance. Its optimization has driven most of the research on better component materials and the implementation of new designs in the last years [7]. The presence of water in PEMFCs is essential in order to keep the Nafion membrane and the ionomers in the catalyst layers hydrated. Only in this state, the transport of protons from the anode to the catalytic surface of the cathode is making the oxygen reduction reaction (ORR) possible.

Water is introduced in the system through humidification of the oxidant and fuel streams and it is produced as unique product by the ORR reaction. In many applications, as for example in the automotive field, operating conditions with low relative

humidity of the feeds are preferred, relying on the self humidification of the Nafion membrane. [8, 9]. The produced water tends to condensate in the porous structure of the cathode electrode where part of it is transported to the channel to be expelled. The water present in form of vapour is driven by diffusion and convection to the same direction. Exchange of water between anode and cathode occurs through transport in the Nafion membrane by different mechanisms: (i) electroosmotic drag flux consisting of the water dragged from the protons going from anode to cathode side, (ii) back diffusion of the water generally in the direction from cathode to anode, (iii) hydraulic permeation, (iv) thermal osmotic drag [10]. The last two mentioned mechanisms are significant only under specific circumstances [11, 12]. In particular, the hydraulic permeation flow becomes considerable in asymmetric pressure operating conditions, while the thermal osmotic drag has a strong effect during start up and shut down of the fuel cell because of the higher temperature gradients [13, 14]. Improper balance between the aforementioned mechanisms can lead to the faulty conditions of flooding of the electrodes and dehydration of the Nafion membrane.

A situation of flooding is achieved when liquid water starts to condensate and accumulate inside the porous structure of the electrodes. This phenomenon occurs first in the catalyst layer where the liquid water fills the pores increasing dramatically the resistance of the mass transport of the gaseous reagents, which must dissolve in a thicker liquid film to reach the catalytic sites. In the GDL, the condensed water only occupies the hydrophilic part of the pore network, while it is repelled in the pores made of hydrophobic material which constitute a free path for the gas to reach the catalyst. The water coming out from the GDL forms small droplets on the interface with channel which are subsequently dragged out from the cell by the gas stream. However, water can accumulate under the ribs and the lands of the flow fields in contact with the GDL, where the diffusion length is too long to reach those regions and efficiently remove the liquid water [15, 16]. By the time, the gaseous species cannot diffuse because of excessive presence of liquid water in the pore network. In this way, areas of local starvation of reactants at the catalyst interface are formed. Thereby, strong current inhomogeneities and increase of the concentration polarization have been verified in the cell, causing performance losses and even the shut down of the system in extreme cases [17]. Additionally, the water drops dragged by the streams in the channel can accumulate to the cell outlet at severe flooding conditions, leading to a temporary block of the gas flow path which gives rise to negative spike in the voltage if operating at galvanostatic control. As a result of the gas blockage, the pressure drop increases to a a certain extent after which the excess of the liquid water is flushed out restoring the cell voltage to the initial value. Such a cycle of build up and removal of liquid water causing periodic voltage fluctuations and unstable cell performance has been verified [18, 19].

The main features of the fuel cell components which determine the window of critical operating conditions where flooding takes place are material composition of the GDL and the flow field design. However, the latter has a weaker effect on the water distribution [20, 21]. The cathode side is generally more prone to flooding due to the

continuous production of water through the ORR [22]. However, the anode electrode can also often get flooded under operating conditions where the back diffusion is dominant with respect to the osmotic flow, as for example, at low current density and low and/or asymmetric relative humidity of the streams [23, 24]. Additionally, strong accumulation of water in the anode is a common problem in fuel cells operating in dead end mode [25]. This configuration implies the block up of the anode inlet in order to maximize the fuel consumption avoiding bulky fuel recirculation systems and has been largely applied in the automotive sector [8].

Long term operations or dynamic load changes under flooded conditions lead to degradation of the electrode. Basically, a change of the voltage at the catalyst interface in the starved regions of the cell favours the progression of side reactions which modify irreversibly the morphology and the chemical composition of the catalyst [26, 27].

On the cathode side, the depletion of oxygen in the flooded area of the electrode cause a local voltage decrease leading to lower cathode potentials [28, 29]. Under these conditions, the ORR is replaced by the proton reduction reaction:

$$2H_3O^+ + 2e^- \quad = \quad H_2 + 2H_2O \qquad (E^0 = 0.00V) \tag{2.1}$$

The reversal current generated by this reaction results in inhomogeneities of the current densities which increase in the not starved area of the catalyst in order to keep the total current value demanded by the electrical control applied to the cell. Along with the current densities, temperature gradients arise between different area of the electrode. In the catalyst parts with an increased current, the higher temperature enhances the agglomeration of platinum particles causing a local reduction of electrochemically-active catalyst surface area (ECSA) available for the ORR by the time. The irreversible reduction of the ECSA dramatically increases the polarization losses due to the kinetics.

Water usually accumulates towards the end of the flow fields on the anode side creating a descending gradient of hydrogen partial pressure at the catalyst interface from the outlet to the inlet. Aside from water, nitrogen permeating the membrane from the cathode further dilutes the hydrogen in the depleted regions of the electrode, constituting a so called nitrogen front. Among the other, this phenomenon is quite likely to happen in fuel cells in dead end mode [25, 30]. As soon as hydrogen partial pressure decreases, the corresponding local electrode voltage increases due to an increase of the concentration overpotential. Therefore, a gradient in the voltage drop at the anode electrode/membrane interface is also created. As consequence, the current redistributes with a higher local density in the regions of lower anode concentration overpotential to ensure a homogeneous potential distribution in the electronic conductive material. This redistribution impacts the corresponding cathode electrode regions close to the cell outlet where the local overpotential and ohmic drop decrease. Then, the local voltage is higher favoring the reaction of platinum dissolution and carbon corrosion in this part of the cell.

The platinum dissolution in PEMFCs has been proven to occur either through direct

dissolution of the metal:

$$\text{Pt} \;=\; \text{Pt}^{2+} + 2\text{e}^- \qquad (\text{E}^0 = 1.19 + 0.029\log[\text{Pt}^+]) \qquad (2.2)$$
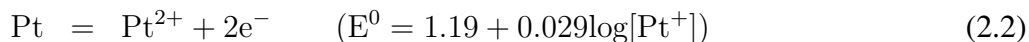
or by production of an oxide layer and subsequent chemical reaction:

$$\text{Pt} + \text{H}_2\text{O} \;=\; \text{PtO} + 2\text{H}^+ + 2\text{e}^- \qquad (\text{E}^0 = 0.98 + 0.59\text{pH}) \qquad (2.3)$$

$$\text{PtO} + 2\text{H}^+ \;=\; \text{Pt}^{2+} + \text{H}_2\text{O} \qquad (\log[\text{Pt}^{2+}] = -7.06 + 2\text{pH}) \qquad (2.4)$$

The Pourbaix diagram of the $\text{Pt}^0/\text{PtO}/\text{Pt}^{2+}$ suggests that Pt metal is fairly stable in the ionomeric phase for a negative pH and an electrochemical potential below 0.9 V at 25 ° C [31]. Outside these conditions, PtO and Pt^{2+} are more stable and the oxidation and corrosion of Pt through the steps 2.2-2.4 are thermodynamically favoured. However, it must be remarked that the reaction 2.4 is extremely slow so that the formation of a platinum oxide layer protects the catalyst against dissolution, which practically takes place only through step 2.2.

The equilibrium concentration measured in the ionomeric phase is very low also at high potentials. For instance, a value below 10^{-9} M has been determined at a potential of 1.2 V. Despite of this, increase of temperature and the Pt migration to other particles can enhance Pt solubility making the dissolution process occurring to a significant extent even at the lower potential of 0.6-0.7 V, as observed in the literature [32, 33].

Smaller Pt particles tend to dissolve preferentially as their chemical potential is higher than that of bigger particles. The Pt ions dissolved in the ionomeric phase migrate to the surface of the larger particles contributing to further increase of their dimensions. By the time, as the size of the small particles falls, their chemical potential further increases accelerating the dissolution rate and determining the progressive growth of the larger particles at the expense of the smaller ones. The final result of this dissolution/redeposition process is an irreversible lowering of the available ECSA. The growth of the particles through this mechanism mechanism is named electrochemical Ostwald ripening due to the analogy with the phenomenon occurring in heterogeneous solutions [34, 35].

Pt dissolution dramatically accelerates under dynamic conditions often resulting in sudden voltage changes. To cycle from high to low current, the voltage of the cell is generally varied from 0.6 to 1 V. While the anode overpotential does not significantly change under voltage cycling due to the fast kinetics of the hydrogen oxidation reaction (HOR), the sluggish kinetics of the ORR makes the overpotential swinging on the cathode. When the voltage rapidly rises from lower to higher values, the platinum can dissolve faster than the formation of a protective oxide layer [36–38]. This phenomenon leads to significant losses of ECSA over repeated voltage cycling. Mayrhofer, et al. [39] applied load cycles between 0.4 and 1.4 V on carbon supported platinum catalyst and registered an increment of the average catalyst particles size from 4.9 to 5.6 nm. Then, they observed that mechanisms of particles aggregation like electrochemical Ostwald ripening, particles migration and coalescence were more accelerated under voltage cycling.

The electronic conductor, as in our case the carbon black, is critical to the dissolu-

tion/redeposition, as this growth process involves a coupled transport of Pt ion in the water ionomer media and the electrons in the conductive support. Virkar and Zhou [40] were the first to verify such an influence observing that the redeposition does not occur using non-conductive Al_2O_3.

Part of the dissolved platinum diffuses into the Nafion membrane and can be reduced to metal Pt by the hydrogen permeating from the anode to the cathode [41–43]. Traces of Pt were already detected in fresh membranes, but their concentration increases upon ageing. By the time, a band of Pt emerges close to the interface between membrane and catalyst on the cathode, which catalyses reactions leading to chemical degradation of the membrane discussed further.

The general carbon corrosion reaction in aqueous solution can be expressed by the following equation:

$$C + H_2O \quad = \quad CO_2 + 4H^+ + 4e^- \qquad (E^0 = 0.207) \tag{2.5}$$
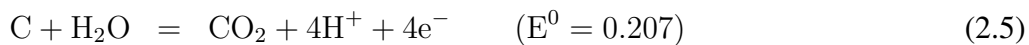
The Nernst potential of 0.207 V is lower than the cathode potential of a running PEMFC implying that carbon oxidation is thermodynamically favoured at standard operating conditions [44]. However, the corrosion rate of carbon is generally very sluggish at potential below 0.9 V at typical PEMFC's operating temperature of 60-90 °C. Anyway, this potential threshold can be shifted depending on the type of carbon, temperature and humidity. For example, the corrosion of widely used Vulcan carbon support is insignificant at cell voltages lower than 0.8 V, but becomes fast going at voltages over 1.1 V and increases with the temperature [45]. Then, serious carbon corrosion has been observed at normal conditions and at open circuit voltage in fuel cells after several thousands of hours of operation using such type of carbon support.

As pointed out previously, local regions at high potential in the cathode arise as result of partial flooding of water in the corresponding opposite parts of the anode. According to Reiser et al. [46], limited exposure to hydrogen in these regions and additional presence of oxygen coming through membrane permeation can cause an anode interface potential drop from 0 to -0.59. This can raise the cathode interface potential to 1.5 V accelerating dramatically the rate of the carbon corrosion of the cathode catalyst layer. In case of extended flooding or no supply of hydrogen, keeping the cell potential at 0.7 V, oxygen evolution and carbon corrosion has been observed on the anode side.

Favourable conditions to carbon corrosion can also be encountered during start-up and shut-down of the cell where the distribution of the fuel is inhomogeneous along the stack at least for a short time. Under a prolonged shut-down, the hydrogen remaining on the anode crossovers to the cathode while all the channels are filled up of air [47]. As consequence, the starting-up of the cell induces a transient condition in which the anode at the inlet is reach of fuel while the region close to the outlet is still mostly occupied by air and starves. During this transient, the local voltage can also reach value at the cathode higher than 1.8 V relative to the hydrogen reference electrode, leading to a fast carbon corrosion. Therefore, cycles of start-up and shut-down can damage considerably the cell. In order to mitigate the effects of this degradation,

systems involving an external load at the start of the cell or different manifold designs which allow a more uniform distribution of the fuel have been proposed. [48]

Carbon corrosion leads to further decrease of the ECSA and thinning of the catalyst layer, as Pt nanoparticles may lose their support and agglomerate to larger particle by electrochemical Ostwald ripening, or may be completely detached and transported out of the cell. Additionally, carbon corrosion can increase the electronic resistance since Pt particles may be disconnected from the electrical network because of the loss of the carbon support. Moreover, the porous structure of the electrode can be also deteriorated causing lowering of its mechanical strength and enhanced mass transport.

Poor humidification of the membrane electrode assembly (MEA) determines a low proton conductivity as this parameter has a proportional dependence on the water content in Nafion. This leads to an increase of the ohmic resistance related to the limited proton transport in the membrane and in the ionomeric phase in the catalyst layer. Moreover, an increase of the kinetic overpotential can also occur under a severe dehydration. Platinum carbon particles surrounded by extremely dried ionomeric phase are not accessible to the protons lowering the effectiveness factor of the catalyst. This results in a decrease of the area available for the reaction and the potential at the catalyst interface increases further.

The nature of the proton transport in Nafion is intimately connected to its chemical structure and physical changes along with the water content. Several studies have been conducted in order to elucidate these mechanisms and have been described in concise reviews [49, 50]. Nafion membranes are constituted by a polytetrafluorethylen (PTFE) backbone having side chains ending in a sulfonic acid group ($-SO_3H$). The sulfonic group upon contact with water dissociates forming a hydronium ion becoming a hydrophilic center where sorbed water acts as counter-ion forming clusters in contraposition to the hydrophobic backbone. Two different activation energies of proton transport, i.e. of 0.36 and 0.1 eV, are respectively measured going from lower to higher water content of the membrane, suggesting two different mechanisms [51]. When low level of water is present in the system, the hydronium ion is localized on the sulfonate heads and there is no a continuous water phase in the membrane. In this state, the transport of protons occurs by the interaction between the close sulfonate chains which exchange the protons through a mechanism which has been hypothesized to be based on the propagation of solitons [52]. The energy of the proton transport required by this mechanism matches the one measured experimentally at low water content. As the quantity of sorbed water increases, the size of the water cluster expands until they coalesce with each others forming a continuous phase with properties which approach the ones of bulk water. Under these circumstances, the protons are transported through Grotthuss mechanism which results in a higher conductivity.

The effect of these phenomena can be also verified by observing the trend of the conductivity along with the relative humidity (RH) [53]. In the range of 13-60 % RH, the conductivity changes sharply by nearly two orders of magnitude, while a change of less than one order of magnitude occurs in the range from 60-100 % RH.

Long exposure of the cell under dehydrated conditions enhances the chemical

degradation of the Nafion membrane. This behaviour is unexpected since the permeability of the membrane to gaseous species decreases at lower humidification. On the other hand, common impurities present in the reactants, as for example sulfate and ferrous ions, are accumulated under these conditions, while they are washed out in drain water at higher RH. These species act as catalyst for the oxidation reaction promoted by the H_2O_2 which is produced as side product during operation in the cell [54].

The mechanism of formation of H_2O_2 and its degrading effect on Nafion have been elucidated by La Conti et al. [55]. According to this work, oxygen molecules permeate through the membrane from the cathode side and are reduced at anode catalyst to form H_2O_2. The chemical reaction occurs by the following scheme:

$$H_2 + 2Pt \rightarrow 2(Pt - H) \tag{2.6}$$
$$Pt - H + O_2 \rightarrow \bullet OOH + Pt \tag{2.7}$$
$$\bullet OOH + Pt - H \rightarrow H_2O_2 \tag{2.8}$$

However, experiments performed by several groups using single side catalyzed MEA show that H_2O_2 is produced by mechanisms involving the cathode catalyst as well [56,57]. The reaction on this side probably takes place at the Pt band in the membrane formed as result of the Pt dissolution occurring at the cathode. The potential drops at the band position from the cathode to the anode value going below 0.2 V, which is a favourable potential for the hydrogen peroxide formation.

The H_2O_2 sorbed in the membrane reacts with metal ions impurities forming hydroxy and hydroperoxy radicals:

$$H_2O_2 + M^{2+} \rightarrow M^{3+} + \bullet OH + OH^- \tag{2.9}$$
$$\bullet OH + H_2O_2 \rightarrow H_2O + \bullet OOH \tag{2.10}$$
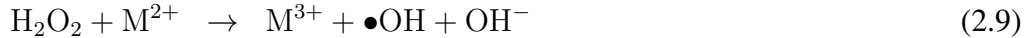
Nafion is susceptible to peroxide and radical attack due to a trace amount of polymer end groups with residual hydrogen containing terminal bonds. The hydroxy and hydroperoxy radicals can attack the end of these groups initiating the decomposition, producing as indicator of this reaction fluoride ions, CO_2, SO, SO_2. As example, carboxylic groups are attacked by hydroxy radicals according to the following scheme:

$$R - CF_2COOH + \bullet OH \rightarrow R_CF_2 \bullet + CO_2 + H_2O \tag{2.11}$$
$$R_CF_2 \bullet + \bullet OH \rightarrow R - CF_2OH \rightarrow R - COF + HF \tag{2.12}$$
$$R - COF + H_2O \rightarrow R - COOH + HF \tag{2.13}$$
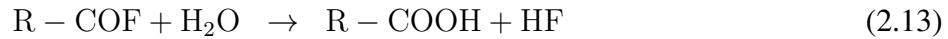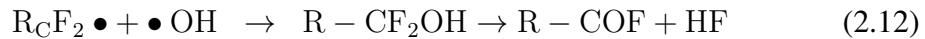
This mechanism of degradation results in membrane thinning and consequent lowering of the mechanical strength. Therefore, phenomena like creeping in tension points of the membrane and pinholes formation accelerate leading to abrupt increase of gas crossover and finally to cell failure.

Transitions from well humidified to dehydrated conditions can also contribute to decrease the life span of a PEMFC. Basically, cycles of operations going from lower to higher current densities can cause transitions to well humidified to dry membrane. In the first case, the ionomers acquiring water swell increasing the thickness of the

11

membrane and subsequently causing non-uniform local stresses [58]. This situation leads to the rise of defects like crack and crazing especially in the area more exposed to compression by the assembly of the cell [59]. On the other hand, drying out leads to residual tensile stresses and chemical degradation mechanisms, as previously described [60, 61]. It has been seen in different study involving acquisition of SEM images over different numbers of RH cycles that an extensive cycling between these two conditions accelerates degradation phenomena like pinholes formation and delamination of the MEA catalyst layer [60].

2.1.2 Performance losses and degradation mechanisms associated to starvation of reactants

In this section, the effect of reactant starvation due to external factors are described. These mainly include malfunction of the oxidant and fuel conditioning system of which stationary and automotive fuel cells are provided. This specific source of starvation must be identified and distinguished from the others already discussed like inefficient water management, improper flow field design or degradation of the electrode materials, since the corrective action to decrease its consequences involves the adjustment of different parameters.

The typical commercialized fuel cell system configurations have been reviewed in several papers and the features of the flow management sub-system are here briefly described [8]. The air supply sub-system generally consists of an air filter at inlet, air compressor, air intercooler, air humidifier, air recycle or bypass, and air exhaust. For low pressure fuel cell systems, a compressor is not present and the air is delivered using fan or blower. Several configurations have been proposed for the fuel supply subsystem: flow through anode (FTA), dead end anode (DEA), hydrogen circulation anode (HCA) and hydrogen ejector anode (HEA). In the FTA mode, hydrogen is supplied by using pressure regulator, while no back valve is used to control the fuel flow at the outlets and the hydrogen is exhausted into air. The DEA mode implies a blocked flow at the outlet where a purging valve is opened regularly to avoid the accumulation of nitrogen and liquid water permeating from cathode to anode. This configuration allows a high fuel efficiency. The HCA is characterized from a hydrogen recirculation system which favours also a high fuel consumption avoiding the gas starvation at the outlet verified in the DEA system. Finally, the particularity of the HEA is the use of an injector to send the fuel to the cell which does not consume electric power compared to the usual hydrogen pump. In this way, the stability of the fuel cell system is improved.

Failures of the reactant supply unit can lead to insufficient oxidant and/or fuel flows, and scarce humidification of the membrane. Natarajan et al. [62] studied the fuel cell performance at voltastatic conditions, and observed that the efficiency of the water management is a strong function of the air velocity. Reducing the reactants flow rates, the water in vapor phase easily saturates and the flooding area shifts near to the gas inlet. This leads to uneven distribution of the current density. Moreover, Wahdame

et al. [63] and Bodner et al. [64] pointed out that the decrease of internal pressure at lower flow rates may cause an increase of the mechanical stresses, uneven internal flow rates and water distribution leading to hot spots inside the cell. Under these conditions, the same degradation mechanisms observed under flooding can occur. As seen in the previous sections, on the cathode side, local water accumulation leads to an increase of Pt dissolution, while in severe starvation conditions shut down of operation due to insufficient oxidant supply can occur. Additionally, the oxidant flow rate influences the dynamic behavior of the cell increasing the voltage undershoot during the load change of power. On the anode side, severe carbon corrosion has been observed under repeated fuel starvation conditions [36,48]. Defects in the humidity supply system can cause dehydration of the membrane accelerating the previously discussed degradation mechanisms.

2.1.3 Performance losses and degradation mechanisms associated to impurities

The different impurities often present in small traces in the air and hydrogen streams affect the fuel cell performance through two mechanisms. Some of them may adsorb on the catalyst surface of the anode and cathode and block catalytic sites for the ORR and HOR reactions, causing kinetic overpotential losses. Other impurities can form cations which can ion exchange with protons bounded to the sulfonic groups in the Nafion membrane. This process lowers the proton conduction and can result in increase of ohmic losses. The losses due to impurities can be permanent and irreversible or temporary and reversible. In last case, a recovery procedure can be performed in order to recover completely the performance.

Impurities in the fuel stream originate from the production process which is basically the reforming of different hydrocarbon mixtures. For example, the most common anode catalyst poison, carbon monoxide, is produced via reverse water gas shift occurring in the steam reforming process. CO chemiadsorbs on the Pt forming a strong bond with the metal. The chemisorbed CO blocks the adsorption of hydrogen reducing the number of the sites available for the HOR [65,66]. This catalyst poisoning causes a reduction of the electro-oxidation rate and a raise of the anode overpotential which dramatically lower the performance compared to CO free case. However, the long exposure to CO poisoning does not affect the durability of the cell and the performance losses can be completely recovered. One of the most common recovery strategy is the so-called air bleed which consists in mixing the fuel stream containing CO with oxygen or air [67]. In this way, CO is chemically oxidized into CO_2 at the catalyst surface without electricity production.

Hydrogen obtained by the reforming of the natural gas may contain traces of H_2S. This compound has a strong affinity with metals like platinum and can adsorb on catalytic sites leading to the same degrading consequences verified in the CO case. The degrading effect of H_2S is a function of the concentration and time of exposure [68]. It

has been seen that 1 ppm of H_2S completely disables a fuel cell operating at 0.5 V after 21 h of exposure. The performance loss is not recoverable indicating the irreversibility of the poisoning process. This is due to the fact that the electrochemical oxidation of the chemisorbed sulfur to non-poisoning species occurs only at 0.8-1.3 V which is not achievable during H_2 fuel cells operations.

Another common impurity present in hydrogen streams obtained by natural gas reforming is ammonia. NH_3 reacts with H^+ on the sulfonic groups of the membrane forming NH_4^+ and consequently lowering the proton conductivity. The poisoning process starts on the anode catalyst layer and continues into the membrane as the ammonia diffuse [69]. The increase of the ohmic resistance due to this poisoning mechanism is rapid. Short-term exposure to NH_3 below 1 h shows reversible effects on the performance. On the contrary, it has been shown that long term exposure leads to irreversible degradation and not complete recovery of the cell previous state.

The cathode side is generally exposed to air pollutants that succeed to pass the filter located before the cell inlet in the PEMFC systems [70]. Among others, one of the most common is the sulfur dioxide produced from fossil fuel combustion which can be found in urban area and in proximity to some chemical plants. SO_2 affects the cathode catalyst through the same mechanism as on the anode side described above. Similarly, the performance cannot be fully recovered by sending contaminant-free air during fuel cell operations, but only by performing cyclic voltammetry to oxidize the adsorbed SO_2.

Nitrogen oxides NO_x are another common air contaminants affecting fuel cell performance. The poisoning mechanism of NO_x has not been fully understood, since no surface species have been detected during cyclic voltammetry indicating no catalyst poisoning mechanism. The poisoning rate does not strongly depend on bulk concentration of NO_x, but rather on the time of exposure. The fuel cell performance gradually decreases achieving a plateau after 30 h. A full recovery is obtained upon supplying air without contaminants for 24 h.

Additionally, salts like NaCl coming from sea mists can contaminate the air cathode supply. The performance loss due to this contaminant is related to the decrease of proton conductivity as a consequence to the exchange of H^+ with Na^+ in the Nafion membrane. Large quantity of salts also decreases the hydrophobicity of the GDL increasing the retention time of water and subsequently the mass transport resistance of the oxygen. Cyclic voltammetry measurements reveal that Cl^- does not block the catalyst surface.

2.2   Use and limits of EIS in the study of PEMFCs

The complexity of the physico-chemical phenomena during PEMFCs operations, the many faulty conditions and degradation mechanisms have boosted the implementation of various diagnostic methodologies which are mostly based on already existing electrochemical techniques. The protocols for characterization of PEMFCs listed in the

international standards test methods includes polarization curves, current interruption methods, cyclic voltammetry and EIS [71].

Polarization curves provide information on fuel cell performance as a whole, failing to give insights on the contributions of specific processes or to determine whether activation, ohmic or mass transport losses are dominant. Current interruption methodologies are widely used to measure PEMFC ohmic resistance with the advantage of having a relatively straightforward data analysis procedure. However, they require a fast monitoring of the voltage changes which can be obtained with the implementation of an additional oscilloscope connected in parallel to the cell, overloading further the hardware [72]. Cyclic voltammetry is successfully used to determine the ECSA of the cell porous electrodes with a good accuracy enabling to get information on the degradation state of the catalyst. Despite of the diagnostic usefulness of these techniques, their application in real time mode to operating multiple cells or stacks under voltastatic control is impractical. On the contrary, several real time diagnostic routines for fuel cells testing based on EIS have been established and integrated with control systems.

EIS is based on the application of a small AC perturbation at different frequencies to the cell which can be performed during operations without significantly influencing the performance of the system. Unlike other techniques, the losses due to phenomena occurring at different time scales can be separately evaluated and visualized in different frequency regions of the EIS spectra. However, this is not always the case since the effects of many processes are often coupled not allowing the identification of them and leading to misleading conclusions [73–76]. The applications and the mode of use of EIS in PEMFC research for improvement of the durability are briefly described in the Section 2.2.1. Then, a survey of the phenomena detected in the different regions of the different representation of the EIS spectra is reported with an emphasis on the coupling of the contributions of different processes and the interpretation of patterns in order to demonstrate the limitations of this technique.

2.2.1 Application and mode of use of EIS in PEMFC research

As the others diagnostic tools, EIS is mainly employed to investigate the influence of different material components and cell designs on fuel cell performance as well as to develop onboard diagnostic tools.

In the first case, EIS is applied on different PEMFCs where certain features of the cell are systematically varied. The outcome of the implemented modifications is evaluated through parameter fitting of a PEMFC model to the EIS spectra. Three different model approaches are usually employed: (i) physically based, (ii) equivalent circuits (EC), (iii) data driven models. An example of this operating mode for testing MEA with different electrolyte compositions is displayed in Figure 2.2.

Following this general strategy, many characteristics of PEMFCs have been improved. For example, a combination of experiments and simulations was used by several groups to investigate the effect of different flow field geometries in order to re-

15
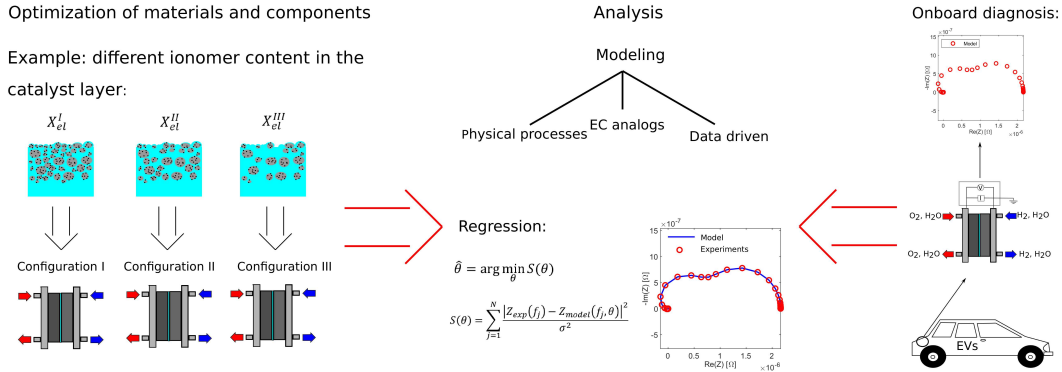
Figure 2.2: Schematic of the main uses of EIS for optimization of cell components and onboard diagnosis.

duce the mass transport resistance on the cathode side [77,78]. Others have focused on the understanding of the relationship between the GDL features and the resistance to oxygen transport [79], water removal [80], electron conduction and heat transport [81] using EIS in combination with other experimental techniques. Moreover, the employment of EIS for a better comprehension of the relationship between catalyst layer structure, its efficiency and durability was extensive and supported the synthesis of MEA with optimized ionomer content, ionomer/carbon ratio and platinum loading [82–84]. Finally, the performance of membranes alternative to Nafion were also tested , as for example poly-vinylidene-fluoride and polybenzimidazole [85, 86].

Generally, the implementation of EIS based onboard monitoring systems for faulty states identification was performed through two different approaches: model based and non-model based. In the first one, a model able to simulate with a certain degree of confidence the monitored output of the system is developed. The models can be differentiated in white-box models constituted of a series of algebraic or differential equations based on physicochemical relations, and black box models based on statistical data driven algorithms that develop empirical relations deduced by a suitable number of experimental database. A scheme of this approach is given in Figure 2.2. Differently, the non-model based approaches allow the detection of faults through qualitative reasoning methodologies based on sets of input and output data. The use of this approach is becoming popular in the last years due to the rising development of machine learning algorithms. However, in this dissertation, we focus on the use of white box model based diagnostic tools, since they give us a physical perspective of the system dynamics.

In the model based approach, the identification of the faulty states can be performed through two different strategies. In the first one, the model can run in parallel with the physical system so that the differences between the model and the system outputs, so called residuals, are measured in real time. Once one or more residuals correlated to a certain faulty conditions overcome a fixed threshold a symptom is detected and communicated to the control system for the implementation of a proper fault isolation

procedure. On the other hand, if the model is provided by parameters related to the behaviour of a specific component or physical phenomena, a correlation between nominal values of parameters obtained in no faulty conditions and faulty conditions can be analysed. Then, the data can be fitted during operation of the system and when the variation of a parameter achieves a certain limit, the correlated fault can be detected and isolated.

The most used white box model approach in PEMFCs diagnostic tools based on impedance is the development of an EC. Elements of a circuit such as resistors, capacitors and Warburg components are used to represent respectively ohmic or charge transfer resistances, double layer capacitance and diffusion. Different combinations of these elements in series or in parallel depending on the relation between the different processes accounted can be obtained constituting the so-called EC model of the cell. Many EC models have been proven useful to obtain parameters such as kinetic resistance and membrane proton conductivity under different operating conditions. Some of them have become a standard methodology of analysis. For example, the transmission line model is particularly suitable to describe spatially distributed porous electrodes giving estimation of double layer capacitance and can be used to optimize structural parameters [87–89].

Several onboard monitoring techniques based on fitting impedance through EC models have been proposed in the last years [87, 90]. One of the first examples that must be mentioned is the one of Fouquet et al. [91] who developed a robust fault detection and isolation diagnostic tool for PEMFC hydration state monitoring. In their work, EIS is performed on the system at a certain frequency range and the spectra are fitted by an EC model. The variation from specific nominal parameters of the model indicates if flooding or drying out of the cell is occurring. Narjis et al. [92] proposed a novel hardware which enables to perform EIS on the operating system superimposing the sinusoidal input signal on the existing output DC/DC considerably decreasing disturbances in the electrical load. The faults are also in this case analysed by the variation of the nominal parameters of an EC model like in the previous case. Other works in this direction have been reviewed in detail [90]. However, the use of the EC models has been highly criticized mainly because of a lack of their physical interpretation which can lead to misleading conclusions [87]. Furthermore, ECs often include too many elements, and parameters cannot be precisely identified through fitting of the spectra. It is also not uncommon that different EC models can fit the experiments with the same accuracy. This dramatically decreases the applicability and the diagnostic power of EC models in many situations.

In the last years, physically based models have been formulated to interpret the meaning of EIS spectra and give a more trustworthy estimation of parameters [93]. These include more complex models involving several physical and electrochemical phenomena able to predict the spectra in a wide range of operating conditions. Other models have been developed with the aim of describing impedance spectra under specific conditions to put a light on unexplained patterns or to estimate some characteristic parameters. Because of their complexity and long computational time required for a

numerical solution, they have been only recently applied as support to onboard diagnostic systems. One of the few example is presented in the work of Chevalier et al. [94] who formulated a 2D model suitable for onboard applications able to discriminate flooding on the anode from the one on the cathode.

Independently from the kind of model approach used, the identification of faults and the extraction of parameters by the impedance spectra is made unreliable from the coupling of physical processes acting in the same time range and from the huge amount of structural and operating parameters influencing them. In the following sections, a review of the processes analysed through impedance spectra and of the diagnostic use is reported dividing them for the frequency region in which they are observed. Namely, the spectra are divided in three sectors: high frequency region (f > 10 Hz), middle frequency region (0.1<f< 10 Hz) and low frequency region (f<0.1 Hz).

2.2.2 High frequency region (f > 10 Hz)

In this part of the spectra, the fastest transient processes involving charge transport are detected. One or two mixed arcs can be observed depending on the operating conditions in the impedance Nyquist plot which converges to the real part axes going to higher frequencies. An example is given in the first row of Table 2.1 which displays the most common patterns observed in Nyquist plots related to PEMFCs.

The value of the high frequency intercept with real axes represents the total ohmic resistance of the cell which can be expressed as the sum of the ohmic resistances of each fuel cell component such as membrane, catalyst layer, GDL, bipolar plates and of the contact resistances between them [99, 100]. The connecting wires can generate an inductive effect influencing the impedance measurements at such frequency range. One approach used to eliminate this effect is to measure the impedance of the opened cell and subtract it from the subsequent measurements [101]. Due to its fast estimation, the determination of the high frequency intercept has been largely used as indicator of particular fault and degradation states, as well as for optimization of operating conditions.

The rapid changes of the high frequency resistance during operation occurring in time scales of tens or hundreds of seconds are assumed to be related to the variation of membrane ionic resistivity due to different membrane hydration state. The contributions of other components are excluded as the variation of their ohmic resistance is result of more sluggish degradation processes. For this reason, the change of the high frequency resistance is exclusively considered a measure of the change of water content in the membrane. The first one to take advantage of this correlation was the R&D division of the General Motors which developed a method to optimize the humidity level of a fuel cell stack based on the continuous monitoring of the high frequency impedance, associating an increased resistance to membrane drying [102]. On the other hand, a decreased resistance in conjunction with low performance was associated to flooding. Following this example, many other methodologies have been developed to differentiate drying and flooding measuring this parameter together with other

EIS Nyquist Plot Patterns	Associated Processes
	High frequency capacitive loop
-Im(Z) [Ω] vs Re(Z) [Ω]; 100 Hz, 10 Hz	• charging of the cathode double layer and ORR charge transfer resistance. • charging of the anode double layer and HOR charge transfer resistance.
	Distortion of the high frequency loop
-Im(Z) [Ω] vs Re(Z) [Ω]; 10 kHz, 10 Hz	• inhomogeneous ionic resistance and capacitance distribution.
	Low frequency capacitive loop
-Im(Z) [Ω] vs Re(Z) [Ω]; 2 Hz, 5 mHz	• mass transport of oxygen along the cathode flow field channel. • dehydration of ionomers of the anode catalyst layer.
	Low frequency inductive loop
-Im(Z) [Ω] vs Re(Z) [Ω]; 1 Hz, 5 mHz	• adsorption steps of the ORR and/or platinum oxidation and dissolution. • CO poisoning on the anode catalyst. • hydration of the Nafion membrane through back diffusion of water.
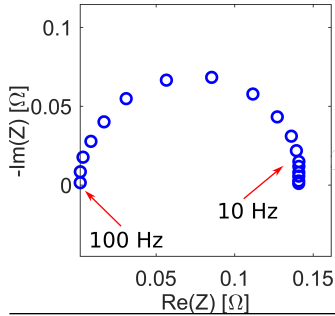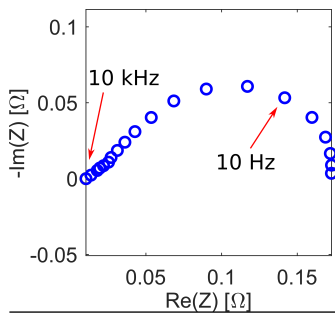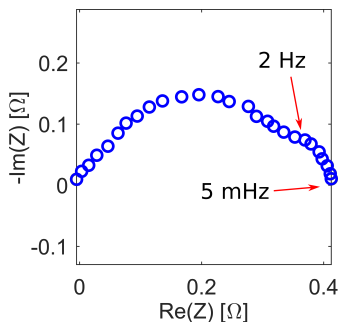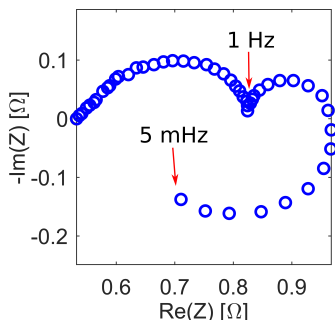
Table 2.1: Most common pattern of EIS Nyquist plot related to PEMFCs. The figures are respectively adapted from Springer et al. [95], Paganin et al. [96], Ciurenau et al. [97], and Wiezell et al. [98].

indicators, as for example back pressure or imaginary part of impedance at specific lower frequency values. In the works of Nitta et al. [103] and Ashgari et al. [104], high frequency EIS has been used to evaluate the contact resistance between the GDL and the catalyst layer as a function of the compression. They claimed that this resistance represents a considerable part of the general ohmic resistance and can dramatically affect the current distribution inside the cell. Moreover, the effect of the poisoning due to traces of NH_3 in the anode feed has also been investigated performing impedance at high frequency [105]. It has been found that the membrane conductivity loss is the main cause of degradation for fuel cells due to ammonia contamination.

Only one arc is generally observed as complete spectrum at low overpotential using well humidified pure hydrogen and oxygen streams [73]. This loop is related to the double layer capacitance of the electrode combined with the charge transfer of the ORR reaction. The diameter of the arc is a measure of the charge transfer resistance and its magnitude decreases going to lower potential, since the kinetic is faster at higher overpotentials. The contribution of the charge transfer of the HOR is neglected under these circumstances, as its kinetic is much faster than ORR. This capacitive arc is mainly used as indicator of catalyst properties such as catalyst surface area, catalyst loading and catalyst utilization.

A distortion of the semicircle at high frequency can be often observed. It is constituted by a straight line at 45 ° with respect to the real axis which resembles the Warburg impedance with a characteristic proportionality $\mid Z \mid \propto \omega^{1/2}$ (see second row of Table 2.1). This feature is generated by the coupling effect of the distributed ionic resistance and the distributed capacitance in the catalyst layer which is emphasized under conditions of limited proton conductivity. Additionally, this distortion can be accompanied by a smaller potential independent loop partially merged to the larger one. One of the experimental proofs of the correlation between the appearing of the 45 ° line path and the distributed electronic properties of the catalyst layer has been given by Paganin et al. [96] who observed a gradual disappearing of this feature by decreasing the thickness of the catalyst layer.

The behaviour of the high frequency capacitive loop and the relation with the structural parameters of the catalyst layer has been extensively studied and interpreted through the development of different model approaches such as simple pore models, agglomerate models, macrohomogeneous models, flooded agglomerate models and EC. Springer et al. [95] were between the firsts to develop a PEMFC model based on the macrohomogeneous description of the porous electrode using it to fit impedance spectra at different voltages and separate the different sources of losses. Specifically, they evaluated the electrochemical kinetics and proton conductivity in the catalyst layer by investigating the effect of these resistance sources on the variation of structural parameters like length of the thin film layer. They were able to reproduce all the features of the EIS spectra including the effect of the charge distribution in the electrodes showing that the highest catalyst utilization is achieved with thin film catalyst layers made of ionomer/Pt/C composites. A limited proton conductivity, together with a low permeation of oxygen in the cathode catalyst layer, are the factors which have the

largest impact on the high frequency arc. Moreover, it was found that the effects of the low humidification in the catalyst layer leading to a scarce proton conductivity in the ionomers can exceed the ones of the resistance of a dried membrane. These results were further confirmed in other works. Ciurenau et al. [97] performed an analysis of the PEMFCs performance through a flooded agglomerate model emphasizing the possibility to evaluate separately the effects due to charge transfer, air diffusion into the pores of the catalyst layer and the diffusion in the Nafion layer surrounding the catalyst particles through the fitting of the high frequency arc of the impedance. Their studies also demonstrated that a good humidification state is essential for a good proton conductivity and an efficient catalyst layer.

Among the EC models, the transmission line representations are the most applied to interpret impedance results, since they can well reproduce the effect of the distributed parameters on the spectra like the 45° straight line in the Nyquist plot. Many studies have taken in advantage of the particular suitability of the transmission line model to extract the electronic conductivity of the different phases constituting the catalyst layer together with the double layer capacitance [106–109]. One of the first works in this direction is the one of Eikerling and Kornishev [106] who developed a transmission line circuit with a repetitive unit which is constituted of two parallel resistive elements respectively for electron transport in the carbon particles and proton transport in the ionomers connected by a double layer capacitance in parallel with a charge transfer resistance. This circuit configuration has been used in many other studies. Additionally, the use of this model approach in combination with impedance experiments performed on cell operating with H_2/N_2 gas feed configuration has become popular to collect information on microstructural parameters of the catalyst. The main advantage of the H_2/N_2 configuration lies in the simplicity of the interpretation of the obtained EIS spectra which are free from the contribution of the ORR kinetics and mass transport. As example, the work of Lefebvre et al. [107] must be mentioned, where this kind of analysis was used to optimize the Nafion loading. Similarly, Cimenti et al. [109] have used the methodology to measure the proton conductivity with good accuracy comparing it with the conductivity estimation using a H_2/O_2 configuration. They claim that the advantages in the first case were the quicker performing of the measurements and the possibility to carry them out in any humidity condition achieving more easily an equilibrium of the ionomer hydration.

Due to its strong dependence on charge transfer resistance and catalyst efficiency, the high frequency capacitive loop is higly sensitive to degradation mechanisms of the catalyst layer i.e. carbon corrosion, platinum dissolution and particle sintering which decrease the active surface area. For this reason, many onboard diagnostic tools have been proposed based on the monitoring of the impedance at high frequency region in the last years. Most of these methodologies imply the development of a model, which is generally an EC, and the fitting of it to a series of impedance spectra of PEMFCs on which accelerated stress tests have been performed. The variation of the extracted parameters along with the degradation state of the cell is interpreted and associated to specific degradation mechanisms, giving the possibility of checking the health status.

Recent examples are the methods developed by Nara et al. [110] and Pivac et al. [111] who correlated the parameter changes of their EC model to morphological changes of the catalysts combining impedance at high frequencies with ex situ techniques as TEM imagines.

The contribution of the anode charge transfer on the impedance spectra is not always negligible. According to Kuhn et al. [112] who have measured the half cell impedance of a PEMFC, anode contribution is even of the same order of magnitude as of the cathode one and has a significant impact on the entire cell impedance below 1 Hz. However, this assumption is considered questionable and object of debate in the electrochemistry community. The impedance response of the HOR has also been investigated in detail by Wiezel et al. [113, 114] using a symmetrical H_2/H_2 setup. Their work combining modeling and experimental studies considers a Tafel Volmer mechanism for the kinetics which gives rise to two high frequency capacitive loops confirming the findings of previous studies [96, 112, 115, 116]. Under conditions of considerable mass transport resistance on the anode, the starvation of hydrogen at the catalyst interface causes an increase of the overpotential and the size of the high frequency arc expands. As consequence, an additional arc appears next to the capacitive cathode charge transfer loop in the Nyquist plot. This pattern has been observed in PEMFCs running with diluted hydrogen gas and/or low flow rate. Boillot et al. [117] investigated in detail this phenomena demonstrating the attribution of the additional arc to the HOR through experiments at different hydrogen stoichiometry.

It has been observed that the contribution of the anode charge transfer resistance becomes significant at low humidity conditions and using thicker membranes. The reason of such a correlation has been first advanced in the study of Andreaus et al. [116]. According to their work, a low humidification implies a decrease of the water content not only in the membrane, but in the electrolitic ionomeric channel of the catalyst layer as well. The anode side is more subjected to the dehydration of the ionomer in the catalyst, as the electrosmotic flow drags water away from anode to cathode. Basically, the channels deep in the active layer become dry and, subsequently, the linked Pt catalyst sites may become inactive, as the proton to be formed by the oxidation of H_2 cannot be hydrated and transported out the catalyst to the membrane. The inactivation of several regions of the ECSA makes the overvoltage increasing to keep the value of the current imposed by the control. The back transport of water produced on the cathode to the anode may compensate this effect, but the use of a thicker membrane tend to minimize this compensation.

On the cathode, the catalyst dries less easily due to the water production by ORR even though Neyerling et al. [118] measured a significant dependence of the catalyst activity on the water content at relative humidity below 60-50%.

2.2.3   Middle frequency region 0.1<f<10 Hz

When EIS is performed on PEMFCs operating in H_2/air feed configuration an additional capacitive loop like the one showed in the third row of Table 2.1 appears in

the Nyquist plot region corresponding to this frequency range. This pattern is not observed using saturated streams of pure oxygen as feed. The size of this additional arc increases along with the overpotential and often overlaps completely with the charge transfer contributions at higher frequency. Its origin has been initially attributed only to mass tranport resistance of the gas in the cathode GDL and catalyst layer. Through a combination of modeling and experiments, Springer et al. [95] concluded that the appearing of the second low frequency arc indicates significant losses due to diffusion of oxygen diluted with nitrogen in the GDL. The main experimental evidence of this hypothesis arose from the fact that the use of a double GDL layer leads to a lowering of the fuel cell performance accompanied by an increase of the low frequency loop. The later work of Ciurenau et al. [97] supported the view of Springer further clarifying the role of the electrode flooding. They investigated the effect of the flow rate observing a gradual decrease of the low frequency arc using higher flow rates. Supported by the fitting of experiments to an EC model, they came to the conclusion that this phenomenon reflects the appearance of a concentration gradient of oxygen in the GDL and catalyst layer resulting from a decrease of the effective porosity due to accumulation of water. Liquid water starts to increase when the rate at which it accumulates in the cathode becomes larger than that at which it is removed. Thus, the disappearing of the low frequency capacitive loop using higher flow rates is explained by an acceleration of the removal of water by evaporation or dragging out by the gas stream. Any other factor accelerating the water removal from the cathode leads to the same trend on the impedance spectra, as for example the decrease of the thickness of the Nafion membrane verified in the work of Paganin et al. [96] which makes more efficient the back diffusion of water into the membrane. The studies of Fouquet et al. [91] and Canut et al. [119] on impedance of fuel cell stacks further confirm the hypothesis registering an increment of the low frequency part of impedance in the range f< 10 Hz under flooding conditions. A considerable variation of the magnitude and phase Bode plots along with the level of flooding was also observed, which respectively shows a significant increase and decrease of their values in this frequency region. They constitute sensitive indicators of this type of losses that have been extensively used for diagnostic purposes.

However, the mass transport resistance of the oxygen inside the GDL only constitutes a single factor influencing the impedance at low frequencies. Several studies have demonstrated that the actual phenomenon causing the low frequency capacitive loop is related to the depletion of the reactants along the channel generating concentration gradients of oxygen and water from the inlet to the outlet of the cell flow fields. The group of Schneider was the first to describe the effect of the oxygen concentration variations along the channel during impedance measurements [120–122]. In their experiments, they used a single channel segmented fuel cell setup of technical size (200 cm^2) enabling to measure impedance in different sectors along the channel direction. The periodic variation of the oxygen partial pressure of the outlet stream was measured by monitoring the voltage variations of an additional cell kept at galvanostatic control and located at the cathode outlet. It was observed that oxygen concentration oscilla-

tions build up along the cathode gas channel during EIS experiments in the frequency between 0.1 and 10 Hz, causing an additional polarization sinusoidal voltage contribution which couples to the modulated voltage imposed at the electrode by the electric control. The local interactions between these two periodic voltage variations evoke the formation of positive and negative resistance loops along the channel. The integration of all the local resistance loops generates a global positive resistance loop which results in the appearing of the capacitive arc in the impedance. The local responses to the oxygen concentration change and are influenced by the operating conditions, the hydration state of the ionomeric components and the thickness of the GDL. Therefore, it can be concluded that the resistance to the gas transport in the GDL influences only quantitatively the impedance response determining the size of the middle frequency arc. When using a high flow rate, no significant oxygen depletion occurs along the down stream due to the low residence time. For this reason, concentration oscillations don't occur and, consequently, the capacitive loop would appear in the spectra. The same happens if pure oxygen is used instead of air, since there is no diluting nitrogen in the cathode reactant gas.

Due to its origin, the capacitive loop at low frequency is often called channel impedance. The channel impedance has been studied by different groups that observed it also in serpentine flow fields [123]. Among the theoretical works, worth nothing are the series of papers of Kulikovsky [124, 125] who developed a 1D model of a segmented PEMFC capable to described the trend of the local impedance as function of the stoichiometry and oxygen diffusivity in the GDL. Thus, the amplitude of the spatial oscillations of the local impedance decrease towards the outlet with a slope which mainly depends on the diffusivity of oxygen. An analytical expression was derived which allows to easily determine this parameter from fitting of different local impedance spectra. However, the model is valid only assuming a constant cathode overpotential along the channel.

Many other models have been developed in order to fit the low frequency impedance and evaluate transport parameters to diagnose flooding states. Most of them are EC which do not account the channel impedance and consider only the transport in the porous electrode of the cathode [126, 127]. For this reason, they often lead to erroneous estimation of parameters and misleading conclusions giving only an indicative trend. One example of EC description is the one of Chanderis et al. [128] who developed a simple model relating the low frequency resistance to the air inlet stoichiometry in order to investigate the reason for the difference between the value of the resistance at the low frequency impedance and the one measured by the slope of the polarization curve. They claim that the difference becomes prominent when operating at high current densities. Therefore, they concluded that they are due to the increase of the oxygen depletion along the cell.

Channel impedance has been described in higher detail through physical based mode. Similarly to Kulikovsky, Maranzana et al. [123] used a pseudo-2D model to investigate the relationship between the air velocity, cell geometry and the channel impedance. By fitting their model to the low frequency arc, the air velocity could be

estimated leading to a better evaluation of other parameters related to diffusion losses especially at higher current densities. However, their model could only be solved numerically limiting its use as diagnostic tool. Chevalier et al. [129] derived an elegant analytical expression by which the air velocity could be extracted through the fitting of the plot depicting the ratio between imaginary and real part of the impedance. Keller et al. [130] determined the residence time of the gas transport in the cathode flow field of a 90 cell stack system from the channel impedance with the aid of data fitting of an ad-hoc EC. They found out a proportional nonlinear dependence between the time constant and the air flow velocity. More surprisingly, it was verified that the relation was invariant from cell size and geometry of the flow field. The humidity of the inlet flow was not influencing the residence time of the gas in the stack, but it changed quantitatively the impedance spectra.

A capacitive loop has been also observed using pure oxygen as cathode feed under low humidity conditions. This pattern cannot be attributed to the mass transport limitation on the cathode. Instead, it has been related with large acceptance to the relationship between the activity of the HOR and the hydration state of the ionomers. As described in the previous section, Andreaus et al. [116] and Wiezel et al. [113, 114] pointed out that level of water in the ionomers has a significant influence on the HOR kinetics, since it determines the proton conductivity of the formed hydrogen ions. The transport of the ions can become a limiting step at low humidity significantly increasing the HOR charge transfer resistance. In this context, when a sinusoidal current perturbation is applied to the cell, the variation of the flux of water from anode to cathode due to the electrosmotic drag force leads to an increase of the drying out of the ionomers in the anode catalyst layer. Then, the consequent increase of charge transfer resistance determines the appearing of a capacitive loop in the Nyquist plot. A shifting of the top frequency of the arc to lower ones has been registered with increasing membrane thickness L following a proportional relation to $1/L^2$. This trend confirms the relation of the phenomenon behind the arc with the water transport. A further reinforcement to this hypothesis comes from Schneider et al. [131] who have measured the high frequency impedance in parallel to a current step observing a maximum of the resistance around the time scale of one second after the perturbation. The maximum resulted to increase along with a decrease of humidification level. A further theoretical and experimental work of Wiezel et al. [98, 132] shows that the use of air feed causes the complete covering of the capacitive arc in the Nyquist plot due to the dehydration, making impossible the diagnosis of the drying out of the anode under these conditions.

2.2.4   Low frequency inductive loop f< 0.1Hz

An inductive loop crossing the positive side of the real axis, as the one depicted in the fourth row of Table 2.1, has been observed in the Nyquist plot of PEMFCs under different operating conditions at frequency below 0.1 Hz. This pattern causes discrepancies between the slope of the polarization curve and the resistance measured by impedance at the lowest frequency which is often not measured below 0.1 Hz. The explanation of

this inductive behaviour is still under debate in the scientific community, since many processes could cause it. Pivac and Babir [133] have recently reviewed all of them proposed in several modeling and experimental studies.

Many authors have suggested that the inductive loop could be attributed to the effect of the characteristic heterogeneous side reactions occurring in the cell which include several potential-dependent adsorbed intermediate species. Some of them are responsible of the degradation of the membrane and electrodes. The first authors to measure the inductive behaviour at low frequencies and advance the kinetic hypothesis have been Antoine et al. [134]. Considering the mechanism proposed by Damjanovic et al. [135], they related the inductive loop to the relaxation of adsorbed intermediate species of the ORR. This mechanism contemplates an initial fast adsorption of O_2 on Pt considered in pseudo-equilibrium conditions, and involving a low partial coverage followed by an electrochemical step. The latter consists of the protonation of the O_2 which gives rise to other adsorbed species, i.e. O_{ads}, OH_{ads} and O_2H_{ads}. According to Antoine et al. [134], the slow relaxation of these products leads to an increase of the catalyst area available together with a subsequent decrease of the over-potential which generates the inductive loop. The findings were supported through simulations of a flooded homogeneous model of a gas diffusion electrode. However, the experiments were performed in a gas diffusion electrode setup with a very thin porous layer implying a negligible diffusion limitation. Therefore, it is not clear if such kinetic contribution would give a visible impact in the impedance spectra of an operating PEMFC where various transport processes occurring at the same time scale could cover this kinetic effect. Makharia et al. [108] measured the inductive loop at low frequency in a fuel cell with 50 cm^2 active area, but they did not give an explanation of it and just referred to the work of Antoine et al. [134], as their focus was on evaluating the ohmic resistance of the catalyst layer. Franco and Tembley [136] developed a mechanistic model of a PEMFC cathode based on an irreversible thermodynamic description accounting a Damjanovic mechanism for the ORR, Pt oxidation and dissolution (Equations 2.2-2.4 in Section 2.1.1). The obtained simulations showed a qualitative agreement with their experiments which exhibited a low frequency loop decreasing in size along the nominal current. This pattern was explained through the competition between the intermediates on the catalytic surface, but was not illustrated in detail. Kuhn et al. [112] performed impedance experiments on a PEMFC cathode using a three electrode half cell setup which allowed to separate cathode and anode contributions. Surprisingly, they found out that the characteristic frequency of the inductive loop did not change in their measurements along with steady state current suggesting that a potential independent process could explain such a behaviour. They suggested as possible cause a chemical step occurring on the cathode surface. Thus, they proposed a kinetic mechanism for the ORR involving O^- and peroxide OH as adsorbed intermediates on Pt. In this picture, the inductive loop is due to the formation of OH_{ads} from the adsorbed O^- which is independent from the potential. Roy et al. [137] considered three different reaction schemes occurring on the cathode side. In the first one, a one step mechanism for the ORR was used. The second scenario

involved a two step ORR with formation of H_2O_2 as intermediate according to a two electron path which is found to be favoured with respect to the classic four electron path on Pt nanoparticles supported on carbon [138]. In the last reaction scheme, a one step ORR occurring in parallel to Pt oxidation and dissolution was contemplated. The kinetic models were inserted in a general PEMFC model used to fit impedance spectra. Only the two mechanisms involving more steps with reaction intermediates could reproduce the inductive loop. Interestingly, it was observed that the inductive loop in the Pt oxidation case was caused by the adsorption/dissolution steps of the platinum oxide which was indirectly controlling the rate of the ORR. Therefore, it was concluded that a one step reaction could not generate the inductive loop. On the other hand, the two step mechanisms could also not be discriminated by EIS. A somewhat similar study was conducted by Cruz-Manzo et al. [139] who also confronted the impedance spectra considering one reaction scheme with Pt oxide formation, and another involving ORR double step mechanism with H_2O_2 intermediate. They concluded that the inductive loop in the EIS measurements can only be accurately reproduced by a model accounting for platinum oxide and hydrogen peroxide formation together, and not from one including for either PtO or H_2O_2. This explanation is contrasting with the previous one.

Wagner and Schultz detected a strong pseudo inductive behaviour below 3 Hz under condition of CO poisoning of the anode catalyst [140]. This path was attributed to a surface relaxation process due to the competitive oxidation of hydrogen and carbon monoxide. The progressive increase of the size of the pseudo inductive loop along the time makes the CO poisoning recognizable from the other process causing inductive patterns.

Another explanation which has been given for the inductive loop is related to the slow dynamics of uptake of water in the ionomers of the Nafion membrane. Basically, the AC current applied during the EIS measurements perturbs the hydration state of the membrane at lower frequencies, as it changes the water production rate at the cathode and the electrosmotic water drag flux. Especially at low humidity conditions, the variation of the electrosmotic drag of water initially leads to the dehydration of the ionomer on the anode side, causing a decrease of the proton conductivity and, thus, the middle frequency capacitive loop discussed previously. At lower frequencies, the water generated on the cathode is transported to the anode driven by gradient forces newly increasing the water content of the membrane. Consequently, a decrease of the resistance of the cell is obtained as final result which is translated by an inductive loop in the Nyquist plot.

Wiezel et al. [113, 114] theorized such interaction of mechanisms through the development of a dynamic 1D model of a PEMFC. They predicted that the frequency range where the inductive loop appears is dependent on the water diffusivity in Nafion and thickness of the membrane. Additionally, they claimed that the loop should be more pronounced at sub-saturated conditions and using thicker membranes. They attempted to validated their findings using a symmetrical cell with H_2/H_2 feed configuration equipped with a 4 electrodes system enabling to measure separately the

impedance of the anode and cathode side. However, the inductive loop was not observed in the measured impedance spectra because of the impossibility to achieve low frequency bands. In a series of works of the same group years later, the same model approach was used to study the dynamics of PEMFCs with O_2/H_2 feed configuration under low humidity conditions [98, 132]. A systematic series of experiments using different combinations of humidity level of the feeds and membrane thicknesses were used to validate the model. Differently from the previous study, the inductive loop was caught in the impedance spectra and all the predicted trends were observed. Moreover, the frequency range of the inductive loop was found to be proportional to $1/L^2$. Schneider et al. [131] further confirmed the membrane transport contribution integrating impedance measurements of a cell operating under sub-saturated conditions with current step experiments where the resistance was registered continuously in parallel. After the maximum of the resistance due to the membrane drying out already mentioned in the previous section, a subsequent decrease has been registered confirming the relation between the inductive loop and the variation of the ohmic resistance due to the hydration of the membrane. However, this trend has been observed only under sub-saturated conditions suggesting that eventual inductive loop measured in well humidified conditions cannot be attributed to membrane hydration. A more complete model was formulated by Setzler and Fuller [141] which included together platinum oxide formation, water transport in the membrane, heat generation and cell hardware effects. Moreover, they considered a one step ORR dependent on the free catalytic sites as electrochemical kinetic expression on the cathode. They claimed that both water build up and platinum oxide growth could generate inductive loops, but the latter made more significant contribution to it under the experimental conditions tested in their work. According to them, at high steady state current density, the variation of the current generates an increase of temperature that offsets the effect of the water generation. In this case, the hydration response can be limited or even reversed giving rise to a positive increment of resistance. Under these circumstances, the inductive loop is dependent on the relaxation due to kinetics of platinum oxide formation. More recently, Bao et al. [142] through simulations of a 2D model including a detailed membrane transport description further demonstrated that the inductive behaviour can be due to the slow transport of water in Nafion. However, they stated that membrane water system could achieve an equilibrium by days in reality, so that an inductive arc may not appear or be distinguished in experiments. Nevertheless, their theory was not supported by experiments.

2.3   Conclusions

PEMFCs are exposed to several degradation mechanisms which are dramatically accelerated under different operating modes and faulty conditions. In order to mitigate their effects on the lifetime of the cell, diagnostic tools integrated with control systems are required to identify such harmful conditions and minimize the permanency under

these operating states. Additionally, the knowledge of the transient processes occurring in PEMFCs is essential for the development of new materials and cell design improving further the durability.

Among the numerous methods available for the analysis of electrochemical systems, EIS is the only one which enables to separate the contributions of a large number of physico-chemical processes occurring is series and/or in parallel. However, the dynamics of PEMFCs system is complex and the effect of many phenomena overlap with each other in the EIS spectra under most of the operating conditions, since they present comparable time constants. For example, charge transfer of the HOR and ORR reaction and mass transport resistance can mask each other generating only one arc in the Nyquist plot making difficult the determination of their single impact on the performance. Moreover, the interpretation of some patterns is still not well understood due to the complex interaction between many processes, making the use of spectra in the respective frequency regions not suitable for diagnostic purposes. An example is the low frequency inductive loop which could be caused from the dynamics of side reactions occurring on the catalyst surface, water transport in the Nafion and heat generation.

For this reason, the development of experimental tools to identify and separately measures the impact of selected processes would be beneficial for improving the diagnostic and understanding of PEMFCs.

Chapter 3

Concentration-alternating frequency response analysis: motivation and concept

The attribution of the patterns observed in the impedance spectra of PEMFCs is not unambiguous in most of the cases, and a clear picture on the dynamics is not possible. As seen in the previous Chapter 2, the main reason of this issue lies in the overlapping of the contributions of different processes with similar time constants. For this reason, diagnostic tools mostly based on the fitting of EIS spectra through EC or physical based models often lead to erroneous evaluations of the different performance losses of the fuel cell.

In order to overcome the limitations of the EIS, many alternative experimental techniques based on dynamic nonelectrical input and/or output have been proposed for the study of PEMFCs in the last years. The idea behind this approach is that the stimulation and detection of a different physical variable respectively could influence and contain information about specific dynamics, making possible the decoupling of their contributions from the others.

In this chapter, a general mathematical framework based on LST is presented in order to asses a theoretical quantification of the information contained in a transfer function related to a certain input/output configuration and verify the possibility to study specific dynamic phenomena (Sections 3.1.1 and 3.1.2). Further, a brief review of the methodologies based on nonelectrical input/output applied to different electrochemical systems with a particular focus on fuel cells is presented emphasizing advantages and critical aspects respect to classic EIS (Sections 3.1.3 and 3.1.4). Finally, the concept of CFRA is introduced as new diagnostic tool for PEMFCs systems (Section 3.2).

3.1 Theoretical background

EIS and the alternative dynamic experimental techniques discussed in this chapter belong to the class of the linear FRA. These methodologies involve the application of periodic perturbations of an input variable at different frequencies to a system and the analysis of a response variable by the means of the Fourier Transform. The amplitude of the input must be small enough to assure a linear response.

The theoretical background of the FRA techniques involving nonelectrical quantities to study the dynamics of electrochemical systems has been extensively investigated in the past. For example, a general mathematical framework to formulate and analyse different nonelectrical transfer functions has been proposed by Gabrielli and Tribollet [143]. A methodology to assess the reliability of the data collected through non-electrical frequency response experiments has been developed by Macdonald [144]. Recently, Collet-Lacoste [145] has performed an analysis of the relationship between a generic perturbation and a certain response in electrochemical systems based on the non-equilibrium thermodynamic theory. However, a procedure to quantify the influence of a dynamic variable on the frequency response spectra in relation to the input and output considered has not been presented yet.

As our purpose is the decoupling of the contributions of certain processes from the others, a mathematical framework to quantify the information contained in a certain transfer function regarding specific dynamics in relation to the input/output used is presented. Furthermore, the sensitivities of different transfer functions to a certain characteristic parameter of the system is also discussed. It must be remarked that the following framework is applicable to any model describing an electrochemical system.

3.1.1 Canonical form of the state space representation and residual matrix

Any set of equations describing the dynamic behaviour of a lumped or distributed time invariant system (Figure 3.1) can be reduced or approximated to the following mathematical form [146, 147]:

$$\dot{X} = F\left(X, W\right) \tag{3.1}$$
$$Y = G\left(X, W\right) \tag{3.2}$$

The elements x_i of the vector X represent the state variables which the values determine the state of the system. On the other hand, the components w_j of the vector W are the input quantities or constraints which impose the experimental conditions. Furthermore, the input quantities y_k of Y mean the output variables which allow the state of the system to be observed. Generally, the set functions F_i and G_k are nonlinear. In case of distributed system, the related partial differential equation are reduced to a set of ordinary differential equations through numerical discretization methodologies.
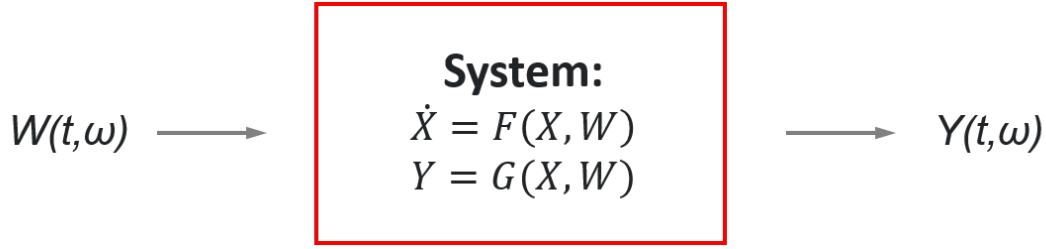
Figure 3.1: General scheme of FRA of time invariant dynamic system.

In the context of electrochemical systems, the elements of such vectors could assume the following meaning: (i) the components x_i could be, as example, the concentrations of the reactants and of the charged species in the electrolyte, coverage fractions of intermediate species on the electrode surface or the local overpotential; (ii) w_j can be the overall voltage or current, temperature and partial or total pressure; (iii) as y_k the voltage and current can be measured, as well as the reflective power of a photosensitive electrode surfaces, the mass added or removed from adsorption/desorption reactions and the reactant concentrations coming out from the system. The nonlinearities of the functions F_i and G_k are mostly attributable to the kinetics of the electrochemical reactions whose rate has an exponential dependence on the potential.

Considering the solution of the system at a fixed steady state, the dynamic response to a certain input perturbation can be calculated through linearization of the equation system with respect to the steady state and input variables, obtaining the following simplified version:

$$\dot{X} = AX + BW \tag{3.3}$$
$$Y = CX + DW \tag{3.4}$$

where A, B, C and D respectively represent the so called state space, controllability, observability and transmission matrixes whose components are equal to:

$$A_{i,j} = \left.\frac{\partial F_i}{\partial x_j}\right|_{x_n, w_m, n \neq j} \tag{3.5}$$

$$B_{i,j} = \left.\frac{\partial F_i}{\partial w_j}\right|_{x_n, w_m, m \neq j} \tag{3.6}$$

$$C_{k,j} = \left.\frac{\partial G_k}{\partial x_j}\right|_{x_n, w_m, n \neq j} \tag{3.7}$$

$$D_{k,j} = \left.\frac{\partial G_i}{\partial w_j}\right|_{x_n, w_j, m \neq j} \tag{3.8}$$

Then, it is remarkable that the values of the elements of the matrix A depend on the intrinsic dynamic features of the system, while, in the case of B and C, they are respectively functions of the kind input and output considered.

32

Generally, the system response to a perturbation is described through the corresponding transfer function $H(i\omega)$ in frequency domain, obtained by applying the Fourier transform properties to the system of equations 3.3-3.4. It reads

$$H(i\omega) = \frac{\tilde{Y}(i\omega)}{\tilde{W}(i\omega)} = C(i\omega I_n - A)^{-1}B + D. \tag{3.9}$$

For $\Lambda = diag(\lambda_i)$ $(i = 1, 2...n)$ be the diagonal matrix of the eigenvalues λ_i of A, P the matrix of the corresponding left eigenvectors p_i, and $Q^T = P^{-1}$ the matrix of the corresponding right eigenvector q_i^T, the equivalent canonical form of the system 3.3-3.4 reads [146, 148]:

$$\dot{X}_d = \Lambda X_d + Q^T BW = X_d + \beta W \tag{3.10}$$
$$Y = CPX_d + DW = \gamma X_d + DW. \tag{3.11}$$

where $\beta = Q^T B$ constitutes the normal form of the input matrix, while $\gamma = CP$ the normal output matrix. According to this new representation, the transfer function expressed in the equation 3.9 for a single input single output (SISO) system can also be written in the following simplified form:

$$H(i\omega) = CP(i\omega I_n - \Lambda)^{-1}Q^T B + D = \sum_{k=1}^{n}\frac{r_k}{i\omega - \lambda_k} + d_1 \tag{3.12}$$

where

$$r_k = Cp_k q_k^T B = \sum_{i=1}^{n}\sum_{j=1}^{n}c_{1,i}p_{i,k}q_{k,j}^T b_{j,1} = \gamma_{1,k}\beta_{k,1} \tag{3.13}$$

The quantities r_k represent the elements of the residual vector, each one relative to a certain dynamic state variable k characterized by a time constant $\tau_k = -\frac{1}{\lambda_k}$. As displayed in the Equation 3.13, they are dependent on the product of the k elements of the normal form of the input and output vectors which determine the contribution of the corresponding state variable k to the transfer function in a certain input/output configuration. If the value of one of the elements of γ is zero or negligible compared to the other ones, it means that the dynamics corresponding to the k variable is not observable or has not a significant contribution to the transfer function based on the considered output. In the same way, if one of the elements of β is negligible relatively to the others or zero, the corresponding k variable is not controllable and has no influence on the transfer function determined using the related input. Therefore, given a model describing a certain system, the determination of the residual matrix is a valuable theoretical tool to estimate which kind of dynamics influence the most the related FRA spectra using a certain input/output configuration. Additionally, it can be used for model reduction purposes, suggesting which variable and/or phenomenon can be neglected to describe the dynamic effects of a certain perturbation.

3.1.2 Parameter sensitivity of a general transfer function

A certain degree of controllability and observability of a variable in the transfer function is not the only condition to be fulfilled for identification of a process. A sufficient sensitivity of the transfer function to the changes of parameters influencing the studied phenomena must also be verified. In general, a high sensitivity implies a smaller variance in the measure of a certain parameter resulting in a more accurate estimation [149, 150]. Given the vector of the n_p parameters $\boldsymbol{\theta} = \left(\boldsymbol{\theta_1}, ... \boldsymbol{\theta_{n_p}}\right)$ which characterizes a system, the sensitivity of the transfer function as function of the frequency with respect to a certain parameter θ_m is computed by the following equation:

$$\frac{\partial H\left(i\omega\right)}{\partial \theta_m} = \sum_{k=1}^{n} \left(\frac{\frac{\partial r_k}{\partial \theta_m}\left(i\omega - \lambda_k\right) + r_k \frac{\partial \lambda_k}{\partial \theta_m}}{\left(i\omega - \lambda_k\right)^2} \right) \tag{3.14}$$

In the Equation 3.14, the values of the residual vectors and their derivatives with respect to the fixed parameter determine the part of the sensitivity related to the input/output configuration used. This can be better observed by expressing the derivative of the residual vectors with respect to a generic parameter θ_m:

$$\frac{\partial r_k}{\partial \theta_m} = \sum_{i=1}^{n} \sum_{j=1}^{n} \left(c_{1,i} b_{j,1} \frac{\partial p_{i,k} q_{k,j}^T}{\partial \theta_m} + p_{i,k} q_{k,j}^T \frac{\partial c_{1,i} b_{j,1}}{\partial \theta_m} \right) \tag{3.15}$$

It is noticeable from the Equation 3.15 that the sensitivity of the residuals not only depends on the value of the elements of the controllability and observability matrix, but also on the sensitivity of the elements of these vectors to the parameter θ_m. Then, the Equation 3.15 can be used to determine which types of input/output configuration and which frequency band are the most suitable for the identification of a set of parameters related to a specific dynamic process.

3.1.3 General overview of FRA methodologies applied to electrochemical systems

Several FRA techniques alternative to EIS based on nonelectrical input and output have been developed to study the dynamics of various electrochemical systems. Among the ones involving an electrical input and a nonelectrical output, AC electrogravimetry is certainly the most applied. It consists of the coupling of EIS with a fast response quartz crystal micro-balance in order to monitor the mass variation of the electrode. A sinusoidal perturbation of voltage is applied to the system, so that the admittance is measured together with the electrogravimetry transfer function constituted by the ratio between the complex variation of the mass of the electrode and the amplitude of the voltage. This way, the effects of the processes involving the change of the mass of the electrode such as adsorption-desorption of reaction intermediates and transport of cations or anions in films can be decoupled from the impedance. Because of these

features, AC electrogravimetry has been largely applied in corrosion sciences to study, for example, mass transport in oxide materials as WO_3 [151], iron behavior in acidic medium [152], conductive polymers like poly (neutral red) films [153], and inorganic conductive films like Prussian Blue films [154].

Mostly, FRA techniques involving the use of a nonelectrical input and detection of an electrical output have been proposed. The most successful belonging to this type of FRA are the electro-hydrodynamic (EHD) impedance, thermo-electrochemical impedance (TI) and photo-electrochemical impedance (PI).

EHD involves the sinusoidal modulation of the rotation rate of a rotating disk electrode and the measure of the resulting sinusoidal current or voltage depending on the electric control applied on the system. Then, two transfer functions can be determined which are the ratio between the complex current or voltage and the amplitude of the disk rotation rate. EHD impedance enables to isolate the effect of mass transport resistance from the classic EIS spectra. For this reason, the technique is particularly suitable to study processes that are under mass transport control allowing the estimation of diffusion coefficients of ionic species from the determination of the Schmidt number. It has been widely used to evaluate the efficiency of corrosion protections [155, 156] and the effect of calcareous deposit on metal structures in water [157].

TI is based on the modulation of temperature and the collection of the current or voltage response. The temperature perturbation is obtained by using a special setup which applies a light beam coming from a IR diode on the electrode surface. The analysis of the TI transfer function allows to determine the activation energy of the electrochemical and adsorption reaction steps, and evaluate the effect of the thermal convective and diffusive transport. It has been revealed to be useful in the determination of kinetic mechanism of electro-crystallization of nickel [158] and electro-deposition of silver in nitrate and tartaric solutions [159, 160].

PI includes different transfer function all based on the stimulation of surface of photo-sensible materials by modulation of the intensity of light beams and the detection of the photoelectric response. The current and voltage responses have been considered for the system analysis, as well as the ratio of these two outputs in complex form. These transfer functions measure the resistances generated by the transport of charged species involved in the photo-electrochemical processes. This technique has been applied for characterizing solid state silicon [161], organic and perovskite solar cells [162, 163].

3.1.4 FRA applied to fuel cells

In the last decade, several FRA methodologies alternative to EIS based on nonelectrical quantities have been proposed for the study of PEMFC dynamics. As already mentioned in the Chapter 2, the renewed interest for such experimental techniques is due to increased demand of more accurate and selective diagnostic tools. In Table 3.1, the nonelectrical FRA techniques developed in the last years are listed together with the expressions of the related transfer functions and the specific processes detected in

FRA Technique	Transfer Function	Processes Isolated
EPIS	$Z_{E/P} = \frac{\tilde{E}(i\omega)}{\tilde{P}_{out}(i\omega)}$ $Z_{I/P} = \frac{\tilde{I}(i\omega)}{\tilde{P}_{out}(i\omega)}$ $Z_{P/E} = \frac{\tilde{P}_{out}(i\omega)}{\tilde{E}(i\omega)}$ $Z_{P/I} = \frac{\tilde{P}_{out}(i\omega)}{\tilde{I}(i\omega)}$	Mass transport gaseous reactants and liquid water in the channel, GDL and catalyst layer.
ETIS	$Z_{ETIS} = \frac{\tilde{T}(i\omega)}{\tilde{I}(i\omega)}$	Heat transport along the flow fields.-Water generation.
LIT	$Z_{LIT} = \frac{\tilde{T}_{surface}(i\omega)}{\tilde{T}_{in}(i\omega)}$	Water accumulation along the flow fields and GDL.
HECII	$Z_{HECII} = \frac{\tilde{t}_{H_2O}(i\omega)}{\tilde{I}(i\omega)}$	Water generation.

Table 3.1: A summary of FRA transfer functions based on nonelectrical input or output together with the main processes isolated by them.

their spectra. Each methodology is discusses more in detail below.

The first work towards this direction has been the one of Niroumand et al. [164] who observed the arise of cathode back pressure oscillations using low flow rates which induced voltage sinusoidal waves. They related this phenomenon to the dynamics related to the accumulation of water in the cathode catalyst layer and GDL which simultaneously cause the increment of the back pressure and the diminution of the accessible ECSA. Based on these considerations, they hypothesized that the stimulation of the fuel cell through periodically modulated back pressure in a certain frequency range and the analysis of the voltage response could lead to the isolation of the contribution of the liquid water and gas transport dynamics. Unfortunately, they were not able to practically realize their idea. However, they developed a Fault Detection and Isolation (FDI) algorithm where the cathode back pressure and voltage oscillations were used as symptom to differentiate flooding from cathode and anode starvation [165]. Years later, a theoretical work of Grübl et al. [166] investigated in deep the diagnostic capabilities of the application of pressure sinusoidal modulations at different frequencies on a generic electrochemical cell (i.e. fuel cells, metal air batteries, electrolyzers) considering the two possible electric responses. They considered

also the reverse scenarios of perturbing the system by electrical variables and detecting the consequent back pressure changes in the outlet. They named the new FRA technique electrochemical-pressure impedance spectroscopy (EPIS). The simulated spectra of the obtained transfer functions were highly influenced from geometrical features of the cell and more sensitive to mass transport parameters than classic EIS. They validated their findings through the experimental results displayed in the work of Hartman et al. [167] who applied the concept of EPIS to an oxygen metal air battery system detecting the variations of oxygen pressure in the outlet during EIS experiments. Engebretsen et al. [5] were the first to apply EPIS to a PEMFC developing a setup capable to generate sinusoidal back pressure stimulation using a loudspeaker arrangement collocated at the cathode outlet. The amplitude of the EPIS transfer function, which was obtained considering only the voltage as response, resulted to increase along with cell polarization due to decrease of oxygen partial pressure at catalyst interface. The EPIS spectra also showed a significant sensitivity to the humidification level of the anode and cathode feeds. This suggests that the effect of reactants starvation and water imbalances can be measured by EPIS providing complementary information to EIS.

A couple of novel diagnostic tools for PEMFCs inspired by the concept of TI have been further proposed. In a new work of Engebretsen et al. [6], the novel electrothermal-impedance spectroscopy (ETIS) has been applied on an open cathode cell as case study. The technique consists of imposing a periodic electrical stimulation to a PEMFC and measuring the consequent local surface temperature response. The latter is monitored through an infrared thermal imaging camera pointed on the open cathode flow fields. This way, the local heat generation within the different components can be determined together with the thermal conduction properties of the materials. ETIS allows to identify current dependent phenomena which change thermal conductivity, as for example water generation and accumulation within the GDL and under the lands. Conversely, it does not detect current independent effects like hot spots due to pinholes in the membrane which can be identified by DC thermography. Therefore, ETIS and DC thermography can be considered complemetary techniques.

Rasha et al. [168] introduced another thermography based FRA technique with the aim of mapping the water distribution named lock-in thermography (LIT). This methodology involves the application of a sinusoidal heat pulse on one side of the fuel cell and the monitoring of the temperature changes on the other side. The heat pulse is obtained by using a printed circuit board arrangement integrated with a Peltier device, while a thermal imaging camera is employed to measure the temperature changes. By varying the modulation frequency of the imposed heat stimulus, it is possible to observe water build up within the cell through the determination of the phase shift of the LIT transfer function. The mapped water distribution at different humidity and steady state current densities are consistent with the results obtained in literature using neutron imaging which shows water accumulation in the bends of serpentine flow fields and towards the outlet. Additionally, they states that the LIT has the advantage to be substantially cheaper than neutron imaging.

A more accurate FRA tool to detect water generation is the hydro-electrochemical

impedance imaging (HECII) which implies a small sinusoidal current perturbation at different frequencies to the cell, and the measurement of the water thickness variation across the active area obtained using neutron radiography [169]. The distribution of the phase shift and the amplitude of the obtained transfer function indicate the location of liquid water generation. Compared to steady state neutron imaging, EHCII is capable to distinguish legacy of water accumulated in the system over time and water recently generated by reactions.

3.2 Concentration-alternating frequency response analysis
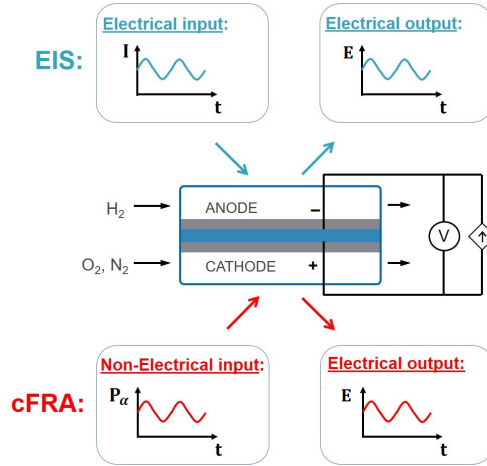
Figure 3.2: General scheme of CFRA experiment for a PEMFC system.

Following the example of the novel techniques described in the previous sections, we propose a novel FRA methodology alternative to EIS so called concentration-alternating frequency response analysis (CFRA) for the study of PEMFC dynamics and diagnosis. CFRA involves a feed with a modulated concentration of a certain sent to the fuel cell at different modulation frequencies (Figure3.2). The detected electrical response, i.e. current or voltage, depends on the electric control regime applied to the cell which is respectively voltastatic and galvanostatic. In this way, for a given modulation of a reactant α, a galvanostatic and voltastatic transfer function ζ is obtained:

$$\zeta_{I,\alpha}\left(i\omega\right) = \frac{\tilde{E}\left(i\omega\right)}{\tilde{C}_{\alpha}\left(i\omega\right)} \tag{3.16}$$

$$\zeta_{E,\alpha}\left(i\omega\right) = \frac{\tilde{I}\left(i\omega\right)}{\tilde{C}_{\alpha}\left(i\omega\right)} \tag{3.17}$$

It is expected that the effects of mass transport phenomenon and reaction steps influenced by the concentration variation should be isolated from the other processes allowing specific analysis on the fuel cell performance losses. In the following chapters, these assumption is verified through modeling and experimental studies on PEMFCs. The concept of CFRA can be applied to all the open electrochemical systems, i.e. metal air batteries, electrolyzers and electrochemical reactors.

Chapter 4

Model based analysis of CFRA methodology

In this chapter, a model based analysis to investigate theoretically the capability of CFRA to study PEMFC dynamics is reported. First, a 1-D dynamic model of a PEMFC has been developed (Section 4.1) and validated by comparison with experimental EIS spectra collected under various operation regimes (Section 4.2.1). Then, CFRA spectra have been simulated at the same operating conditions considering perturbations of oxygen and water partial pressure sent to the cathode side as input (Section 4.2.2). The possibility to separate the contributions of different type of dynamic processes to the cell performance and get new insights on the dynamics of the system is evaluated. Moreover, a sensitivity and collinearity analysis with respect to kinetic and transport parameters is performed in order to evaluate the performance of the new technique for parameter estimation (Section 4.3). Finally, a feasibility analysis is carried out to identify an operating conditions window to perform CFRA experiments guaranteeing detectability and linearity of the electrical response (Section 4.4).

4.1 PEM Fuel Cell Model

4.1.1 General assumptions

A schematic representation of the structure and of the different domains which constitute a PEMFC is displayed in Figure 4.1. The coordinate system, the position of the interfaces between the layers, as well as the considered stoichiometry of the electrochemical reactions are indicated. The main physical processes which influence the transient performance of a PEMFC are the following: (i) the charging/discharging of the double layer at the electrode surface occurring in parallel with electrochemical and adsorption/desorption reaction steps, (ii) the mass transport of the gaseous reactants and of the produced liquid water in the cathode electrode layers (channel+GDL+catalyst layer), (iii) the water sorption and the consequent hydration of the Nafion membrane.
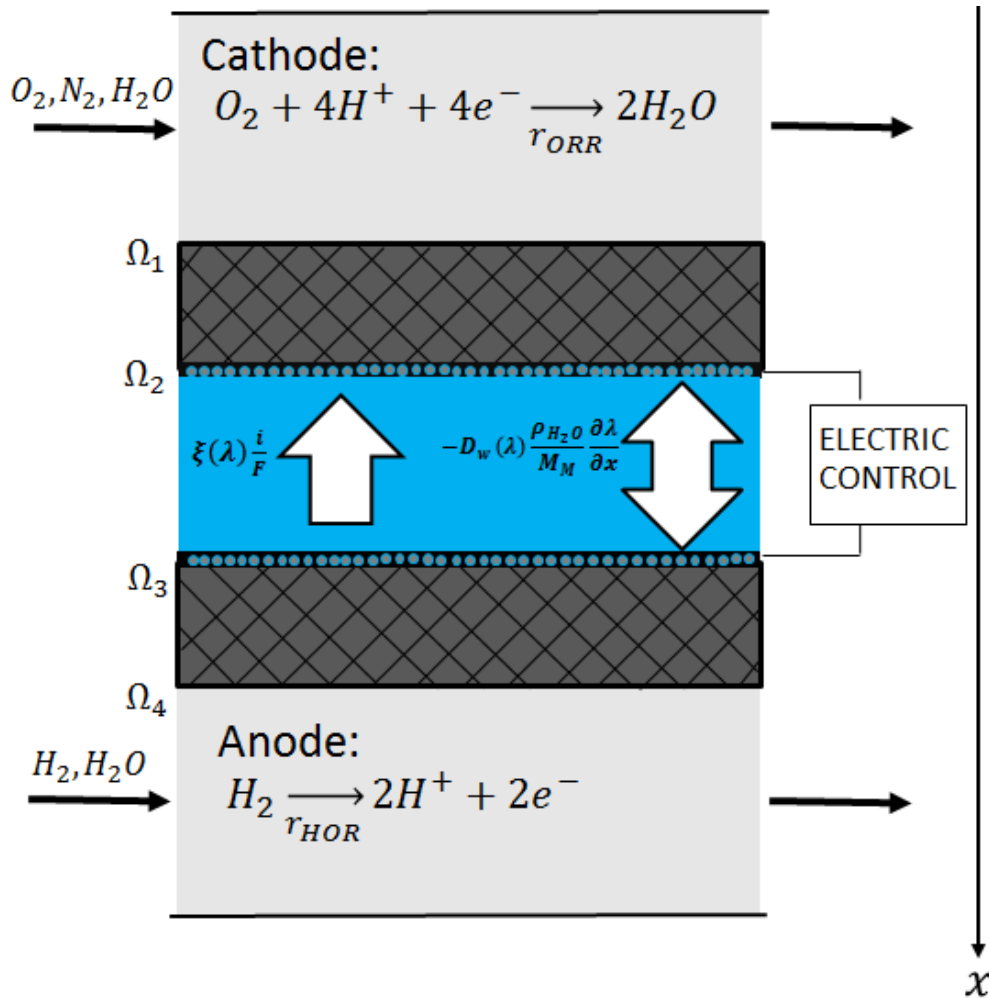
Figure 4.1: Scheme of a PEMFC.

In the formulated model description, all dynamic phenomena mentioned above are considered except for the transport of the liquid water in the electrodes. This assumption limits the predictive power of the model to those operating conditions where the water condensation effects are negligible.

The accumulation of water in the electrode decreases the porosity of the GDL dramatically increasing the mass transport resistance. Different literature studies performed by using neutron imaging techniques have evaluated the effect of the liquid water formation and retention in the GDL considering operating conditions and cell geometry similar to the ones of the experiments presented in this dissertation [170, 171]. In particular Zhang et al. [171] concluded that the volume occupied from the liquid water in the porous structure of the GDL has mostly a negligible effect on the overall performance of the fuel cell at current densities below 400 mA cm^{-2}, as the accumulation of water drops in the electrode is not significant. Since the humidity of the feed

set in the reported experiments is lower than the the one in the cited work and current density up to 300 mA cm^{-2} are taken into account, the presence of liquid water is expected to be negligible in these cases as well. However, it must be remarked that the main feature determining the quantity of water retained in the porous electrodes is the GDL material which could determine a dramatic increment of mass transport resistance even at low current densities [15].

In any case, as seen in the Section 2.2.3, the effect of water accumulation in the GDL is detected in the middle frequency arc of the impedance. This phenomenon influences the size of the arc , but it is not generating this pattern which is actually caused by the dynamics of the gas transport in the cathode channel. Therefore, two facts can be concluded: (i) the neglecting of the liquid water does not change qualitatively the linear dynamic response of a PEMFC, (ii) its effect can be just evaluated by fitting parameters directly influencing the mass transport resistance, as for example the effective porosity of the GDL.

Dynamic mass balances have been formulated for all the gaseous chemical species contained in all the compartments of the fuel cell. Concentration variations along the sandwich coordinate x are accounted, while along the axial coordinate the composition is considered constant. Moreover, isothermal and isobaric conditions are assumed.

To relate the effects of the different transport phenomena to the electric responses, a dynamic charge balance at the catalyst surface has been developed. Realistic boundary conditions connect the dynamics of the different compartments of the cell have been formulated.

In the following subsections, more detailed information about the assumptions and the model equations describing the transport of neutral and charged species along the different domains are given.

4.1.2 Mass balances in channel and GDL

The channels are treated as a perfectly mixed compartments of volume V, with inner gas composition equal to the one at the outlet. In these compartments, the sink term is represented by the gas flux J_α entering the GDL at the interfaces Ω_1 and Ω_4 (see Figure 4.1). Accordingly, the dynamic mass balance for a generic chemical compound α in the channel in terms of partial pressure P_α reads:

$$V\frac{\mathrm{d}P_\alpha^{CH}}{\mathrm{d}t} = P_{\alpha,in}^{CH}F_{in} - P_\alpha^{CH}F_{out} - RTA_{cell}J_\alpha|_{\Omega_i,t} \quad i = 1, 4. \tag{4.1}$$

where the symbol A_{cell} stands for the geometric area of the electrode, while F_{in} and F_{out} are respectively the inlet and outlet volumetric flow rates of reactants or products. Taking advantage of the assumption of isobaric conditions, the outlet flow rate F_{out} is obtained by summing up the channel mass balances of all the species for each side. Therefore, the following expression is obtained:

$$F_{out} = F_{in} - \frac{RTA_{cell}}{P_{tot}} \cdot \sum_{\alpha=1}^{n} J_\alpha|_{\Omega_i,t} \quad i = 1, 4. \tag{4.2}$$

The meaning of the other symbols can be found in the List of Symbols.

According to these assumptions, dynamic effects related to this cell compartment like the channel impedance are attributed to a uniform transport of reactants without significant gradients along the sandwich axial coordinate. This well reproduce the situation when medium-high flow rates of the feeds are used [124, 125].

The main mechanism of transport considered in the GDL is diffusion. While most models in the past considered only diffusive transport in the GDL [172], newer works include also the convective flow [173]. The contribution of both fluxes has been also addressed by Benziger et al. [174], who gave an estimation of the relevance of the convective compared to the diffusive mass transfer in the GDL. They concluded that the oxygen transport in the GDL is governed by both diffusion and convection whose the coupled effect can be described by the following equation:

$$J_{O_2} = \frac{P_{tot}}{RT} \frac{\epsilon}{\tau_t} \left(\frac{x_{O_2}}{x_{N_2}} D_{N_2} + D_{O_2} \right) \frac{\mathrm{d}x_{O_2}}{\mathrm{d}x}. \tag{4.3}$$

Assuming that the tortuosity factor is expressed as $\tau_t = \sqrt{1/\epsilon}$ (Bruggemann's correlation for the effective diffusivity), the Equation 4.3 gives:

$$J_{O_2} = \frac{1}{RT} \epsilon^{1.5} \left(\frac{P_{O_2}}{P_{N_2}} D_{N_2} + D_{O_2} \right) \frac{\mathrm{d}P_{O_2}}{\mathrm{d}x}. \tag{4.4}$$

In the Equation 4.4, the first term in the parenthesis from left gives the contribution of the convective transport, while the second one of diffusive transport. Assuming air cathode stream, one can estimate that the ratio between the first and the second term is 0.26 corresponding to ca. 4 times lower rate of convective compared to the diffusive transport which results to be the dominant one. In this case, the flux of oxygen as expressed in the Equation 4.4 is described by the Fick's law.

The diffusion flux of the ternary O_2-N_2-H_2O mixture is usually described by the Maxwell-Stefan approach. However, it has been found that the Fick's law describes pretty well this ternary system as well, when humidified air is used as oxidant [175]. According to these assumptions, the mass balance for the GDLs reads:

$$\frac{\partial P_\alpha^{GDL}}{\partial t} = -\frac{\partial J_\alpha^{GDL}}{\partial x} = D_{\alpha,\beta}^{eff} \frac{\partial^2 P_\alpha^{GDL}}{\partial x^2} \tag{4.5}$$

The effective diffusivity $D_{\alpha,\beta}^{eff}$ is expressed in accordance to the Bruggemann correlation:

$$D_{\alpha,\beta}^{eff} = \epsilon^{1.5} D_{\alpha,\beta}. \tag{4.6}$$

The diffusion coefficients of each component of the cathode gas mixture (humidified air) are determined according to the following equation introduced by Fairbanks and Wilke [176]:

$$D_{\alpha,air} = \frac{1}{\frac{y_\beta}{D_{\alpha,\beta}} + \frac{y_\gamma}{D_{\alpha,\gamma}}} \tag{4.7}$$

where y_α indicates the molar fraction of a generic component α of the gas mixture.

On the anode side, the stream is composed by a binary mixture of H_2 and water which is well described by a binary Fick's law as well.

The catalyst layer is considered as an interface where the electrochemical reactions occur immediately. The mass balance related to this layer is constituted of boundary conditions between the GDL and the Nafion membrane which are discussed in the next sections.

4.1.3 Nafion membrane

A single phase formulation based on the Springer approach [177] is used to describe the dynamics of the Nafion membrane. Accordingly, the water content in the membrane $\lambda_{H_2O}^M$, which is defined as the ratio between the number of water molecules and the number of sulfonic sites in the membrane, is considered as variable. The relationship between the water concentration in the Nafion ($C_{H_2O}^M$) and $\lambda_{H_2O}^M$ is:

$$C_{H_2O}^M = \frac{\rho_{EW}}{m_{EW}} \lambda_{H_2O}^M \qquad (4.8)$$

where ρ_{EW} and m_{EW} are the density and the molecular weight of the Nafion membrane respectively. Then, according to the Equation 4.8, the dynamic mass balance for the water in the membrane can be expressed as follows:

$$\frac{\rho_{EW}}{m_{EW}} \frac{\partial \lambda_{H_2O}^M}{\partial t} = -\frac{\partial J_{H_2O}^M}{\partial x}. \qquad (4.9)$$

As stated in different studies [172, 178], the water flow $J_{H_2O}^M$ is mainly generated through three different mechanisms: (i) diffusion due to the water concentration gradient along the membrane, (ii) hydraulic permeation driven by the gradient of capillary pressure, and (iii) the electrosmotic flux due to the water molecules dragged by the protons migrating from the anode to the cathode side. Although both diffusive and hydraulic permeation types of water transport concurrently contribute to the water transport, one of the two mechanisms dominates depending on $\lambda_{H_2O}^M$ values. It is generally accepted that the diffusive way of transport dominates at low $\lambda_{H_2O}^M$ values while the hydraulic at high $\lambda_{H_2O}^M$ values. Yet, there is a disagreement [172, 178] about the critical $\lambda_{H_2O}^{*M}$ value which marks the transition from diffusive to hydraulic type of water transport. For example, the critical $\lambda_{H_2O}^{*M}$ value of 3 is suggested by Eikerling et al. [178], while much higher value of 14 is suggested by Weber and Newman [172]. According to Eikerling et al. [178], by following the similarity with the diffusive term, the hydraulic permeation term can be expressed in terms of water content gradient by introducing an effective diffusivity coefficient. Furthermore, by assuming the validity of electro-neutrality hypothesis in the membrane, so that the proton flow can be considered equal to the current density, one can write:

$$J_{H_2O}^M = -\left(D_{diff}^{eff,M} \left(\lambda_{H_2O}^M \right) + D_{hyd}^{eff,M} \left(\lambda_{H_2O}^M \right) \right) \frac{\partial \lambda_{H_2O}^M}{\partial x} - \xi \left(\lambda_{H_2O}^M \right) \frac{j}{F} \qquad (4.10)$$

where $D_{diff}^{eff,M}$, and $D_{hyd}^{eff,M}$ are effective diffusivities for two different mechanisms of water transport. Having this in mind, and in order to implicitly account for both types of transport mechanisms, by keeping at the same time the level of model complexity low, the Equation 4.10, for the water flux in combination with a semi-empirical expression [179] for effective water diffusivity in the Nafion membrane was used. The disadvantage of this simplification is that the effect of the pressure gradient on the water transport in the membrane cannot be described by the model. Given these assumptions, $J_{H_2O}^M$ reads:

$$J_{H_2O}^M = -D_{H_2O}^M \left(\lambda_{H_2O}^M\right) \frac{\rho_{EW}}{m_{EW}} \frac{\partial \lambda_{H_2O}^M}{\partial x} - \xi \left(\lambda_{H_2O}^M\right) \frac{j}{F}. \tag{4.11}$$

The dependence of the water diffusivity in the membrane $D_{H_2O}^M \left(\lambda_{H_2O}^M\right)$ and of the electrosmotic drag constant on the water content $\xi \left(\lambda_{H_2O}^M\right)$ are respectively expressed by the following relations taken from Fuller [179] and Springer et al. [177]:

$$D_{H_2O}^M \left(\lambda_{H_2O}^M\right) = \lambda_{H_2O}^M D_{H_2O}^{0,M} exp \left(-\frac{2436}{T}\right) \tag{4.12}$$

$$\xi \left(\lambda_{H_2O}^M\right) = K_{H^+} \lambda_{H_2O}^M. \tag{4.13}$$

The Equation 4.12 is a semi-empirical relation derived by fitting of the experiments displayed in the work of Zawodzinski et al. [180].

The potential loss due to the ohmic resistance related to the transport of protons in the Nafion membrane is strongly dependent on the total water content. To account for this effect, the potential loss $\Delta \Phi_{H^+}$ is calculated by integrating the local electric field along the membrane

$$\Delta \Phi_{H^+} = j \int_0^{l^M} \frac{1}{\kappa_{H^+} \left(\lambda_{H_2O}^M\right)} \, dx. \tag{4.14}$$

The membrane conductivity κ_{H^+} is expressed as function of the water content by the following relation [177]

$$\kappa_{H^+} = \left(0,005139\lambda_{H_2O}^M - 0,00326\right) exp \left(1268 \left(\frac{1}{303} - \frac{1}{T}\right)\right). \tag{4.15}$$

4.1.4 Charge balance

Charge balances at the catalyst layers interfaces have been formulated by considering the double layers acting as capacitors in parallel to charge transfer resistances due to the electrochemical reactions. The resulting equations for both anode and cathode sides read

$$C_c^{DL} \frac{d\eta_c}{dt} = -j + 4F r_{ORR} \tag{4.16}$$

45

$$C_a^{DL}\frac{\mathrm{d}\eta_a}{\mathrm{d}t} = j - 2Fr_{HOR}. \tag{4.17}$$

The variable η stands for the overpotential, while C^{DL} is the double layer capacitance. The balance is formulated according to the reaction stoichiometry shown in Figure 4.1. Because of the assumption of the fast transport in the catalyst layer, the charge balance is not spatially distributed. One step ORR and HOR mechanisms are assumed. The expressions taken from various studies in the literature read [181–183]:

$$r_{ORR} = \frac{P_{O_2}^{CL}}{RTC_{O_2,ref}}t_c^{CL}ai_0exp\left(-\frac{\alpha_c F}{RT}\eta_c\right) \tag{4.18}$$

$$r_{HOR} = \frac{k_{HOR}\left(P_{H_2}^{CL}\right)^{1/2}}{2\sqrt{K_{H_2,ad}}}sinh\left(\frac{\alpha_a F}{RT}\eta_a\right). \tag{4.19}$$

The kinetic rate of the ORR r_{ORR} is a simplified version of the Butler-Volmer equation obtained neglecting the anodic contribution to the electrochemical reaction. The order of the kinetics with respect to the oxygen is assumed to be one, as stated in the work of Wang et al. [181]. On the other hand, the kinetic expression for the HOR r_{HOR} proposed in the work of Zhang et al. [182] has been used. It considers a Tafel-Volmer mechanism consisting in a dissociative adsorption of H_2 followed by the electrochemical oxidation of the adsorbed hydrogen atoms. The adsorption step characterized by an equilibrium constant $K_{H_2,ad}$ is assumed to be in quasi-equilibrium, while the rate of the electrochemical step determined by the rate constant k_{HOR} obeys to the Butler-Volmer law. The meaning of all the other terms in kinetic expressions can be read in the List of the Symbols.

To relate the voltage E of the fuel cell to the various overpotential and ohmic losses, a polarization equation obtained by application of the Kirchhoff's voltage law is formulated:

$$E = E_{OCP} - \eta_a + \eta_c - \Delta\Phi_M \tag{4.20}$$

where E_{OCP} is the open circuit voltage. The current density i is implicitly given in the Equation 4.20, so that this expression can be used to determine the total voltage or the current provided by the cell depending on the electric control we consider, i.e. galvanostatic (fixed current) or voltastatic (fixed potential).

4.1.5 Boundary conditions

The developed model consists of six second order partial differential equations (PDE): five spatially distributed mass balances for all the components of the gas mixture in the GDLs (three for the cathode and two for the anode side), and an additional PDE related to the water transport in the membrane. Therefore, the formulation of twelve boundary conditions (BC) is required to solve the set of equation. Additionally, the two ordinary differential equations (ODE) constituting the charge balance must be accounted.

As shown in the Figure 4.1, the interfaces between the gas channels and GDLs are labelled as Ω_1 ans Ω_4, respectively standing for the cathode and the anode side. The continuity of the partial pressure between these two domains is chosen as boundary condition, so that we obtain:

$$P_\alpha^{GDL}\big|_{x=\Omega_1,t} = P_\alpha^{CH} \tag{4.21}$$

$$P_\alpha^{GDL}\big|_{x=\Omega_4,t} = P_\alpha^{CH}. \tag{4.22}$$

As already mentioned, the catalyst layer is considered as an interface where the reaction occurs as soon as the reactants reach it. On the cathode, this means that the oxygen diffusive flux equals the rate of the oxygen consumption at this interface. Therefore, the BC for the oxygen pressure reads:

$$-\frac{D_{O_2,air}^{eff}}{RT}\frac{\partial P_{O_2}^{GDL}}{\partial x}\bigg|_{x=\Omega_2,t} = r_{ORR}. \tag{4.23}$$

Since nitrogen does not participate to the ORR, the gas is stagnant, and the following condition is valid:

$$-\frac{D_{N_2,air}^{eff}}{RT}\frac{\partial P_{N_2}^{GDL}}{\partial x}\bigg|_{x=\Omega_2,t} = 0. \tag{4.24}$$

For the water case, the steady balance at the catalyst layer is formulated taking into account the water produced by the ORR, the one incoming by the electrosmotic flow, and the water coming out through the diffusion across the Nafion membrane. Then, the following equation is obtained:

$$-\frac{D_{H_2O,air}^{eff}}{RT}\frac{\partial P_{H_2O}^{GDL}}{\partial x}\bigg|_{x=\Omega_2,t} + 2r_{ORR} = -D_{H_2O}^M\left(\lambda_{H_2O}^M\right)\frac{\rho_{EW}}{m_E W}\frac{\partial \lambda_{H_2O}^M}{\partial x}\bigg|_{x=\Omega_2,t}$$
$$-\xi\left(\lambda_{H_2O}^M\right)\frac{j}{F}. \tag{4.25}$$

On the anode, analog assumptions have been contemplated. Accordingly, the BC for the partial pressure of hydrogen at the catalyst interface reads:

$$-\frac{D_{H_2,H_2O}^{eff}}{RT}\frac{\partial P_{H_2}^{GDL}}{\partial x}\bigg|_{x=\Omega_3,t} = r_{HOR}. \tag{4.26}$$

Since, there is no water produced by the HOR, the water crossing the membrane from the cathode side by diffusion and the electrosmotic flow are the only fluxes to be accounted in the balance. Then, the following BC is formulated:

$$-\frac{D_{H_2O,H_2}^{eff}}{RT}\frac{\partial P_{H_2O}^{GDL}}{\partial x}\bigg|_{x=\Omega_3,t} = -D_{H_2O}^M\left(\lambda_{H_2O}^M\right)\frac{\rho_{EW}}{m_E W}\frac{\partial \lambda_{H_2O}^M}{\partial x}\bigg|_{x=\Omega_3,t}$$
$$-\xi\left(\lambda_{H_2O}^M\right)\frac{j}{F}. \tag{4.27}$$

47

At the catalyst/Nafion interface, the water vapour is considered in equilibrium with the water inside the Nafion membrane. According to that, as BCs for the water balance in the Nafion membrane, the isothermal water uptake equation is considered on both sides [177]:

$$\lambda_{H_2O}^M = 0,043 + 17,81 \left.\frac{P_{H_2O}^{CL}}{P_{sat}}\right|_{x=\Omega_i,t} - 39,85 \left.\frac{P_{H_2O}^{CL}}{P_{sat}}\right|_{x=\Omega_i,t}^2 + 36 \left.\frac{P_{H_2O}^{CL}}{P_{sat}}\right|_{x=\Omega_i,t}^3$$
(4.28)

where $i = 3, 4$.

4.2 Simulation of EIS and CFRA spectra

The model compiled in the previous section has been discretized, and numerically solved in MATLAB® environment at different steady state conditions. Then, the obtained nonlinear differential algebraic equations (DAE) system has been linearized around steady state points in order to obtain a linear state space system representation in matrix form (Equations 3.3-3.4). After that, the desired transfer functions have been calculated with a help of the Equation 3.9. This procedure allows to avoid nonlinear contributions and to not concern about the amplitude of the perturbation applied.

As already mentioned, the main purpose of this modeling study is to theoretically investigate the capability of the CFRA as methodology to study the PEMFCs dynamics and for diagnosis. Most of the performance losses are related to processes taking place on the cathode and to the hydration state of the Nafion membrane. For this reason, oxygen and water concentration perturbations sent to the cathode side have been considered as input. As all the components of the feed are in gas phase, it is reasonable to express the concentration variation in terms of partial pressure. Therefore, performing the experiments under galvanostatic and voltastatic conditions, the following four transfer functions can be determined:

$$\zeta_{I,O_2}(i\omega) = \frac{\tilde{E}(i\omega)}{\tilde{P}_{O_2}(i\omega)}$$
(4.29)

$$\zeta_{I,H_2O}(i\omega) = \frac{\tilde{E}(i\omega)}{\tilde{P}_{H_2O}(i\omega)}$$
(4.30)

$$\zeta_{E,O_2}(i\omega) = \frac{\tilde{I}(i\omega)}{\tilde{P}_{O_2}(i\omega)}$$
(4.31)

$$\zeta_{E,H_2O}(i\omega) = \frac{\tilde{I}(i\omega)}{\tilde{P}_{H_2O}(i\omega)}$$
(4.32)

In the following, prior to a preliminary model validation, the results of the simulation of the CFRA experiments are discussed in detail.

4.2.1 Model validation

In order to verify the capability of the model to predict the dynamics of a PEMFC, EIS spectra have been simulated and compared to experimental ones. The operating conditions of the experiments together with the values of the parameters used in the model are listed in the Table 4.1. These have been chosen in order to match as much as possible the assumption made in the model.

Quantity	Value	Source
ai_0 Product of specific catalyst area and exchange current (A m^{-3})	10^4	[182]
A_{cell} Geometric surface area of the catalyst (m^2)	2.6×10^{-3}	Experiments
C^{DL} Double layer capacitance for cathode and anode (F m^{-2})	500	Assumed
$C_{O_2,ref}$ Reference concentration O$_2$2 (mol m^{-3})	40	[182]
$D_{H_2O,air}$ Diffusivity for H$_2$O (m^2 s^{-1})	1.14×10^{-5}	[175]
$D_{N_2,air}$ Diffusivity of N$_2$ (m^{2}s^{-1})	3.07×10^{-5}	[175]
$D_{O_2,air}$ Diffusivity of O$_2$ (m^2 s^{-1})	1.42×10^{-5}	[175]
$D_{H_2O}^{0,M}$ Nominal diffusivity of water in Nafion (m^2 s^{-1})	2.1×10^{-7}	[177]
E_{ocp} Open circuit potential (V)	1.2	Assumed
$F_{in,c}$ Gas flow rate at cathode (m^3 s^{-1})	6.94×10^{-6}	Experiments
$F_{in,a}$ Gas flow rate at anode (m^3 s^{-1})	4.4×10^{-6}	Experiments
K_{ad,H_2} Kinetic constant for hydrogen adsorption (Pa)	5.07×10^4	[182]
K_{HOR} Kinetic constant for hydrogen oxidation (mol m^{-2} s^{-1})	4.15×10^{-1}	[182]
K_{H^+} Electrosmotic drag constant	2.5	[177]
P_{tot} Total pressure (Pa)	10^5	
$P_{O_2,in}^{CH}$ Oxygen pressure of the cathode inlet (Pa)	1.58×10^4	Experiments
$P_{H_2,in}^{CH}$ Hydrogen pressure of the anode inlet (Pa)	7.51×10^4	Experiments
t_c^{CL} Cathode catalyst layer thickness (m)	10^{-6}	[182]
T Temperature (K)	353	Experiments
$T_{dp,a}$ Dew point temperature anode (K)	328	Experiments
$T_{dp,c}$ Dew point temperature cathode (K)	328	Experiments
V Volume of the flow field (m^3)	7.2×10^{-6}	Experiments
α_a Charge transfer coefficient at the anode	0.5	Assumed
α_c Charge transfer coefficient at the cathode	0.55	Assumed
ε_{H_2O} Porosity of the GDL related to H$_2$O	0.3	Assumed
ε_{O_2} Porosity of the GDL related to O$_2$	0.034	Assumed

Table 4.1: List of input parameters

Feeds with low RH (35%) have been set in order to keep the membrane in a dehydrated state. In this way, the contribution to the performance of the ohmic resistance due to the low proton conductivity, and of the water transport in Nafion are expected to be more significant. The employed high hydrogen flow rate makes more efficient the water removal on the anode side promoting a substantial backwards permeation of water in the membrane. Moreover, the condensation of liquid water is likely to be minimal because of the relatively low steady state current density (maximum 300 mA

cm^{-2}). Further details on the experimental conditions, the setup and the cell hardware are discussed in the Chapter 5.

In the Figures 4.2a-c, EIS experimental spectra measured at three different working points, i.e. 100 mA cm^{-2}, 200 mA cm^{-2} and 300 A cm^{-2}, are shown. These
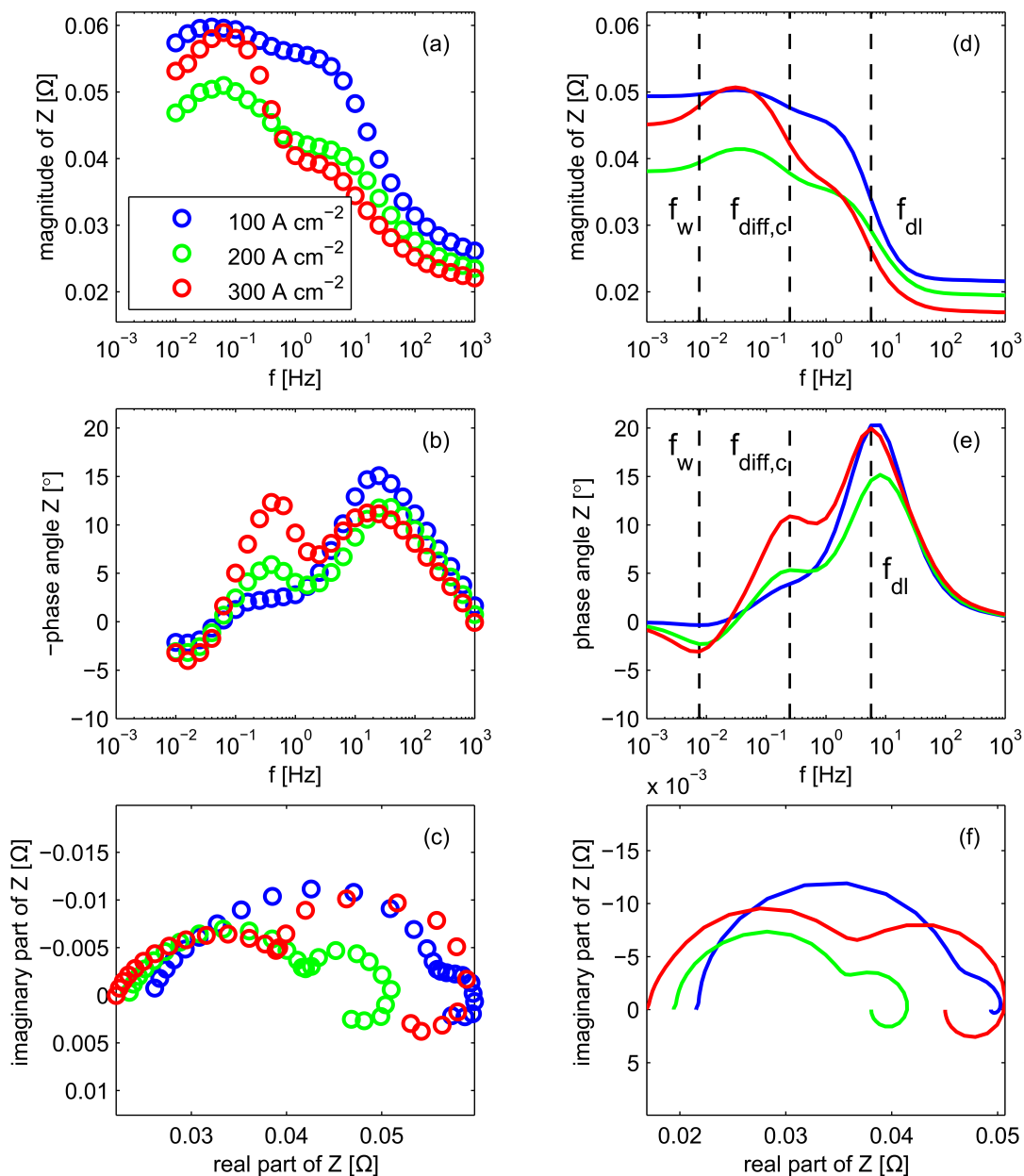
Figure 4.2: EIS spectra collected at 3 different working points. (a)-(c) experimental spectra, (d)-(f) simulated spectra.

conditions correspond to three different regimes of a PEMFC operation: activation controlled region, linear region controlled by the ohmic resistance due to the proton transport in the membrane, and a region in which the mass transport resistances start to have a more significant influence. As shown in the Figures 4.2d-f, the model reproduces well the experimental results, predicting the effects of the dominant transient processes on the spectra. Basically, three phenomena dominate the dynamics of the PEMFC, which characteristic frequencies, and, consequently, the time constants can be determined by the turning points in the phase angle diagram or by the inflection points in the magnitude Bode plot representation [76]. As illustrative example, characteristic frequencies related to the Bode plot at the highest steady state current density are shown in the Figures 4.2d-e. The effect of the kinetic charge transfer resistance on the cathode acting in parallel with the double layer charging dynamics is observed in the high frequency region ($f_{dl} = 7Hz$). As already mentioned in the Chapter 2, it is usually the fastest transient observed in PEMFCs [73, 74]. At a frequency around 248 mHz, termed as $f_{diff,c}$, the dynamics related to the gas transport inside the channel on the cathode side are detected. As shown also in other works [73, 74], the contribution of the mass transport on the anode side to the spectra is too small to be distinguished in most of the cases. Finally, in the low frequency range (larger response times) the characteristic frequency of the water sorption in the membrane ($f_w = 8mHz$) is observed [73, 74, 98, 115, 116, 132, 184].

The dynamics related to the gas transport in the GDL are not clearly observed or distinguished. As observed in other works [130], this contribution can fall in the same frequency region of the double layer charging dynamics and be overlapped with the latter. This is indeed verified in our model simulations. Then, it is reasonable to think that the same occurs in the experiments.

It should be mentioned that the present spectra are relatively easy to interpret, since the most of the observed dynamics do not overlap. As it was mentioned in the previous sections, in many cases, the overlapping of different phenomena occurs in the spectra, making difficult the investigation of the system dynamics.

4.2.2 CFRA spectra

For comparison purposes, CFRA spectra obtained by oxygen partial pressure perturbations under voltastatic control (Equation 4.31), have been simulated at the same operating conditions previously considered. The results are displayed in Figure 4.3. In the magnitude plot (Figure 4.3a), two inflections points are observed at the same characteristic frequencies previously attributed to the gas transport in the channel and to the water transport in the membrane.

The dynamics associated to the double layer charging are not visible at high frequencies. This can be rationalized by the time delay between the input signal perturbation (oxygen pressure change) and the system response in terms of current and overpotential changes. Two patterns typical of delayed systems are indeed observed in the spectra. In the phase angle plot (Figure 4.3b), the phase angle is increasing

51
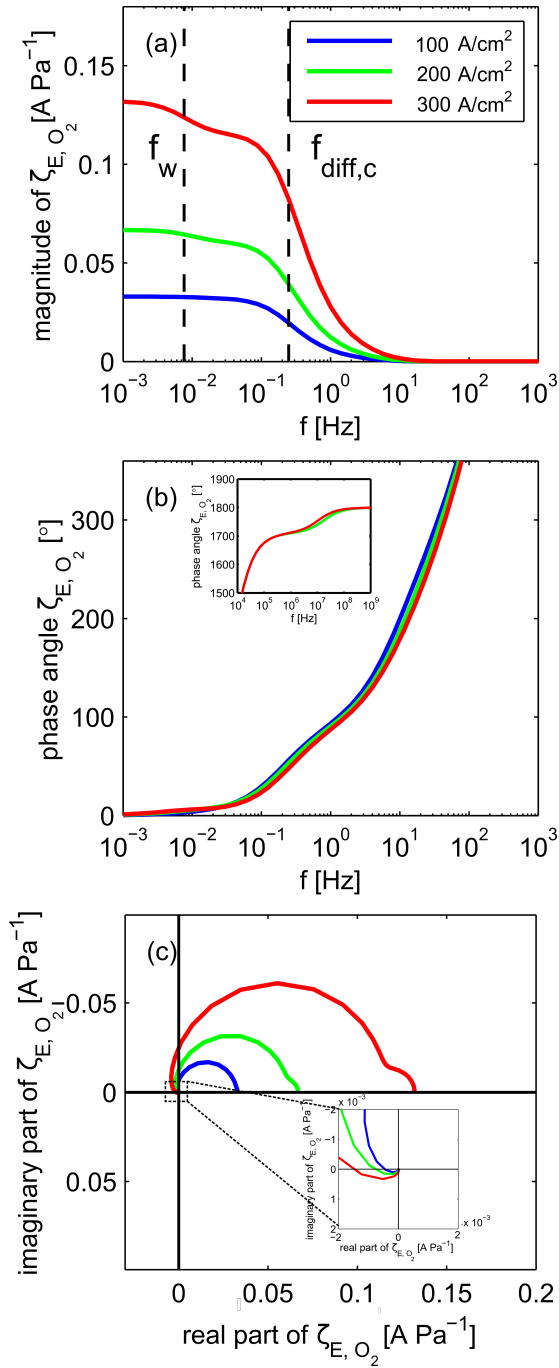
Figure 4.3: Simulated CFRA spectra obtained by oxygen partial pressure perturbations under voltastatic control at 3 different working points.

monotonously over the angle of 360°, reaching the plateau of 1800° at very high frequencies (see the inset of the Figure 4.3b). Additionally, the Nyquist plots exhibit a spiral at high frequencies (see the inset of the Figure 4.3c). It can be further assumed

that this delay should be equal to the time required for the gas to be transported inside the cathode channel and GDL, and reach the catalyst surface. This assumption can be further demonstrated as follows.

The time delay Δt of the output is related to the frequency ω_c at which in the Nyquist plot the imaginary part turns for the first time negative (see the inset of Figure 4.3c) according to the following equation [185]

$$\Delta t = \frac{\pi - tan^{-1}\omega_c}{\omega_c}. \tag{4.33}$$

The calculated time delay by the Equation 4.33 based on data in Figure 4.3c is 0.025 s. It follows further that if the time delay is influenced by mass transfer conditions in the channel and the GDL, the characteristic frequency ω_c is be dependent on the gas diffusivity, GDL porosity or its thickness.

In Figure 4.4a, the influence of oxygen diffusivity on CFRA spectra is shown in a Nyquist plot representation. As one can see, the CFRA spectra are sensitive to the change of this parameter decreasing their values as the oxygen diffusivity increases. The Figure 4.4b shows zoomed high frequency area of the CFRA spectra. As can be observed, the value of the highest frequency intercept on the real axis increases together with the diffusivity ($\omega = 10.19Hz, \omega' = 15.69Hz, \omega'' = 66.48Hz$).

This, in accordance to the equation 4.33, results in the associated time delays of $\Delta t = 0.025s$, $\Delta t' = 0.016s$, and $\Delta t'' = 0.0038s$. An increase of the time delay with a decrease of diffusivity is expected, since a lower diffusivity means a slower gas diffusion and more time to achieve the catalyst interface. It must be remarked that the calculated time delays could be underestimated, since the channel is considered as lumped element neglecting a pressure gradient along the sandwich and axial coordinate. Then, this assumption does not account for the time required to the pressure perturbation to achieve the interface between the channel and the GDL.

The magnitude of CFRA obtained under voltastatic control (solid line), and under galvanostatic control (dashed line) are compared in the Figure 4.5. Unlike the voltastatic case, the galvanostatic spectrum does not display any change in the response at the characteristic frequency for the transport of water in the membrane. The only present inflection point is the one revealing the dynamics of the gas transport in the channel. This is because the galvanostatic control implies a constant reaction rate and, consequently, a constant water production by the ORR on the cathode. This results in a steady hydration of the membrane which is not a dynamic element under this operating condition, and give a constant contribution to the ohmic resistance of the PEMFC.

This supposition is further reflected in Figure 4.6, where simulations of oxygen pressure step experiments (Figure 4.6a) are displayed. Specifically, the electric responses to the pressure stimulation under voltastatic and galvanostatic conditions are reported (Figure 4.6b) together with the dynamic behaviour of the ohmic losses due to the change of water content in the membrane (Figure 4.6c), calculated by the Equation 4.14. Under voltastatic control (Figure 4.6b, solid line), the current increases from its
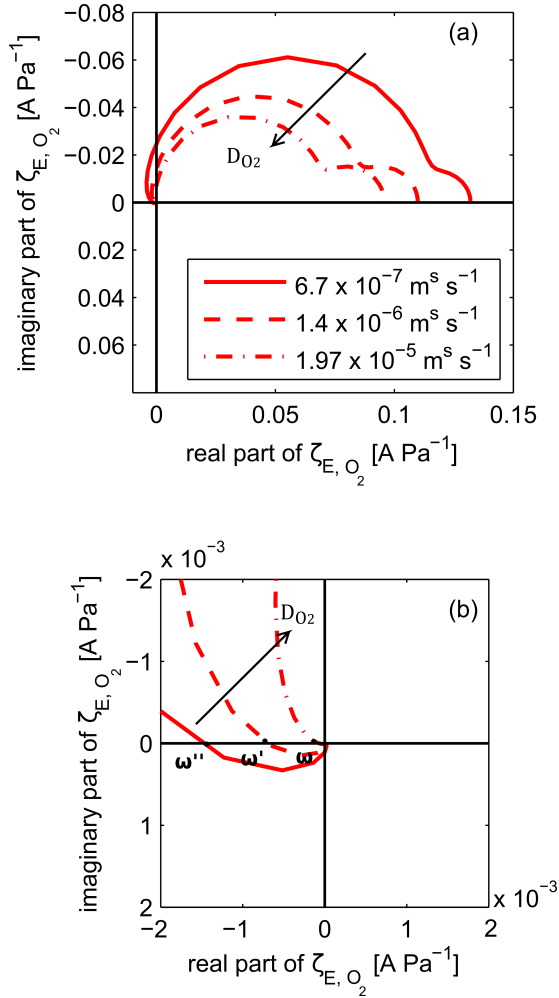
Figure 4.4: Simulated CFRA Nyquist plots obtained by oxygen partial pressure perturbations under voltastatic control at 3 different values of oxygen diffusivity. Operating current: 300 mA cm^{-2}.

initial steady state value to the intermediate new value in a time range around 1 s. At a bit longer time scale ($t > 1s$), additional increase of current can be observed, with a new steady state value reached in ca. 30s. The first change of the current at $t \approx 1s$ can be attributed to the change in the oxygen pressure due to the pressure step. The increase at $t > 1s$ is not directly related to the pressure change. This increase can be explained by a change of a membrane resistance caused by additional water transported into the membrane. The decrease of the membrane resistance under voltastatic conditions leads to an increase of the activation overpotential (cathode overpotential is mainly influenced), causing an increase of the current density. This is further demonstrated in the Figure 4.6c (solid line), where the change of the membrane resistance over time is shown. At first, the membrane resistance is increasing (due to the current
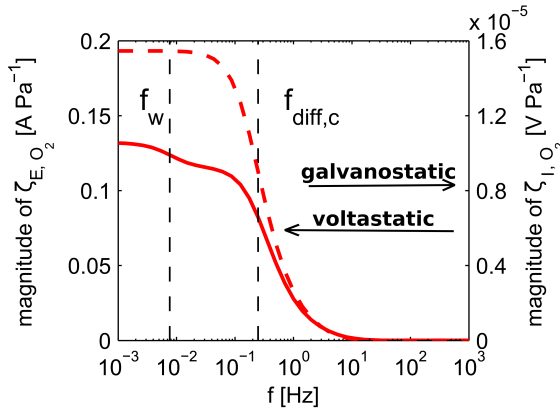
Figure 4.5: Comparison of the magnitude of CFRA in Bode plot representation obtained by oxygen partial pressure perturbations under voltastatic (solid line) and galvanostatic (dashed line) control. Operating current of 300 mA cm^{-2}.

increase), but at $t > 10s$ it starts to decrease. This time corresponds to the time constant of water diffusion in the membrane. On the contrary, the potential response stays constant at the same range of time under galvanostatic control, as well as the ohmic resistance which value does not change during the time course of the experiment (Figure 4.6b-c, dashed line). This confirms the previous speculation about the constant hydration of membrane by keeping the current constant. The present discussion suggests that the comparison between the CFRA spectra collected under galvanostatic and voltastatic conditions can be used to identify and discriminate the contribution of the membrane dynamics to the frequency response spectra and evaluate its time constant.

In the Figure 4.7, the simulated magnitude of CFRA spectra obtained by water partial pressure perturbations are reported (Equations 4.30-4.32). As already stated , in these simulations, the steady state water pressure was significantly below the saturation point (30% RH). For both electric responses, the spectra mostly detect the dynamics associated to the water transport in the membrane which gives the highest contribution to the transfer functions. The characteristic frequency clearly determinable at low frequencies is indeed the one corresponding to this phenomenon. A slight turning point is observed in the frequency range of the gas transport in the channel. The unexpected response of this transient process is related to the change of the partial pressures of the component of the gas mixture at the catalyst interface and is explained in the following.

In the Figure 4.8, simulations of water pressure step experiments are displayed. As seen in the Figure 4.8b, the diffusion of the water pressure perturbation in the GDL and catalyst interface cause also a change of the oxygen pressure. Since the oxygen pressure of the inlet flow stays constant during the experiment, this behaviour is unexpected. However, the variation of the gradient of water in the GDL affects the total volumetric flow rate at the outlet (Equation 4.2), as depicted in the Figure 4.8c. This makes the partial pressures of all the chemical species in the channel changing
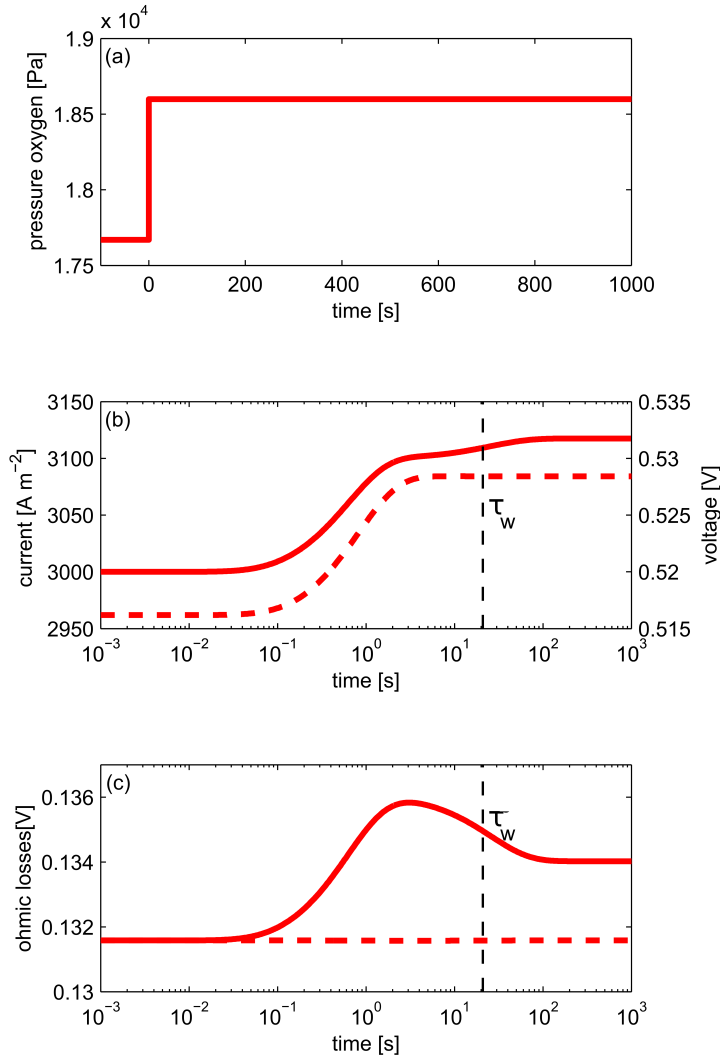
Figure 4.6: Pressure step simulations under voltastatic (solid line) and galvanostatic (dashed line) conditions: (a) oxygen pressure step signal input, (b) current (voltastatic control) and cell voltage (galvanostatic control) outputs, (c) ohmic potential losses due to proton transport in Nafion.

determining a variation in the GDL and catalyst as well. The variations related to this transients result in the detection of gas transport dynamics in the CFRA spectra obtained by water perturbation.

These simulations suggest that water perturbation can be used to study selectively the dynamics related to the Nafion membrane or, more generally, to the the phenomena connected to the water transport in the cell, as for example transport of vapour.

The previous analysis demonstrates that the CFRA capability to discriminate be-
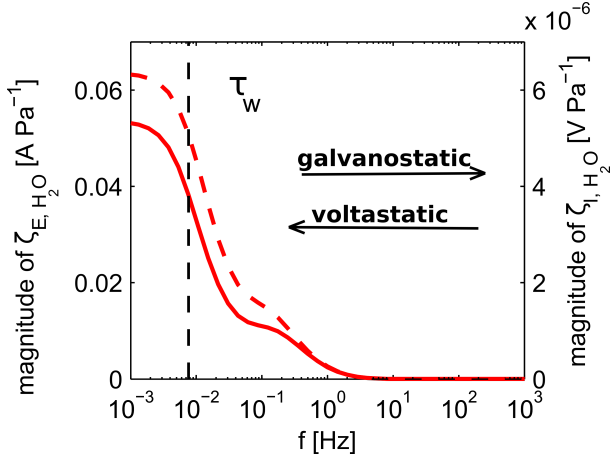
Figure 4.7: Comparison of the magnitude of CFRA in Bode plot representation obtained by water partial pressure perturbations under voltastatic (solid line) and galvanostatic (dashed line) control. Operating current of 300 mA cm^{-2}.

tween different dynamic processes is dependent not only on the chosen pressure input perturbation, but also on the electric control conditions of the experiment. This conclusion follows also from analysis of the terms of the residual vector (Equation 3.13) for all the studied frequency response methods. To rationalize the information contained in the spectra, the relative contribution of the residual r_i is expressed through the following equation

$$r_{rel,i} = 100 \frac{r_i}{\sum_{i=1}^{n} r_i}.$$ (4.34)

In the Table 4.2, the values of the relative residuals $r_{rel,i}$ for model variables related to the main accounted dynamic processes are displayed. The term r_{rel}^{DL} stands for the relative residual related to the double layer charging at the cathode side, r_{rel}^{GDL} for the oxygen transport in the GDL, r_{rel}^{CH} for the oxygen transport in the channel, and $r_{rel}^{M}(\%)$ for the transport of the water in the membrane. The relative terms are expressed in percentage. As claimed in the previous sections, the higher the value of the relative residual, the higher the impact of the dynamic process on the spectra. In the case of EIS, the values of the residuals are significant for most involved dynamic processes. These calculations agrees with the EIS spectra previously displayed, in which insights for all the main dynamics have been observed. The phenomenon with the lowest impact is the charging of the double layer, which is connected to the charge transfer resistance of the ORR. The gas diffusion in the GDL presents a higher contribution. This confirms that this phenomenon is among the most influencing, but its characteristic pattern in the spectra is masked to the one of the double layer charging and, consequently, not visible. Moreover, it is noticeable that the diffusion inside the GDL has a lower impact (20% lower) than gas transport in the channel. This agrees with the hypothesis of the transport in the channel as dominant dynamic process for gas
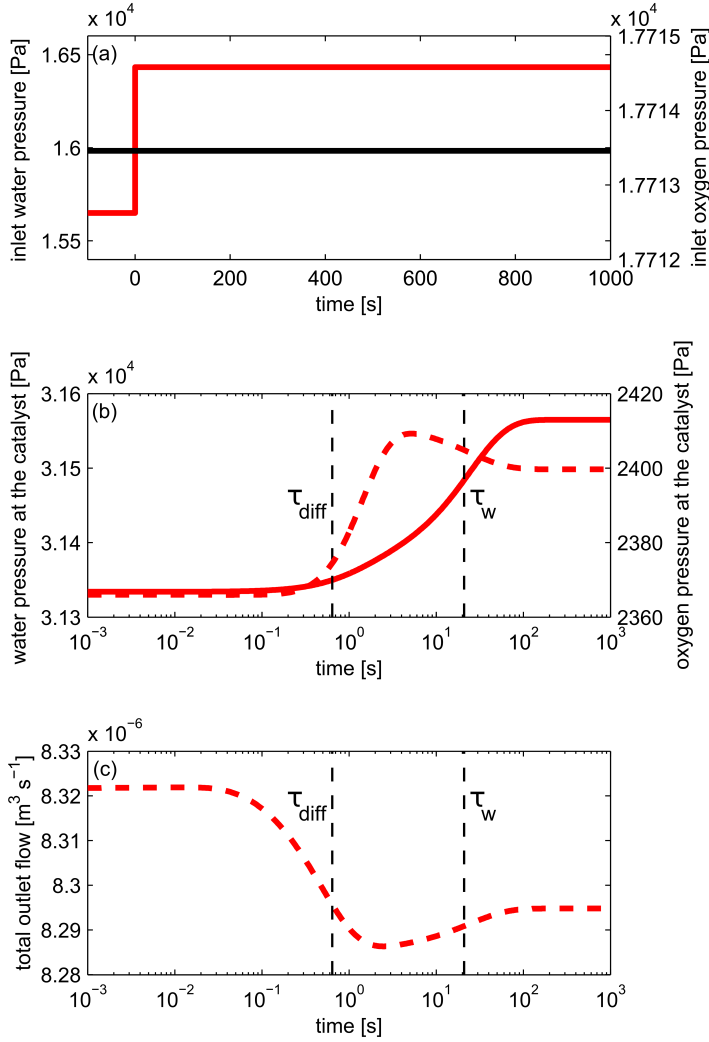
Figure 4.8: Pressure step simulations under voltastatic conditions: (a) water pressure step signal input (red line) and oxygen pressure (black line), (b) oxygen pressure (dashed line) and water pressure (solid line) change at cathode catalyst interface, (c) outlet flow rate

Technique	$r_{rel}^{DL}(\%)$	$r_{rel}^{GDL}(\%)$	$r_{rel}^{CH}(\%)$	$r_{rel}^{M}(\%)$
EIS	13.1	22.7	54.6	9.6
CFRA (O_2) vol.	0	0	87.9	11.1
CFRA (O_2) gal.	0	0	100	0
CFRA (H_2O) vol.	0	0	17.1	82.9
CFRA (H_2O) gal.	0	0	25.2	74.8

Table 4.2: Relative residual values. Operating current: 300 mA cm^{-2}.

transport. The relative residuals related to the CFRA spectra obtained by oxygen perturbation are characterized by an absent contribution of the double layer transient and of the transport in the GDL under both the electric controls. Indeed, these processes could not be identified in the CFRA spectra. Specifically, for the CFRA under galvanostatic condition, the only dynamic process detected is the transport of the oxygen in the gas channel, as observed in the simulations (Figure 4.5). Finally, the selectivity of the CFRA spectra obtained by water pressure perturbations regarding the transport in the Nafion membrane is also verified. The values of the relative residual r_M^{rel} corresponding to this phenomenon are around 80% and 75% respectively for the transfer functions determined under voltastatic and galvanostatic conditions. The rest of the contribution is given by the gas transport in the channel, as also seen in the previous simulations. Therefore, the residual matrix can be considered as valuable theoretical instrument to predict and quantify the contributions of the different dynamics to a spectrum of a certain transfer function.

4.3 Sensitivity analysis

An identifiability analysis has been performend in order to determine the quality of the parameter estimated by the fitting of CFRA and EIS spectra. In this way, the performances of the different FRA techniques as tool for the analysis and onboard diagnosis of PEMFC systems have been compared.

The main parameters accounted in the model influencing the dynamics and the performance of a PEMFC have been selected for this analysis. As parameter affecting the rate of the ORR and the double layer charging, the cathodic transfer coefficient α_c has been considered. The exchange current density i_0 has not been included in the analyzed parameters, as its change resulted to have a negligible impact on the dynamic performance. The effective porosities of the GDL related to oxygen and water transport on the cathode side, respectively ε_{O_2} and ε_{H_2O} have been chosen as parameters determining the impact of the resistance of transport in the GDL as well as the dynamics of the transport in the channel. Finally, the intrinsic diffusivity of water in Nafion $D_{H_2O}^{0,M}$ and the electrosmotic flow constant have been selected as the parameters most characterizing the effects of water transport in Nafion.

4.3.1 Mathematical framework of the identifiability analysis

The following approach to evaluate the identifiability of parameters has been largely employed in the field of chemical process engineering, and it is recently finding application in the kinetic analysis of complex chemical networks in system biology [186, 187]. To our knowledge, this is the first case of application in the analysis of the electrochemical systems.

The observation taken from EIS and CFRA experiments can be described through

the observation equation:

$$\boldsymbol{O} = \phi\left(\boldsymbol{\theta}\right) + \boldsymbol{L}. \tag{4.35}$$

The observation vector $\boldsymbol{O} = (O_1, ...O_n)^T$ contains in our case the values of the considered CFRA or EIS transfer functions measured at different frequencies. On the other hand, $\phi\left(\boldsymbol{\theta}\right) = (\phi\left(\boldsymbol{\theta}\right)_1, ...\phi\left(\boldsymbol{\theta}\right)_n)^T$ represents the simulated results obtained using the parameter set $\boldsymbol{\theta} = (\theta_1, ...\theta_m)^{(}T)$, while $\boldsymbol{L} = (L_1, ...L_n)^{(}T)$ is the observation error vector which elements quantify the difference between the experiments and model predictions. The latter vector is relevant for assessing the adequacy of the parameter estimated, but not for their identifiability.

A given subset K of parameter has to fulfill two requirements to be identifiable. First, the simulated outputs $\phi\left(\boldsymbol{\theta}\right)$ must be sensitive to the change of all parameters of the subset. Second, the change of the output due to the modification of a parameter should not be compensated by the change of value of another parameter from the subset. The first criteria is addressed by the determination of the sensitivity coefficients and their mean square value δ_j^{msqr} for each parameter θ_i, while the second by the calculation of collinearity index λ_K related to the subset K considered. Both variables are function of the normalized sensitivity matrix $\tilde{\boldsymbol{S}}_{\boldsymbol{p}}$ which is in turn calculated through the elements $s_{i,j}$ of the adimensional sensitivity matrix $\boldsymbol{S_p}$ expressed by the following equation:

$$s_{i,j} = \frac{\theta_j^0}{\phi_i^0}\frac{\partial\phi_i}{\partial\theta_j}. \tag{4.36}$$

Here, the index i stands for a certain measured output which is the values of a transfer function at a certain frequency in our specific case, while the index j indicates the parameter considered. The derivative in the Equation 4.36 has been determined with respect to a fixed parameter set $\boldsymbol{\theta_0}$. The elements ϕ_j^0 and θ_i^0 are respectively the output of the model calculated from the parameter set $\boldsymbol{\theta_0}$ and its ith element. In general, a high sensitivity implies a smaller variance in the measure of a certain parameter, resulting in a more correct estimation. Therefore, in the present context, the value of the sensitivity coefficient represents a comparative term with respect to the quality of the parameter estimation performed using different FRA techniques.

Then, the elements of the normalized sensitivity matrix $\tilde{\boldsymbol{S}}_{\boldsymbol{p}}$ are constituted by the normalized elements of $\tilde{\boldsymbol{S}}_{\boldsymbol{p}}$ which read:

$$\tilde{s}_{i,j} = \frac{s_{i,j}}{\|\boldsymbol{s_j}\|}. \tag{4.37}$$

The symbol $\|\boldsymbol{s_j}\|$ indicates the Euclidean norm of the jth colums of the nondimensional sensitivity matrix $\boldsymbol{S_p}$. From the elements of $\tilde{\boldsymbol{S}}_{\boldsymbol{p}}$, the mean square sensitivity δ_i^{msqr} related to a certain parameter $\boldsymbol{\theta_j}$ is determined through the following equation:

$$\delta_j^{msqr} = \sqrt{\frac{1}{n}\sum_{i=1}^{N} s_{i,j}^2}. \tag{4.38}$$

A high value of δ_i^{msqr} means that the parameter θ_j has an average high influence over all the simulated outputs ϕ_i, while a value approaching the zero indicates its change has a negligible effect.

The collinearity index γ_K related to a parameter subset K is defined as:

$$\gamma_K = \frac{1}{min \left(eigen \left(\tilde{\boldsymbol{S}}_{\boldsymbol{p},\boldsymbol{K}}^T \tilde{\boldsymbol{S}}_{\boldsymbol{p},\boldsymbol{K}} \right) \right)} = \frac{1}{\lambda_K} \tag{4.39}$$

where $\tilde{\boldsymbol{S}}_{\boldsymbol{p},\boldsymbol{K}}$ is a submatrix of $\tilde{\boldsymbol{S}}_{\boldsymbol{p}}$ containing the columns corresponding to the parameters of the subset K, and λ_K the smallest eigenvalue of $\tilde{\boldsymbol{S}}_{\boldsymbol{p},\boldsymbol{K}}^T \tilde{\boldsymbol{S}}_{\boldsymbol{p},\boldsymbol{K}}$. The index γ_K is a measure of the degree of linear dependence of the columns in $\tilde{\boldsymbol{S}}_{\boldsymbol{p},\boldsymbol{K}}$. Basically, a value of λ_K equal to 1 means the orthogonality of the columns of the subset K, while a value approaching the infinity indicates a high linear dependency between them. If the latter case is verified, changes in the simulated outputs due to the small variation of a parameter can be compensated by an appropriate modification of the value of the other parameters in K implying an impossibility to identify each of them using the considered data set. Therefore, an higher λ_K means that the identified parameters by fitting procedure are not reliable because they represent only one of many different possible solutions. Generally, an empirical threshold of 20 for λ_K is considered in many works, as it represents limit over which the effect of collinearity between parameters is significant and the parameter is defined unidentifiable. However, a value approaching as much as possible one represent the best case.

4.3.2   Comparison of parameter identifiability

In the Table 4.3, mean square sensitivities related to the considered parameters and for each FRA transfer function are displayed for all the steady state current density considered. They have been determined from the values of the simulated magnitude Bode plots at different frequencies according to the Equation 4.38. Additionally, the adimensional sensitivites as function of the frequency at the highest current current density are compared in the Figure 4.9.

It is noticeable that all the FRA techniques are highly influenced from the value of the cathode transfer coefficient. The lowest mean square sensitivity value of 0.26 is verified for the voltastatic CFRA by water input. The CFRA techniques under galvanostatic control are the most sensitive to this kinetic parameter. Additionally, the sensitivity does not change considerably along with the steady state current for any of the frequency response methodologies. This behavior is reasonable, since the kinetic activity of the catalyst is not affected by the mass transport which is the main phenomena increasing its impact proportionally with the current. Moreover, unchanged ORR kinetic mechanism has been assumed along the different polarization conditions. The Figure 4.9a shows that the adimensional sensitivity generally increases towards lower frequencies achieving the highest values from 1 Hz on, which is the frequency range of the dynamics of gas transport in the cathode channel.

Current	Technique	$\delta_{\alpha_c}^{msqr}$	$\delta_{\varepsilon_{O_2}}^{msqr}$	$\delta_{\varepsilon_{H_2O}}^{msqr}$	$\delta_{D_{H_2O}^M}^{msqr}$	$\delta_{K_{H+}}^{msqr}$
	EIS	0.41	0.06	0.01	0.01	0.01
	CFRA(O_2) vol.	0.39	1.95	0.01	0.01	0.01
100 mA cm^{-2}	CFRA(O_2) gal.	0.75	1.97	0.01	0.01	0.01
	CFRA(H_2O) vol.	0.27	0.28	0.68	0.34	0.11
	CFRA(H_2O) gal.	0.48	0.29	0.69	0.34	0.15
	EIS	0.39	0.21	0.02	0.01	0.01
	CFRA(O_2) vol.	0.44	1.8	0.01	0.02	0.02
200 mA cm^{-2}	CFRA(O_2) gal.	0.77	1.85	0.005	0.02	0.03
	CFRA(H_2O) vol.	0.33	0.32	0.75	0.32	0.28
	CFRA(H_2O) gal.	0.48	0.37	0.77	0.33	0.27
	EIS	0.49	0.92	0.03	0.04	0.03
	CFRA(O_2) vol.	0.37	1.46	0.01	0.05	0.05
300 mA cm^{-2}	CFRA(O_2) gal.	0.76	1.95	0.01	0.06	0.06
	CFRA(H_2O) vol.	0.36	0.77	0.84	0.42	0.38
	CFRA(H_2O) gal	0.54	1.1	0.87	0.5	0.41

Table 4.3: Mean square sensitivities of the different transfer functions at three steady state currents.

The mean square sensitivity to the effective porosity related to oxygen diffusion presents a general rising trend along the steady state current density for all the FRA techniques except for the CFRAs by oxygen perturbations. For these cases, this value stays constant around 1.8 without changing significantly and represents the highest compared to the other ones. On the contrary, the EIS presents the lowest sensitivity for this parameter. As noticeable in the Figure 4.9, the sensitivity to the effective porosity of the galvanostatic CFRAs dramatically rises up at higher frequencies, while it stabilizes to a plateau at lower ones. Then, it can be concluded that the best part of the spectra to determine the porosity by model fitting could be the frequency region higher than 10 Hz.

The parameters influencing the water transport in the GDL and in the membrane present a low mean square sensitivity for the EIS and the CFRAs by oxygen pressure perturbations. On the contrary, the CFRA transfer functions obtained by water pressure input result to have a high sensitivity to these parameters which increases together with the steady state current density. Then, it can be concluded that the selectivity of these experimental techniques to the phenomena involving water transport implies a higher influence to the related parameters as well. In the Figures 4.9c-e, it can be observed that the adimensional sensitivities of these techniques present a significant value over 0.1 for most of the frequency range considered. This means a reliable parameter estimation regardless from the fitted region of the spectra.

The collinearity index of different sets of the considered parameters relative to EIS and CFRA methodologies at the three different operating conditions are exposed in the
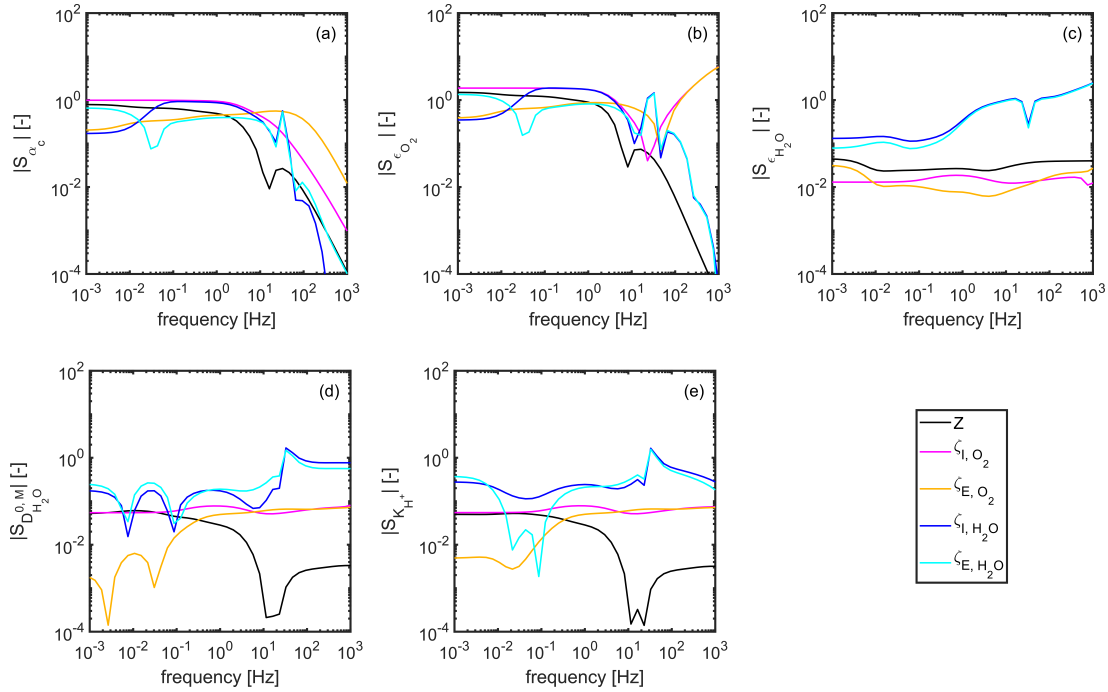
Figure 4.9: Comparison adimensional sensitivities coefficients of the main kinetic and transport parameters: (a) charge transfer coefficient of the ORR, (b) effective porosity related to the oxygen transport, (c) effective porosity related to water transport on the cathode, (d) intrinsic diffusivity coefficient of water in Nafion, (e) electrosmotic flow constant.

Table 4.4. The sets have been chosen with the purpose to quantify the interdependence of parameters influencing phenomena which effect on the response could overlap with each other. Accordingly, in the subsets 1 and 2, it has been respectively determined the collinearity between the kinetic cathode transfer coefficient and the effective diffusivity for the oxygen transport, and between the intrinsic diffusivity of the water in Nafion and the electrosmotic drag constant. In the subsets from 3 to 6, the collinearity index for all the possible combinations of three parameters among the ones considered are displayed. Finally, the subset 7 shows the collinearity index for all the parameters related to mass transport phenomena.

The first apparent observation to point out concerns the correlation index of the subset 1 close to the optimal value of 1 for all the CFRA techniques at all the operating conditions. This means that the kinetic transfer coefficient and the effective porosity related to the oxygen transport are completely independent and their values do not influence each other. Therefore, the estimation of these parameters through model fitting of CFRA spectra in the considered frequency region does not present correlation problems. The same considerations are valid for the transport parameters relative to

63

Current	Subset number	Parameters	EIS	CFRA(O_2) gal.	CFRA(O_2) vol.	CFRA(H_2O) gal.	CFRA(H_2O) vol.
	1	$\alpha_C, \varepsilon_{O_2}$	9.13	1.02	1.04	1.17	1.11
	2	D_λ, ξ_{el}	16.19	7.71	11.69	1.11	1.07
100 mA cm^{-2}	3	$\varepsilon_{O_2}, \varepsilon_{H_2O}, D_\lambda$	7.04	2.04	2.19	4.24	4.12
	4	$\varepsilon_{O_2}, \varepsilon_{H_2O}, \xi_{el}$	10.51	2.12	2.09	1.25	1.16
	5	$\varepsilon_{O_2}, D_\lambda, \xi_{el}$	17.21	9.59	11.69	1.14	1.15
	6	$\varepsilon_{H_2O}, D_\lambda, \xi_{el}$	27.59	128.8	12.55	4.19	4.2
	7	$\varepsilon_{O_2}, \varepsilon_{H_2O}, D_\lambda, \xi_{el}$	30.63	128.8	13.52	4.42	4.32
	1	$\alpha_C, \varepsilon_{O_2}$	10.77	1.11	1.01	1.7	1.48
	2	D_λ, ξ_{el}	8.13	144.36	7.26	1.39	1.84
200 mA cm^{-2}	3	$\varepsilon_{O_2}, \varepsilon_{H_2O}, D_\lambda$	3.29	9.27	1.45	2.21	2.13
	4	$\varepsilon_{O_2}, \varepsilon_{H_2O}, \xi_{el}$	3.23	9.75	1.53	1.13	1.26
	5	$\varepsilon_{O_2}, D_\lambda, \xi_{el}$	8.36	180.7	7.27	1.43	1.9
	6	$\varepsilon_{H_2O}, D_\lambda, \xi_{el}$	8.29	645.58	12.61	4.05	4.39
	7	$\varepsilon_{O_2}, \varepsilon_{H_2O}, D_\lambda, \xi_{el}$	8.48	657.75	13.11	4.49	4.44
	1	$\alpha_C, \varepsilon_{O_2}$	21.75	1.86	2.32	6.45	4.98
	2	D_λ, ξ_{el}	16.99	12371	17.64	3.47	3.75
300 mA cm^{-2}	3	$\varepsilon_{O_2}, \varepsilon_{H_2O}, D_\lambda$	1147	9922	1.7	1.91	1.47
	4	$\varepsilon_{O_2}, \varepsilon_{H_2O}, \xi_{el}$	14.77	24292	1.81	1.64	1.29
	5	$\varepsilon_{O_2}, D_\lambda, \xi_{el}$	18.58	14077	17.83	4.37	3.9
	6	$\varepsilon_{H_2O}, D_\lambda, \xi_{el}$	17.06	18924	23.77	6.14	5.12
	7	$\varepsilon_{O_2}, \varepsilon_{H_2O}, D_\lambda, \xi_{el}$	19.08	37507	24.77	7.03	5.78

Table 4.4: Collinearity index of EIS and CFRA transfer function at three different current densities.

the water in Nafion.

Then, it is remarkable the extremely high values of the correlation index of the galvanostatic CFRA by oxygen input for all the subsets including parameters related to the transport phenomena (subsets 2-7). This extensive overcoming of the fixed threshold means the existence of many different branch of parameters which could fit the experimental data without converging to a single one. For this reason, despite of the high sensitivity to all the fitted parameters, this FRA technique cannot give reliable evaluation of them, by the fitting of a single spectra, giving misleading evaluations on the status of the PEMFC.

On the contrary, CFRAs performed by water present the lowest values of collinearity index relative to the transport parameters displaying a maximum value of 7.03 for the subset 7 which is significantly below the tolerable threshold of 20.

From the analysis of the mean square sensitivity coefficient and correlation index exposed above, the following main considerations can be deduced about the identifiability of parameters and their estimation. First, the CFRA techniques present better performance then classic EIS in parameter identification, as they are generally characterized by higher sensitivities and lower collinearity index. For example, the estimation of the kinetic transfer coefficient and parameters related to transport of oxygen by model fitting is completely free from correlation problems with respect to the EIS which could lead to unreliable results. The same is not verified in all the CFRA about the estimation of the parameters related to transport phenomena. For instance, galvanostatic CFRA by oxygen perturbations results to have correlation index related to the

subsets of transport parameters excessively above the tolerable limit, despite good values of sensitivity. For these reasons, this FRA technique could be not suitable to give information on the mass transport resistances of PEMFCs. On the contrary, CFRAs performed by water perturbations are the only experimental techniques to present high sensitivities and tolerable correlation index between both kinetic and transport parameters (see subset 7). Therefore, it can be concluded that the model fitting of the spectra obtained through these methodologies gives the most reliable results among all the others FRA methodologies analysed. Then, according to the performed identifiability analysis, they are the most suitable to be employed to develope onboard diagnostic tools for PEMFCs.

However, it must be remarked that this analysis is based on an optimal case of wide frequency range of spectra ($0.001 Hz < f < 1000 Hz$) and estimation of the transfer function along 16 points per decade. The identification of parameters based on fitting of experiments with different values of these setting could lead to different conclusions.

4.4 Feasibility analysis

As for all linear FRA techniques, in order to collect reliable data, CFRA experiments must respect conditions of linearity [143, 144, 146]. This mainly implies the application of pressure perturbations with an amplitude sufficiently small to avoid nonlinearities in the electric response of the fuel cell. On the other hand, the amplitude of the pressure should also be large enough to produce an electric response which could be detected and distinguished from the eventual noise. Therefore, the amplitude of a proper input is restricted by the requirement of linearity on one side, and the signal detectability on the other side. Therefore, in the following, detecatability and nonlinearity limitations specific for the considered electric output are defined.

Several methods to quantify the nonlinearities in the output of a frequency response have been proposed [188, 189]. As a most convenient method, in the present case a so-called total harmonic distortion (THD) of a signal has been introduced. This method has been successfully applied in the past [190, 191] for such purposes. Given a periodic signal W composed by different harmonics of amplitude Δ_i, the THD is defined as

$$THD = 100 \sqrt{\frac{\Delta_1^2 + \Delta_2^2 + ...}{\Delta_1}}. \tag{4.40}$$

As suggested in different works [190, 191], for sinusoidal inputs, the THD value should not exceed the value of 5. Over this value, the contents of nonlinearities of the response is supposed to be too high to perform a data analysis conform with the LST assumptions.

The detectability limit is restricted by the amplitude of the electric response. The minimum value of the amplitude which can be clearly detected is fixed at 5 mA and

5 mV, respectively for the voltastatic, and galvanostatic operating control. These detectability limits are largely overestimated, since the modern potentiostats have a resolution 0.3 μV for the voltage. However, an excess in the approximation of this quantity is reasonable for a theoretical study and also considering the possible presence of noise sources.

To theoretically verify the respectability of the CFRA technique to the imposed limitations, the model has been numerically solved to simulate the electric response of the cell to sinusoidal oxygen pressure perturbations at different frequencies, and with amplitudes of different magnitudes. For each output, the amplitude and the THD have been collected. By treating these data, the operating windows in Figure 4.10, for voltastatic and galvanostatic control, have been designed. Each point of the diagram is related to an input specification, i.e. an amplitude of oxygen pressure and a frequency which characterizes a perturbation. The green line indicates the detectability limit. The inputs characterized by the specification points below this line do not generate a detectable electric response. Likewise, the inputs with the specifications indicated by the points over the nonlinearity limit (red line) produce an output containing a not tolerable quantity of nonlinearities. Therefore, the white region represents the operating window for the CFRA which satisfies the feasibility requirements. It is noticeable that the voltastatic CFRA presents a wider feasible operating window than the galvanostatic one. However, in both the cases, oxygen pressure perturbations enabling to produce linear and detectable responses are possible. However, this analysis does not consider technical limitation related to the production of pressure perturbations at such high frequencies which could limit the available frequency range for practical experiments. This aspect is evaluated and discussed in the next chapter.

4.5   Conclusions

The capability of CFRA as experimental technique for diagnosis and study of the dynamics of a PEMFCs has been theoretically investigated through development of a 1-D dynamic model. Oxygen and water pressure perturbations sent to the cathode side of the cell have been chosen as inputs. As output, voltage and current responses have been obtained depending on the electric control applied to the cell, i.e. galvanostatic or voltastatic, so that 4 different CFRA transfer functions could be determined. It has been shown that CFRA spectra can discriminate different dynamic processes occurring in the cell, depending on the kind of concentration perturbation, and electric control applied. For example, the galvanostatic CFRA by oxygen perturbations can selectively detect the dynamics related to the transport of gas in the channel. On the other hand, the comparison between the CFRA spectra obtained by oxygen perturbations under voltastatic and galvanostatic controls, can be used to identify the contribution of the transport of water in the membrane to the system dynamics. Moreover, this phenomena can be selectively studied through CFRA transfer functions based on water pressure perturbation.
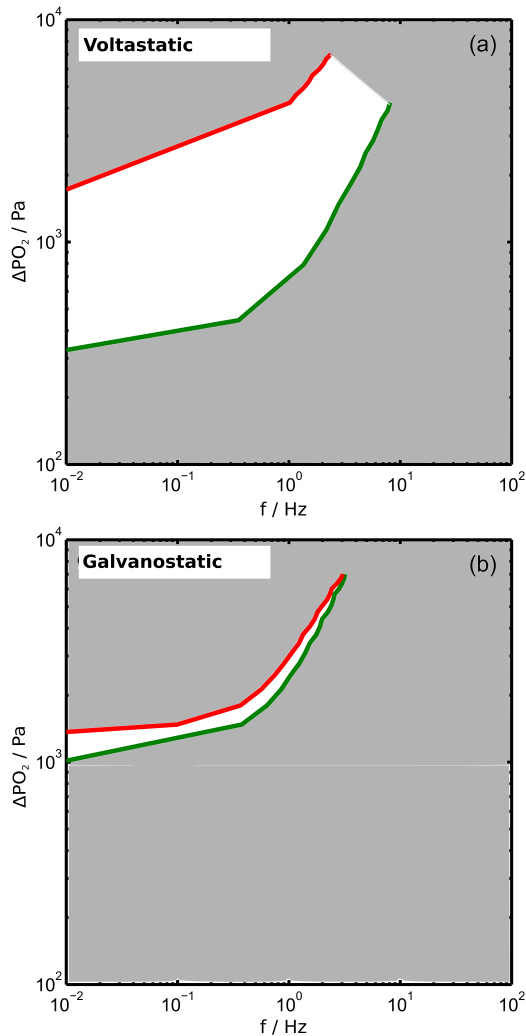
Figure 4.10: Operating window for CFRA experiments involving oxygen perturbation under voltastatic (a), and galvanostatic (b) control. Operating current: 300 mA cm^{-2}.

The results of the identifiability analysis attests that the use of partial pressure perturbations could allow a more correct estimation of the kinetic and transport parameters, compared to the classic EIS. In this regard, the CFRAs performed by using water pressure inputs presented the best performance representing the most promising diagnostic tools for onboard applications among the others. Additionally, the feasibility analysis demonstrates that CFRA experiments for PEMFC could be performed respecting the linearity and detectability constraints.

Chapter 5

Experimental setup and data analysis procedure

In order to validate the theoretical findings discussed in the Chapter 4, a special setup capable to produce a feed with a periodic pressure of oxygen and water at different frequencies was constructed. In the Section 5.1, the technical functionalities of the setup, its limitations as well as the characteristics of the used fuel cell hardware are discussed in detail. Then, the spectral analysis applied to the pressure inputs and electrical outputs to obtain the CFRA transfer functions from the measured quantities is explained in the Section 5.2. Finally, the complete experimental protocol developed to determine the CFRA spectra is described.

5.1   Experimental setup

5.1.1   General description

A scheme of the cathode feed conditioning section of the setup designed to perform CFRA experiments is displayed in the Figure 5.1. The initial part is similar to standard facilities used to characterize PEMFCs performance. The various parts of the experimental setup are numbered in the following description as indicated in the scheme. Dry streams of pure oxygen (1) and nitrogen (2) (99.999% purity) dispensed by Air Liquide were supplied to the system using Bronkhorst EL Flow mass flow controller to dose them in the desired proportions and quantities. The mixture of gases was humidified through a bubbler (4) covered by an external jacket in which heated water was circulating. A Julabo F32 heating circulator (6) was used to heat and pump the water to the jacket controlling indirectly the temperature of the water in the bubbler. In this way, a humidified stream at a fixed dew point temperature was obtained as outcome. In order to avoid water condensation, the temperature of the tubes was kept at least 10 C° degrees more than the fixed dew point temperature by using heating tapes provided of Pt100 temperature sensors and PID controllers. A Vaisala DMT340 dew point meter
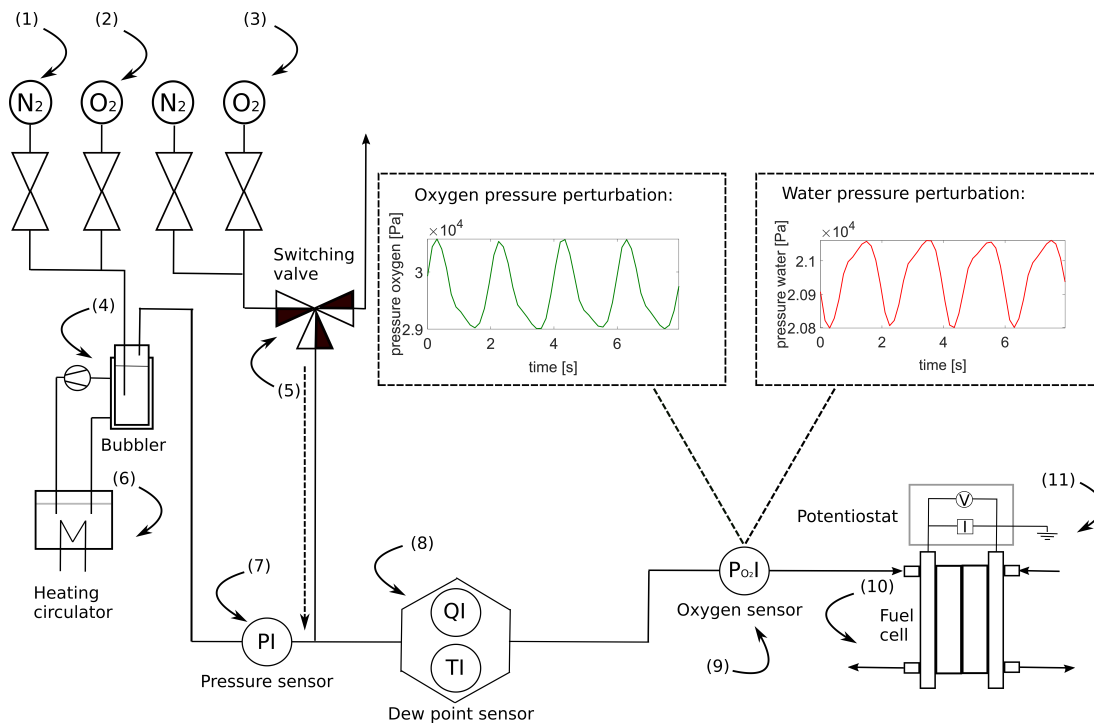
Figure 5.1: Schematic of the cathode feed conditioning section of the experimental setup. Periodic pressure input signal (oxygen and water) and electric output under galvanostatic control of the cell (voltage) at two different frequencies are shown in the inset.

(8) measured the humidification level and the temperature of the gas stream, while a sensor by Elettrotechnik Gmbh (9) monitored the total pressure at the inlet.

The oxygen and water perturbations were produced adding periodically a flow of dry oxygen or nitrogen (3) to the main humidified stream through the use of a switching valve (5) capable to regularly alternate the direction of the additional flow to the cell or to the outlet. The frequencies of the periodic pressure perturbations so obtained were regulated by setting different switching times of the valve between the two flow directions. The set value of the added flow rate was changed in the range of 3-6 % of the main cell feed in order to assure the linearity of the electric response. The protocol developed to verify the condition of linearity is discussed in the Chapter 6.

The addition of a dry stream of pure oxygen or nitrogen simultaneously changes the partial pressure of oxygen and water in the main inlet feed (see insets in the Figure 5.1). The variations of oxygen were measured by a OXR430-UHS oxygen fiber sensor (9) produced by Pyro Science Gmbh which was collocated at the center of the tube before the cathode entrance. The measuring principle of this sensor is based on near-infrared emissions of a photosensitive dye (the indicator) immersed in a polymer matrix caused by its excitation through a modulated red light radiation coming from a photo-diode. The intensity of the light emitted by the indicator is dependent on the pressure of

oxygen surrounding it. The sensor is characterized by a fast time response τ_{90} of 200 ms and a sampling frequency f_s about 6.6 Hz. The used dew point meter (8) to measure the water pressure variations is characterized by a time response of 10 seconds which allows to detect only periodic water perturbations with frequencies lower than 0.1 Hz. For this reason, a calibration procedure of the fiber sensor enabling to extract the water partial pressure variations from the oxygen measurements was established. The procedure is described in detail in the next section.

The features of the produced oxygen and water periodic perturbations and related electric responses depend on the composition of the additional flow used and their frequency. In the Figure 5.2, profiles of pressure inputs and voltage output obtained by adding additional flow of pure oxygen under galvanostatic control are displayed at two different frequencies. It is remarkable that the perturbation produced at the higher frequency of 500 mHz (Figures 5.2a, c) replicates the shape of a sinusoidal, while it turns in a square wave going towards lower frequencies (Figures 5.2b, d). Moreover, the oxygen and water perturbations are out of phase to each other. Then, an increment of the oxygen in the stream is followed by a simultaneous decrease of the water partial pressure and vice versa. This is due to fact that the addition of a dry flow of oxygen increases the oxygen partial pressure in the main stream, but on the other side, it leads to a decrease of the one of the water. The effect of this out of phase coupling of the inputs is well observed in the voltage response at the lower frequency (Figure 5.2f), where a fast increase is first detected as result of the rise of oxygen pressure. Then, a slow decrease of the voltage is verified probably due the lowering membrane hydration consequent to the decreasing water partial pressure. Contrary behaviour is seen when periodically the additional flow of oxygen is not supplied and a quick decrease of voltage followed by a slow increment is observed.

The inputs and output profiles produced using periodic addition of nitrogen are displayed in the Figure 5.3. In this case, the two pressure perturbations are in phase with respect to each other, as the periodic addition and subtraction of an additional flow of nitrogen to the cell feed respectively causes a simultaneous increase and decrease of both oxygen and water partial pressure (Figures 5.3a-d). Dislike the previous case, the voltage response, after the initial fast increase along with the higher oxygen partial pressure, continues to rise as result of the concurrent increase of water pressure which improves the membrane hydration (Figure 5.3f). On the other hand, the periodic lowering of the partial pressure of both the components leads to a sharp decrease of the voltage followed by a slower one.

5.1.2   Fuel cell hardware

All the experiments shown in this work were performed using a single PEMFC having an active area of 25.8 cm^2 and flow fields with parallel channel configuration. Two type of membrane electrode assembly (MEA) were used. One was prepared in-house following the same procedure described in the reference [192] using Nafion 117 membrane and catalyst ink consisting of platinum black (Alpha Aesar). The other one pro-
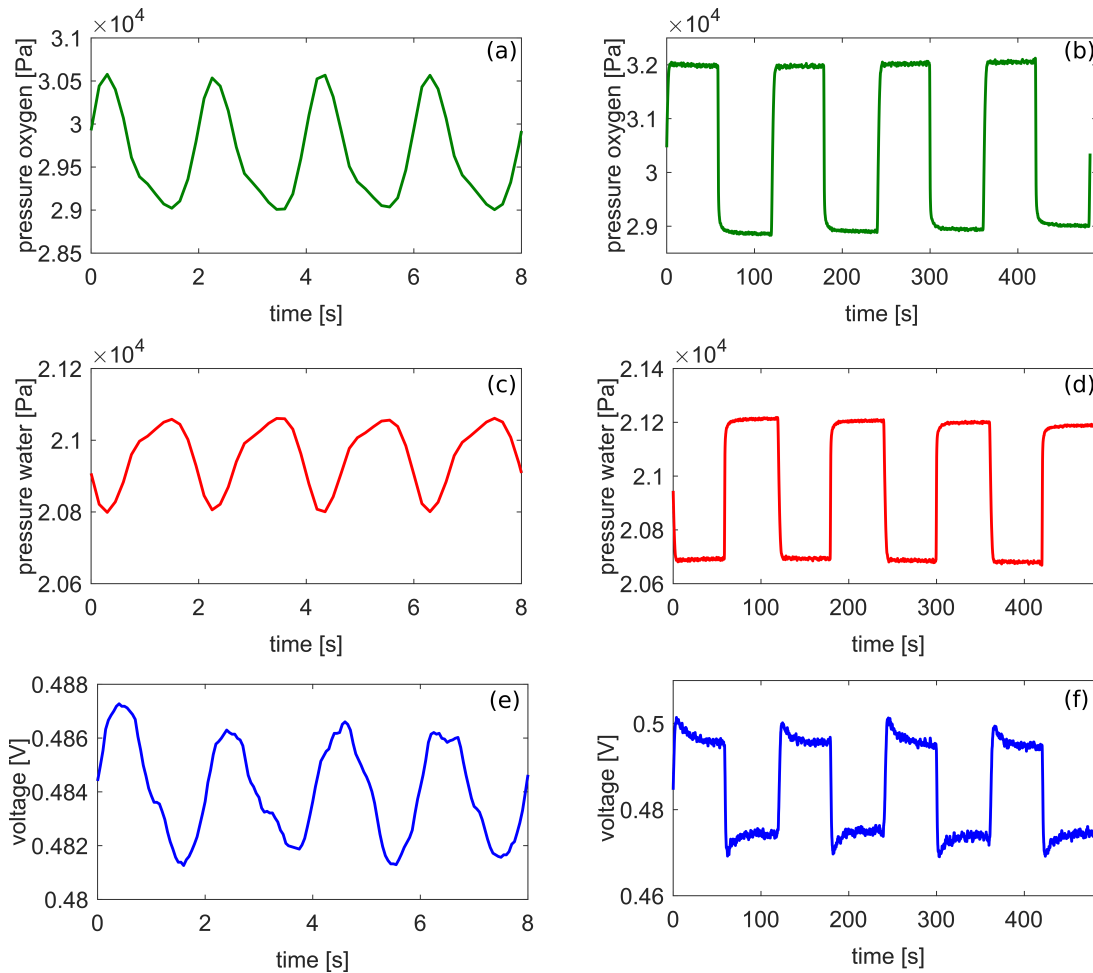
Figure 5.2: Pressure input and voltage output profiles obtained by using periodic addition of oxygen flow at different frequencies: (a) periodic oxygen pressure input at 500 mHz, (b) periodic oxygen pressure input at 8 mHz, (c) periodic water pressure input at 500 mHz, (d) periodic water pressure input at 8 mHz, (e) periodic voltage output at 500 mHz, (f) periodic voltage output at 8 mHz

vided by Quintech which was based on advanced surface area carbon on Nafion 115. In both cases, the platinum loading on cathode and anode side was 1 mg/cm^2. Toray paper TGP-H-060 was used as GDL. The temperature of the fuel cell was controlled by a heating box equipped with a PID controller. An Autolab potentiostat PGSTAT302 (10) with FRA unit and a BOOSTER20A was used to control and monitor the fuel cell voltage and current during the measurements.
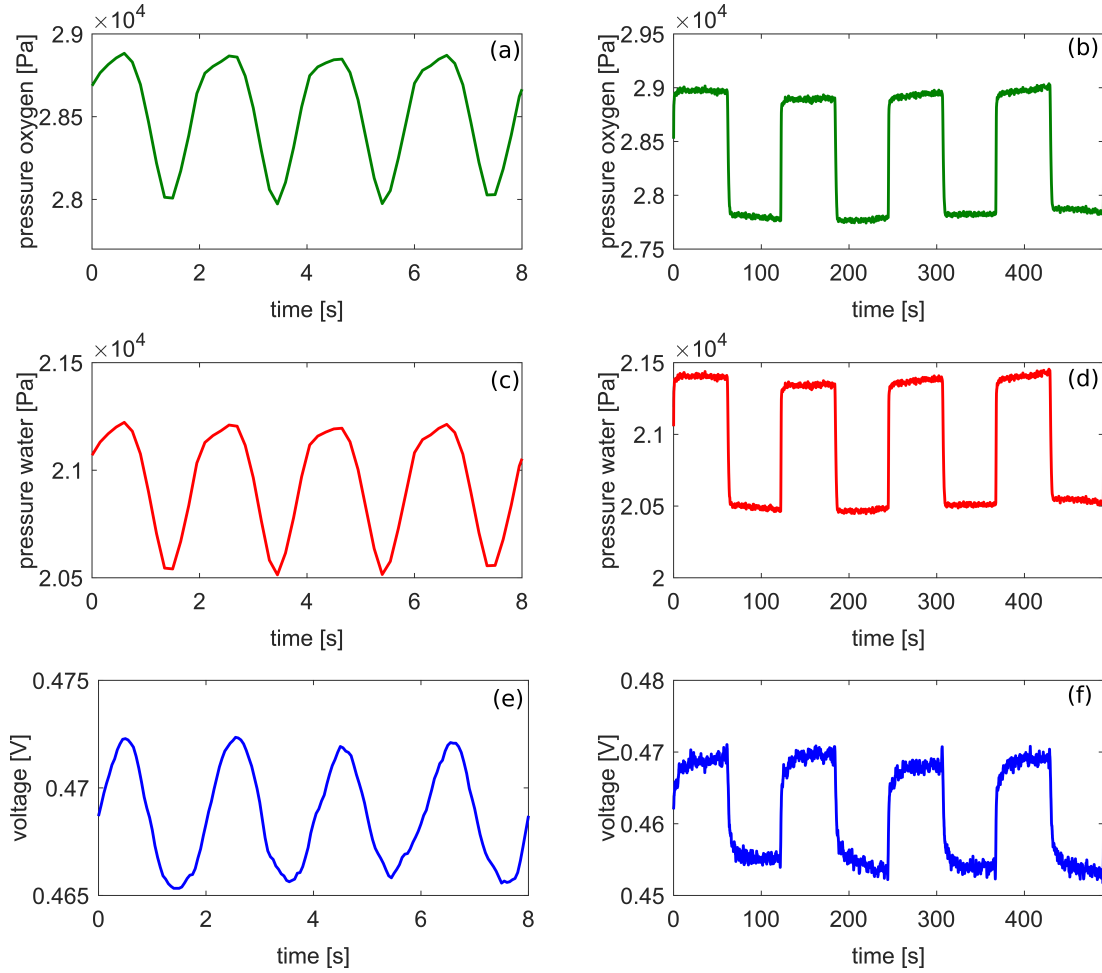
Figure 5.3: Pressure input and voltage output profiles obtained by using periodic addition of nitrogen flow at different frequencies: (a) periodic oxygen pressure input at 500 mHz, (b) periodic oxygen pressure input at 8 mHz, (c) periodic water pressure at 500 mHz, (d) periodic water pressure input at 8 mHz, (e) periodic voltage output at 500 mHz, (f) periodic voltage output at 8 mHz

5.1.3 Calibration of the oxygen fiber sensor for faster measuring of water pressure perturbations

A schematic of the calibration procedure is depicted in the Figure 5.4a. First, a humidified flow F_{in} corresponding to the main feed characterized by an initial pressure of oxygen $P_{O_2,0}$ and water $P_{H_2O,0}$ was sent to the cathode inlet. Then, the additional flow rate of oxygen was step-wise increased until a certain value $\Delta F_{O_2,n} = n\Delta F_{O_2,0}$, where n and $\Delta F_{O_2,0}$ are respectively the total number of the applied steps and the step increment of the flow rate. For each step, the variation of the pressure of water and oxygen was registered after a time sufficient to the slower dew point meter to stabilize its value (see Figure 5.4a). In this way, a series of corresponding n partial pressure data
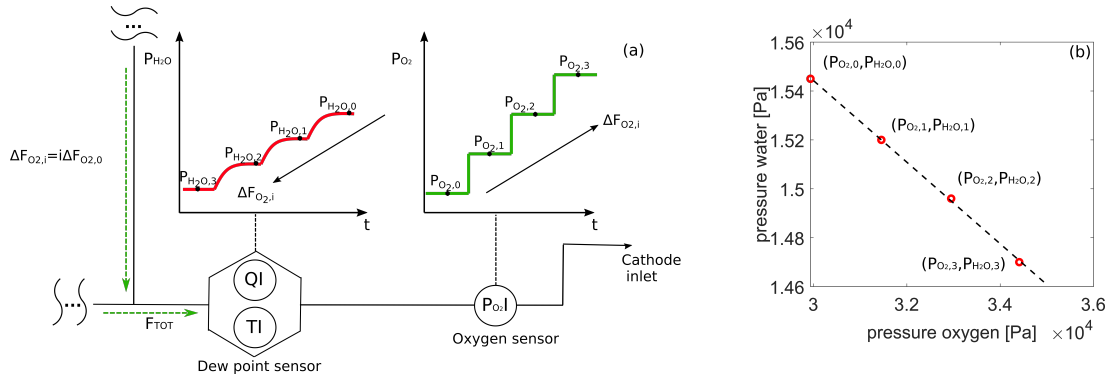
Figure 5.4: Schematic of the calibration of the oxygen fiber sensor for the indirect measurements of the water pressure: (a) detailed scheme of the cathode inlet and applied partial pressure steps, (b) calibration line displaying the dependence of water pressure over oxygen pressure.

$(P_{O_2,i}, P_{H_2O,i})$ were collected which can be fitted to obtain a linear relation expressing the dependence between the oxygen pressure variation measured by the sensor and the pressure of water (Figure 5.4b). Then, the obtained equation could be simply applied to extract the pressure of water from the measured oxygen pressure during the CFRA experiments. In this way, the limitation to the measurements of fast variations of water pressure due to the slow response time of the dew point meter could be overcame. The value of $\Delta F_{O_2,n}$ was kept below or equal to the additional flow rate used in the performed CFRA in order to assure the validity of the calibration line during the experiments.

The calibration procedure was repeated adding the additional flow rate of nitrogen as well. In the example depicted in the Figure 5.4, the step-wise increment of oxygen cause a decrease of the partial pressure of water and, for this reason, a descending calibration line is obtained. The situation is reversed in the calibration of the sensor related to the addition of nitrogen which is here not depicted. A decrease of both the partial pressures is verified along with the the nitrogen flow steps, and a calibration line increasing together with the oxygen pressure is obtained. The operation of the calibration of the sensor was repeated any time the feature of the main stream changes (total flow rate, dew point temperature, ratio between oxygen and nitrogen etc.).

However, some phenomena which could limit the validity of the calibration line for periodic pressure perturbations at high frequencies must be considered and evaluated. For fast periodic additions of flows, the partial pressure perturbations are comparable to the ones obtained by adding concentration pulses of a certain component. Under these circumstances, a significant backward and forward diffusion of the chemical species of the gas mixture occurs. This phenomenon is well known with the name of Taylor diffusion. As the extent of the effect of it mainly depends on the molecular diffusivity, it influences the distribution of the components of the gas mixture along the space in a different way for each one. For these reasons, the ratio between the pressures of water

and oxygen could be slightly different from the one in equilibrium conditions at which the calibration line has been determined

The effect of the dispersion can be expressed for a component α by the adimensional dispersion coefficient defined as the ratio between the pressure at the point of the tube where the additional flow is added P_α^0 and the one at the cell inlet P_α^L. The mathematical expression of this value reads:

$$\phi_\alpha = \frac{P_\alpha^L}{P_\alpha^0} = \frac{F_{tot}}{\pi^{3/2} r^2 \sqrt{\frac{D_{\alpha,air} L_{setup}}{\bar{u}}}} \tag{5.1}$$

where r is the radius of the tube, $\bar{u}$ the average velocity of the gas and L_{setup} the distance between the point where the additional flow is added to the main stream and the cell inlet. The ratio between the values of ϕ_α of two components can be considered as a parameter to compare the effect of the dispersion between them. In this regard, a ratio of the dispersion coefficients close to 1 implies that the the ratio of the partial pressures of the two components in transient regimes is equal to the one at steady conditions. At the usual operating conditions employed in this work, the ratio of the values of ϕ_α of the water and oxygen is 0.9 implying an almost complementary dispersion. This result was expected, since the values of the diffusivity of oxygen and water in air is comparable (check Table 4.1). For this reason, the effect of the Taylor diffusion is considered tolerable and the estimation of the water pressure using the calibration line valid for periodic input at high frequencies as well.

It must be remarked that the effect of the Taylor diffusion involves periodic input characterized by a frequency at least higher than 120 mHz. At lower frequencies, the perturbations achieve a stable value assuming the square wave shape seen in the previous section. Additionally, the influence of the effect of the dispersion quantified in the Equation 5.1 could be overestimated, as it is based on the ideal case of concentration pulse occurring at an infinitesimal range of time. The values used in the equation 5.1 and their reference are listed in the Table 5.1.

Quantity	Value	Dimension
L_{setup}	1	m
r	1.225×10^{-3}	m
t^*	0.71	s
$\bar{u}$	1.4	m s^{-1}

Table 5.1: Parameters related to fluid dynamics and geometry of the setup.

5.1.4 Limitations of the setup

The wide frequency band considered in the theoretical studies of the CFRA discussed in the Chapter 4 is practically not accessible using the developed setup. Basically, the

74

highest frequency limit achievable is determined by the features of two devices: (i) the fiber oxygen sensor which limits the measurability of the periodic input up to a certain frequency, (ii) the switching valve which determines the maximum frequency of the periodic pressure input that can be produced.

The technical features determining the capability of the optical fiber sensor to detect fast changes of the oxygen partial pressure are the time response and the sampling frequency. According to the provider (PyroScience Gmbh), the time response of the used sensor τ_{90} is around 200 ms meaning that only the 90% of the actual value of the amplitude of a periodic input with a frequency of 2.5 Hz is detected. However, the effect of this delay can be compensated to evaluate correctly the measured signal if the exact value of τ_{90} is determined and the dynamic behaviour of the sensor is known. On the other hand, the maximum sampling frequency of the sensor is 7 Hz. According to the Nyquist-Shannon sampling theorem, this implies that a periodic signal with a frequency up to 3.5 Hz can be meaningfully detected.

The limitation of the switching valve is related to the maximum switching rate of 0.5 s which makes possible to produce a periodic partial pressure perturbation up to 1 Hz.

Among all the technical features mentioned, the one presenting the lowest frequency limit is the switching rate of the switching valve. Thus, it determines the highest frequency achievable by the experiments. Therefore, all the CFRA spectra experimentally measured in this work are determined for a frequency range approximately up to 1 Hz. In the Figure 5.5, a sketch of the the inaccessible frequency range in the CFRA Bode plots represented by the grey area is displayed. As one can see, the dynamics detected are not excluded by this restriction.

5.2 Data analysis procedure and determination of CFRA spectra

5.2.1 LST description of the setup

In the model based study, the model could be excited by a single sinusoidal pressure input for each frequency. On the contrary, the setup simultaneously applies to the fuel cell both oxygen and water perturbations which are characterized by a square wave shape at lower frequencies. Therefore, different operations and data treatment must be performed in order to determine CFRA transfer functions experimentally.

From the LST point of view, the setup constitutes a multiple input single output (MISO) system, as it implies two perturbations applied at the same time and a single response. A block diagram of the MISO system related to the setup in terms of FRA transfer functions is pictured in the Figure 5.6. The terms $\tilde{P}_{O_2}(i\omega)$ and $\tilde{P}_{H_2O}(i\omega)$ are the actual pressure perturbations in frequency domain, while $\tilde{P}_{m,O_2}(i\omega)$ and $\tilde{P}_{m,H_2O}(i\omega)$ are their respective values measured by the fiber sensor which dynamic behaviour is contained in the transfer function $S(i\omega)$. The mathematical ex-
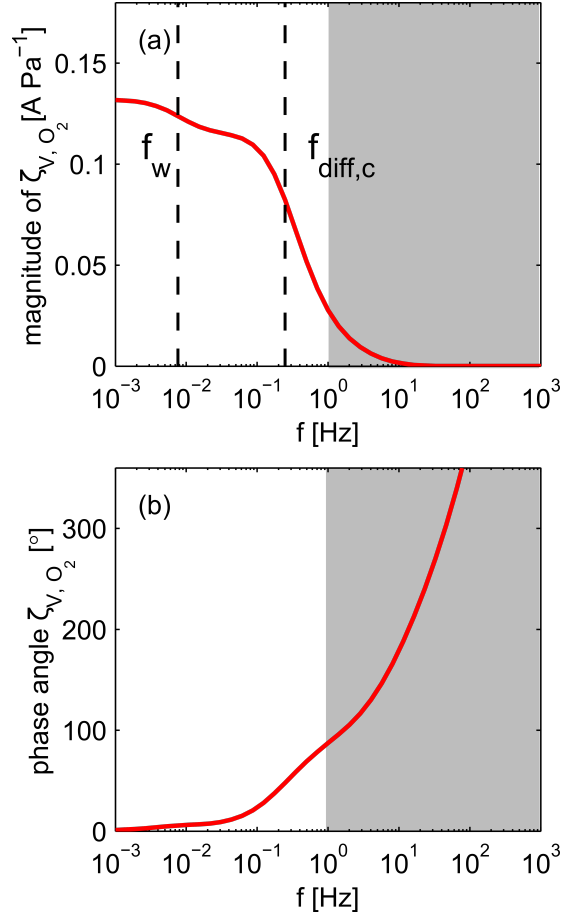
Figure 5.5: Representation of the inaccessible frequency range (grey area) in the CFRA experiments.

pression of this transfer function was determined by fitting the response of the sensor to partial pressure step experiments performed using the setup and considering the device as a second order dynamic system. The procedure is described in detail in the Section 5.2.2. In this way, the effect of the delay of the response of the sensor can be compensated giving the correct value also at higher frequencies. The product between the partial pressure inputs and the generic CFRA transfer functions $\zeta_{O_2}(i\omega)$ and $\zeta_{H_2O}(\omega)$ are added up giving the electric response in frequency domain, i.e. current $\tilde{I}(i\omega)$ or voltage $\tilde{E}(i\omega)$. For a generic electrical output Y_{el}, according to the MISO scheme, this relation reads:

$$\tilde{Y}_{el}(i\omega) = \tilde{P}_{O_2}(i\omega)\,\zeta_{Y_{el},O_2}(i\omega) + \tilde{P}_{H_2O}(i\omega)\,\zeta_{Y_{el},H_2O}(i\omega) = \tag{5.2}$$

$$= \tilde{P}_{m,O_2}(i\omega)\,S(i\omega)\,\zeta_{Y_{el},O_2}(i\omega) + \tilde{P}_{m,H_2O}(i\omega)\,S(i\omega)\,\zeta_{Y_{el},H_2O}(i\omega) \tag{5.3}$$

In the Equation 5.3, the transfer functions $\zeta_{Y_{el},O_2}(i\omega)$ and $\zeta_{Y_{el},H_2O}(i\omega)$ represent the unknown terms, while the variables $\tilde{P}_{O_2}(i\omega)$, $\tilde{P}_{H_2O}(i\omega)$ and $\tilde{Y}_{el}(i\omega)$ can be determined through measurements. Therefore, for each frequency, two sets of measured
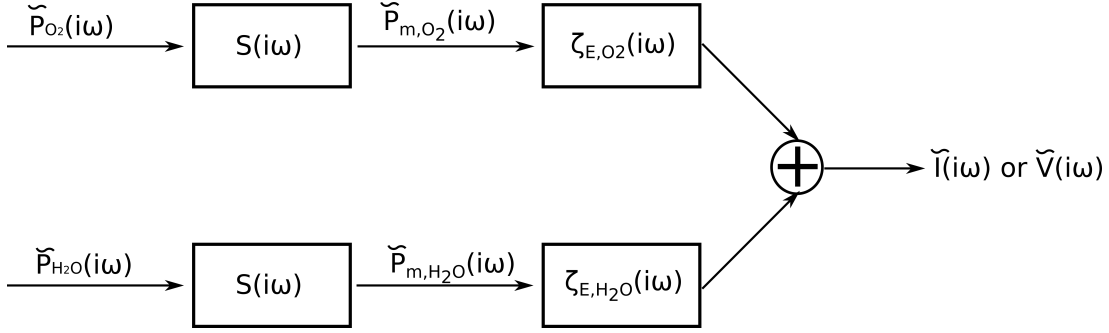
Figure 5.6: Block diagram of the of the MISO system related to the CFRA experiments using the developed setup.

inputs and outputs are required to assess the related CFRA transfer functions. In this way, the following system of two equations is obtained:

$$\tilde{Y}'_{el}(i\omega) = \tilde{P}'_{O_2}(i\omega)\,\zeta_{Y_{el},O_2}(i\omega) + \tilde{P}'_{H_2O}(i\omega)\,\zeta_{Y_{el},H_2O}(i\omega) \tag{5.4}$$

$$\tilde{Y}''_{el}(i\omega) = \tilde{P}''_{O_2}(i\omega)\,\zeta_{Y_{el},O_2}(i\omega) + \tilde{P}''_{H_2O}(i\omega)\,\zeta_{Y_{el},H_2O}(i\omega) \tag{5.5}$$

where the single and the double quote marks respectively stand for the first and the second set of measured values. In order to be the system solvable, the Equations 5.4 and 5.5 have to be linear independent. If this is verified, the CFRA transfer function are obtained by the following soulutions of the system:

$$\zeta_{Y_{el},O_2}(i\omega) = \frac{\tilde{P}''_{H_2O}(i\omega)\,\tilde{Y}'_{el}(i\omega) - \tilde{P}'_{H_2O}(i\omega)\,\tilde{Y}''_{el}(i\omega)}{\tilde{P}'_{O_2}(i\omega)\,\tilde{P}''_{H_2O}(i\omega) - \tilde{P}'_{H_2O}(i\omega)\,\tilde{P}''_{O_2}(i\omega)} \tag{5.6}$$

$$\zeta_{Y_{el},H_2O}(i\omega) = \frac{\tilde{P}''_{O_2}(i\omega)\,\tilde{Y}'_{el}(i\omega) - \tilde{P}'_{O_2}(i\omega)\,\tilde{Y}''_{el}(i\omega)}{\tilde{P}'_{O_2}(i\omega)\,\tilde{P}''_{H_2O}(i\omega) - \tilde{P}'_{H_2O}(i\omega)\,\tilde{P}''_{O_2}(i\omega)} \tag{5.7}$$

The two set of input and output variables were obtained perturbing the cell first by adding periodically additional flow of oxygen to the main feed, and then repeating the same experimental steps by adding nitrogen. As seen in the section 5.1, the two perturbation are out of the phase. For this reason, the linear independence required for the solution of the equations 5.6 and 5.7 is ensured.

5.2.2 Evaluation of the setup and sensor contributions to the CFRA transfer function

The applications of the partial pressure perturbations to the cell can indirectly induce the change of other operating conditions or influence the functioning of some units of the setup. Additionally, the delay of the oxygen fiber sensor in the detection of fast pressure changes leads to an underestimation of the actual extent of the periodic

perturbation at high frequencies. The contributions of these two effects on the measurements were evaluated and subtracted in order to obtain CFRA transfer functions containing the correct response of the fuel cell exsclusively due to the partial pressure inputs.

The addition of the flow of a gas in another stream can cause fluctuations of the total pressure and the temperature. In order to detect these effects, these two parameters were monitored during the CFRA experiments through the related sensors at the cathode inlet (see Figure 5.1). A maximum periodic variation of 30 Pa was measured for the total pressure. This value can be considered negligible compared to the maximum amplitude of the oxygen pressure perturbation of 750 Pa. However, in order to verify the influence of this change on the electric response of the cell, experiments involving variations of the flow rate of the feed with constant the composition and the relative humidity were performed. Specifically, the flow rate of the cell feed was increased of the same increment of the additional flow rate applied during the CFRA to obtain equivalent total pressure variations and the response of the cell was monitored. No significant fluctuations from the steady state value were observed. Therefore, it could be concluded that the total pressure changes were not influencing the determination of the CFRA transfer functions.

On the other hand, no temperature variations were observed during the applications of the partial pressure perturbations. This is probably due to the fact that all the tubes of the setup are heated up approximately to achieve the same temperature and the distance covered by the gases in the pipeline between the addition of the additional flow and the fuel cell inlet (about 1 meter) is enough to uniform the temperature.

As already discussed in the Section 5.2, the effect of the delay due to the time response of the sensor was compensated through the determination of the transfer function $\tilde{S}(i\omega)$ accounted in the Equation 5.3. To achieve this purpose, a model describing the physical principles by which the fiber sensor measures the oxygen variations was developed. Two dynamics acting in series determine the speed of the oxygen detection [193]: (i) the diffusion of the oxygen in the polymer matrix in which the REDFLASH indicator is immersed; (ii) the quenching of the fluorescence of the RED-FLASH indicator which the kinetics is usually described by the Stern-Volmer relationship. This concatenation of processes constituting an overall SISO system can be represented by the transfer function block diagram depicted in the Figure 5.7. For enough small oxygen pressure perturbations, the linear response of such a system can be described by the transfer function relative to a second order model which reads:

$$S(i\omega) = \frac{1}{(1 + i\omega\tau_{s,diff})(1 + i\omega\tau_{s,kin})}. \tag{5.8}$$

In the Equation 5.8, $\tau_{s,diff}$ and $\tau_{s,kin}$ are respectively the time constant of the diffusion and kinetic processes mentioned above. These parameters which characterize the time delay of the sensor were obtained by fitting the corresponding expression of the transfer function in time domain $s(t)$ to oxygen pressure step experiments. Specifically, considering an initial pressure $P_{O_2,in}$ and a step-wise increase of pressure to $P_{O_2,fin}$,

78

$$\tilde{P}_{O_2}(i\omega) \xrightarrow{\hspace{2cm}} \boxed{S_{diff}(i\omega)} \xrightarrow{\hspace{2cm}} \boxed{S_{kin}(i\omega)} \xrightarrow{\tilde{P}_{m,O_2}(i\omega)}$$
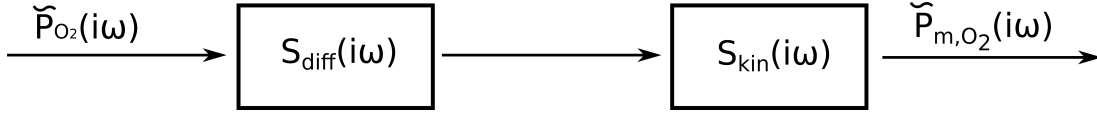
Figure 5.7: Block diagram of the SISO system describing the dynamic process occurring in the oxygen fiber sensor.

the response is equal to:

$$s(t) = P_{O_2,in} + (P_{O_2,fin} - P_{O_2,in})$$
$$\left(1 - \frac{\left(\tau_{s,diff}exp\left(-\frac{t}{\tau_{s,diff}}\right) - \tau_{s,kin}exp\left(-\frac{t}{\tau_{s,kin}}\right)\right)}{\tau_{s,diff} - \tau_{s,kin}}\right) \tag{5.9}$$

The step experiments were performed by adding an additional flow of oxygen to the main stream using the switching valve. Because of the Taylor diffusion, the obtained pressure profile is characterized by a sigmoidal shape. However, the length of the transition region L_{step} where the value of the oxygen pressure changes from $1.1 \cdot P_{O_2,in}$ to $0.9 \cdot P_{O_2,fin}$ in laminar conditions can be estimated by the following equation:

$$L_{step} = 3.62 \cdot \sqrt{\frac{r^2 \bar{u}}{192 D_{O_2,air}} \cdot t_{step}} \tag{5.10}$$

Putting the parameters related to our setup (Table 5.1) in the Equation 5.10, it was estimated a value of 0.11 m for L_{step}. Given the value of the average gas velocity inside the tube, the time t_{step} in which the step transition occurs at the cell inlet is 0.08s. As this value is lower than the sampling time of the oxygen fiber sensor (0.15s), the variation of the oxygen can be approximated to a step function.

In the Figure 5.8, the results related to the estimation of $\tilde{S}(i\omega)$ are displayed. Specifically, the fitting of the oxygen pressure step is shown in the Figure 5.8a, while the obtained $\tilde{S}(i\omega)$ in frequency domain is depicted in the Figure 5.8. A value of 210 ms was estimated for both $\tau_{s,diff}$ and $\tau_{s,kin}$ which is close to the value indicated in the technical specifications by the provider Pyro Science Gmbh (<300ms). It is remarkable that the effect of the delay affect periodic signals higher than 0.1 Hz.

5.2.3 Spectral analysis of the input and output signals

The input and output signals $\tilde{P}_{O_2}(i\omega)$, $\tilde{P}_{H_2O}(i\omega)$, $\tilde{I}(i\omega)$ and $\tilde{V}(i\omega)$ in frequency domain were obtained by applying a build MATLAB® function performing discrete Fourier transformation on the respective signals collected in time domain. In the Figure 5.9, the Fourier amplitude spectra of the signals depicted in the Figure 5.3 are displayed in the same order. The spectra of the periodic signals at higher frequencies (Figure 5.9a, c, e) are similar to the one of a pure sinusoidal with a dominant harmonic
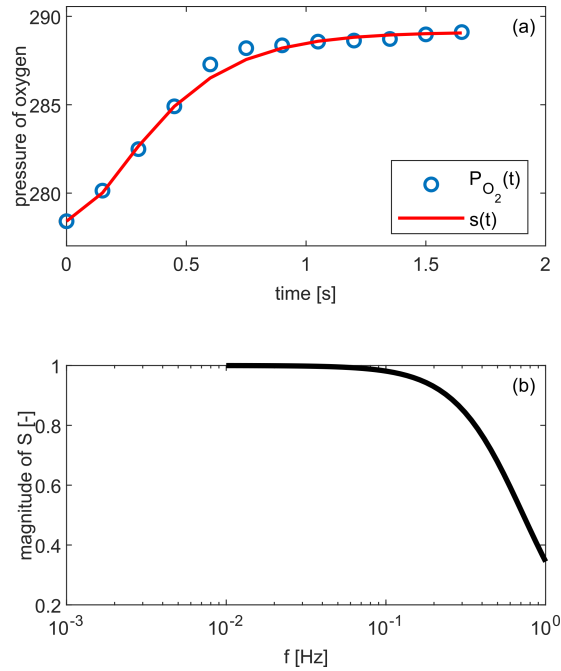
Figure 5.8: Diagrams related to the estimation of the transfer function of the oxygen fiber sensor S: (a) fitting of the oxygen pressure step experiment, (b) transfer function of the oxygen fiber sensor in frequency domain.

at the main frequency of the periodic signal. A smaller peak at a frequency which is the double of the main one indicates a small deviation from a pure sinusoidal shape. As expected, the spectra of the signals with a lower periodic frequency (Figure 5.9b, d, f) reflect perfectly the ones of a periodic square wave, presenting descending harmonic components at multiple odd integer frequencies with respect to the one at the lowest frequency with the highest amplitude. The latter is named fundamental harmonic of the signal.

To determine the values of the pressure inputs and electrical outputs in frequency domain used in the Equations 5.6 and 5.7, only the fundamental harmonics detected in the Fourier spectra were registered ignoring the other ones. The harmonics with lower amplitudes located at higher frequencies were characterized by a lower signal to noise ratio which could lead to highly scattered measurements. The effect of the noise can be further decreased by measuring the signals for longer time. However, a trade-off between the accuracy and measurement time must be defined for each signal depending on the frequency. In this work, the periodic signals with a frequency up to 0.1 Hz were collected for 60 seconds. On the other hand, 4 cycles at least of the ones at lower frequencies were registered.

Moreover, prior to the spectra analysis, a procedure of windowing was applied to the signal in time domain to cut some initial and final measured points in order to select an integer number of periods to analyse. In case of Fourier transform analysis
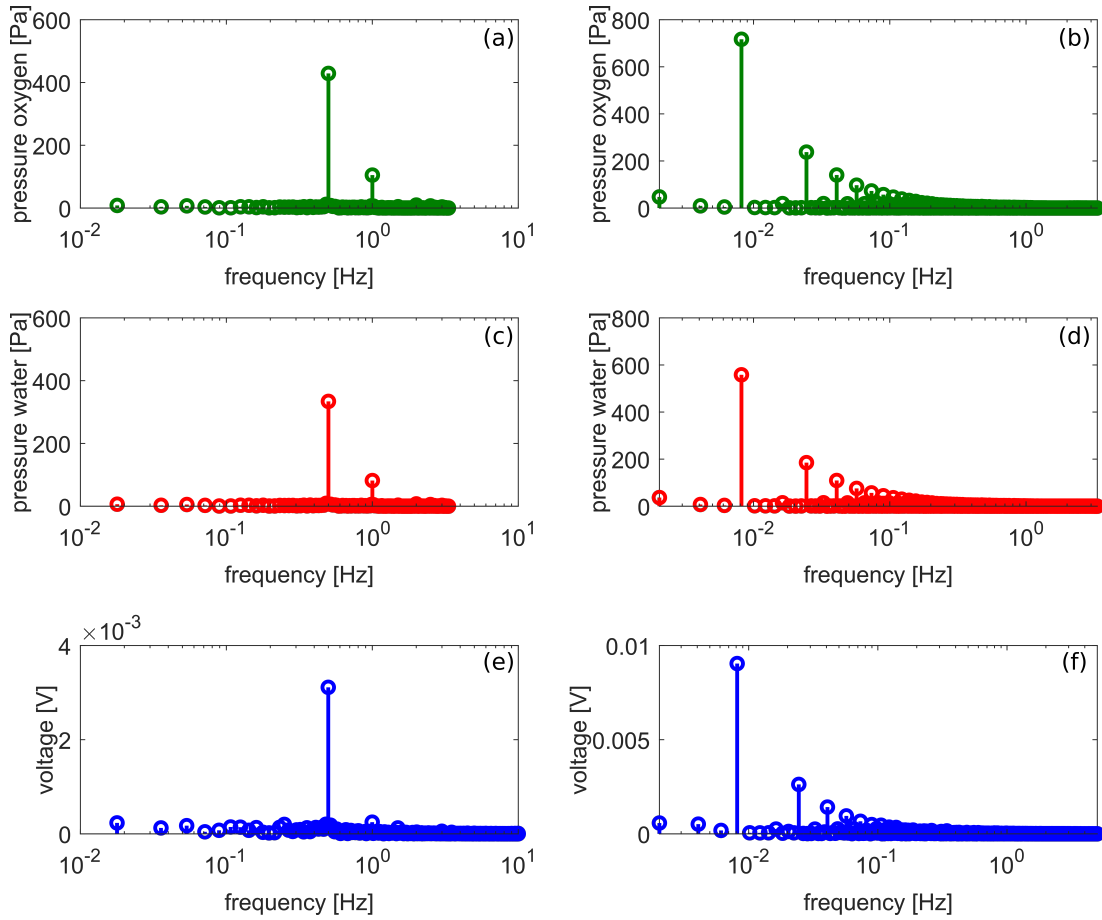
Figure 5.9: Fourier amplitude spectra of periodic partial pressure inputs and voltage output at different frequencies: (a) oxygen pressure input at 500 mHz, (b) oxygen pressure input at 8 mHz, (c) water pressure input at 500 mHz, (d) water pressure input at 8 mHz, (e) voltage output at 500 mHz, (f) voltage output at 8 mHz.

applied to not integer fraction of periods, the phenomenon of the spectral leakage occurs leading to an erroneous evaluation of the harmonics.

An example of magnitude plots of pressure inputs and electrical outputs in frequency domain obtained collecting the fundamental harmonics is shown in the Figure 5.10. Specifically, the spectra collected through the stimulation of the cell by periodic addition of the dry oxygen flow are displayed in the Figure 5.10a, c, e (the ones in the Equation 5.4), while the ones obtained by dry nitrogen flows are depicted in the Figure 5.10b, d, f (the second set in the Equation 5.5). It is noticeable that the amplitudes of the partial pressure inputs increase until the frequencies of 100 mHz prior to achievement of a constant value in both the cases. This depends on the fact that the components of the gas mixture distribute themselves differently depending on the frequency of the periodic perturbation. This is due to a different effect of the Taylor diffusion depending on the frequency of the periodic flow addition. Moreover, the
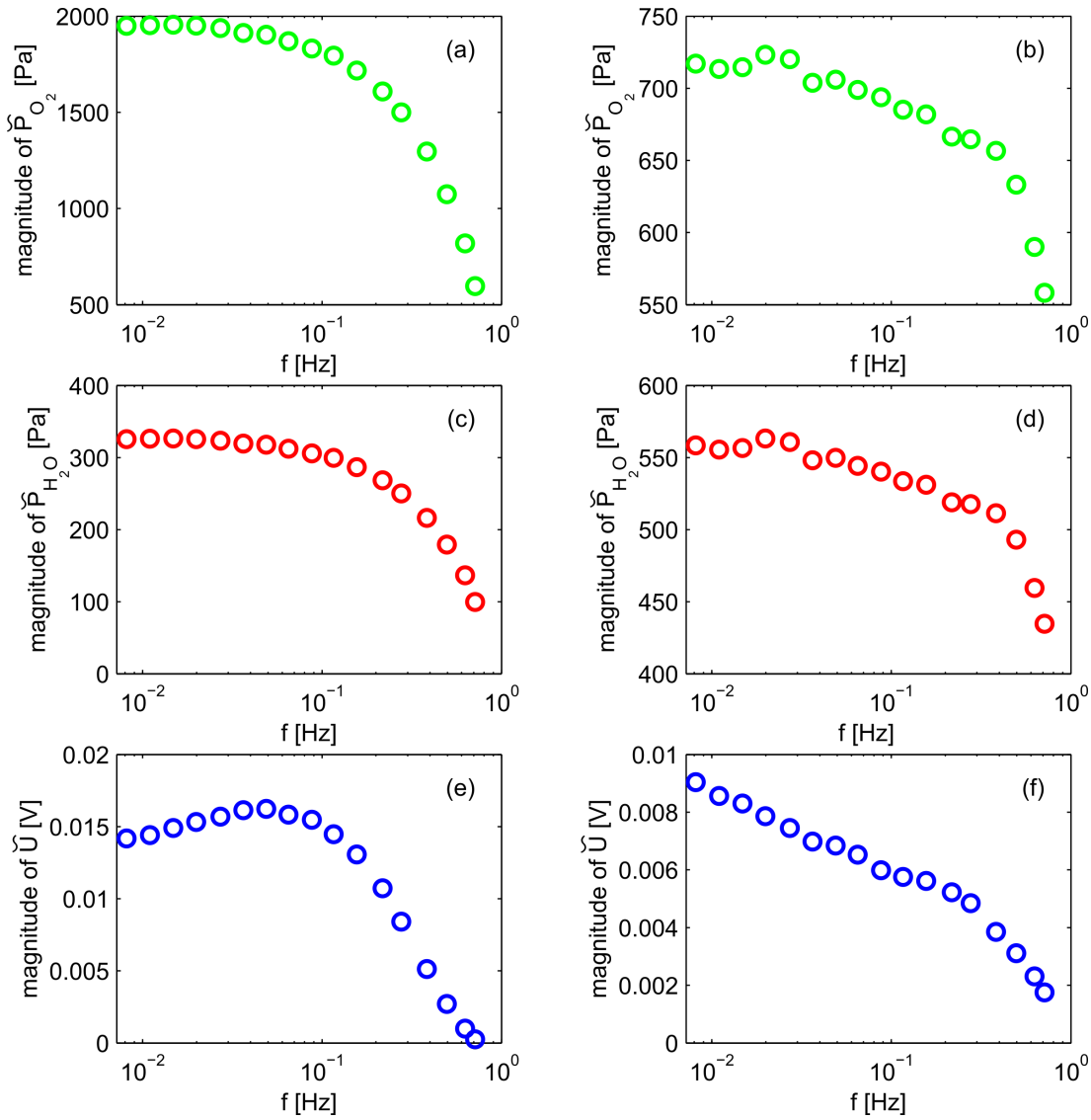
Figure 5.10: Example of pressure inputs and voltage outputs in frequency domain.

magnitude of the voltage response in the Figure 5.10e decreases at lower frequencies, while the one in the Figure 5.10f keeps the increasing trend. In the first case, this behaviour reflects the opposite effects of the simultaneous periodic oxygen and water variation which are out of phase and, consequently, subtract each other. On the other hand, the constructive overlapping in phase of the pressure perturbations in the second case leads to the sum up of the beneficial effects at low frequencies.

5.2.4 Protocol for the determination of CFRA spectra

Combining the mathematical scheme and the spectral data analysis respectively described in the Sections 5.2.1 and 5.2.3 a protocol for the determination of experimental CFRA spectra was developed. The steps of the protocol are described in the following:

(i) Setting of the operating conditions of the experiment defining cathode and anode feed specifications (flow rates, temperature and relative humidity), back pressure and temperature of the cell.

(ii) Setting of the steady state current or voltage; waiting until steady state condition has been achieved in order to not have effect of drifting of the signal in the dynamic measurement.

(iii) Periodic addition to the cathode feed of additional flow of oxygen (6 % of the cathode feed flow rate) by using the switching valve to produce perturbations characterized by a determined set of angular frequencies $\omega = [\omega_1, ..., \omega_n]$; collection of the corresponding partial pressure inputs $P'_{O_2,k}(t)$ and $P'_{H_2O,k}(t)$ and electrical outputs $E'_k(t)$ or $I'_k(t)$ in time domain.

(iv) Periodic addition to the cathode feed of a small flow of nitrogen (6 % of the cathode feed flow rate) by using the switching valve to produce perturbation characterized by the same set of angular frequencies of the step (iii) $\omega = [\omega_1, ..., \omega_n]$; collection of the corresponding second set of partial pressure inputs $P''_{O_2,k}(t)$ and $P''_{H_2O,k}(t)$ and electrical outputs $E''_k(t)$ or $I''_k(t)$ in time domain.

(v) Fourier analysis of inputs and outputs signals registered in the steps (iii) and (iv) and determination of fundamental harmonics.

(vi) Insertion in the equations 5.6 and 5.7 of the values $\tilde{P}_{O_2}(i\omega_k)$, $\tilde{P}_{H_2O}(i\omega_k)$, $\tilde{I}(i\omega_k)$ or $\tilde{E}(i\omega_k)$ obtained in the step (v) for each set of measurements and determination of $\zeta_{O_2}(i\omega_k)$ and $\zeta_{H_2O}(i\omega_k)$ for each element of the set.

In the Figure 5.11, an example of galvanostatic CFRA magnitude Bode spectra obtained from the data shown in the Figure 5.10 following the described protocol are displayed.

It must be remarked that the registration of the signals in time domain in the steps (iii) and (iv) must be performed in quasi-steady state conditions, where there is no drifting component which could affect the spectral analysis. For this reason, prior to any measurement, an certain time was awaited for the stabilization of the quasi steady state at each periodic pressure stimulation.
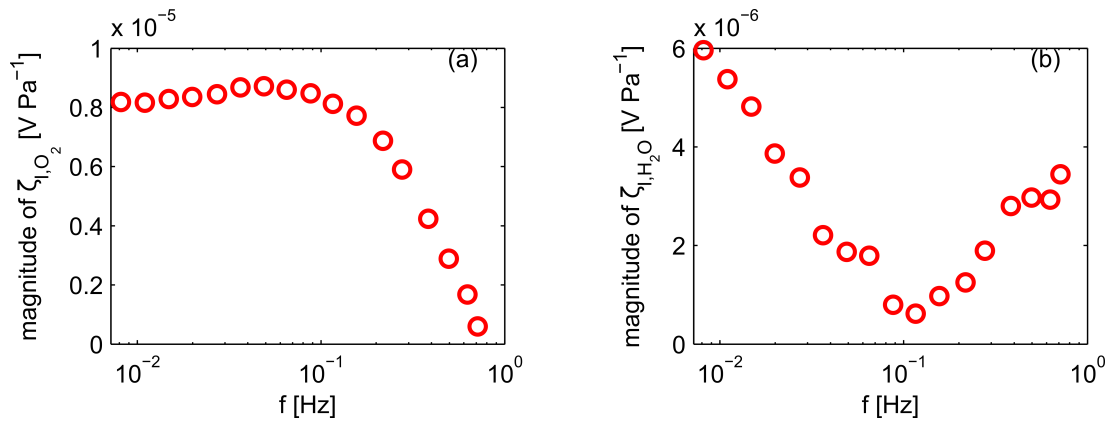
Figure 5.11: Example of magnitude Bode plot spectra of CFRA transfer functions obtained under galvanostatic conditions by different pressure inputs: (a) oxygen partial pressure, (b) water partial pressure.

Chapter 6

Validation of CFRA experimental technique

The experimental protocol described in the Chapter 5 was applied to determine experimental CFRA spectra of a PEMFC system. The obtained results are compared to the theoretical ones in the Section 6.1. First of all, the linearity of the CFRA spectra is evaluated (Section 6.1.2). Then, the predicted features as well as the discrepancies between experiments and simulations are discussed (Sections 6.1.4 and 6.1.5). Hypothesis on the phenomena behind the patterns not predicted by the model simulations are made. In the Section 6.2, the quality of the parameter estimation performed through fitting of spectra of the different CFRA transfer functions and classic EIS is evaluated. Based on the identifiability framework previously presented in the Chapter 4, the performance regarding the reliability of parameter estimated obtained by the different techniques is compared in order to determine the best one to identify a specific set of parameters.

6.1 Validation of CFRA spectra

6.1.1 Experimental operating conditions

The setup described in the Chapter 5 was used to perform all the experiments shown in the following. Additionally, the developed spectral analysis procedure and protocol were used to determine the inputs and outputs in frequency domain and the CFRA transfer functions.

A feed of pure hydrogen with a flow rate fixed at 800 ml/min was supplied to the anode, while the cathode was fed with 600 ml/min of nitrogen and oxygen in air proportion. Both the gas streams were first heated at a temperature of 60 °C before entering in the cell. Dew point temperatures of 55 °C were set for the cathode and anode feed stream corresponding to 30 % relative humidity. The fuel cell hardware is the one described in the Section 5.1.2 using as MEA a Nafion 115 membrane coated

with advanced surface area carbon platinum catalyst provided by Quintech. The temperature of the cell was set to 80°C. A value of 20 ml/min was used as additional flow rate of oxygen to produce the periodic pressure perturbations out of phase (first data set), while 30 ml/min of nitrogen for the ones in phase (second data set).

6.1.2   Linearity assessment of CFRA spectra

Prior to the experiments showed in this section, the linearity of the measured CFRA transfer functions was verified. Since the inputs and outputs at lower frequencies present a periodic square wave shape instead of a sinusoidal one, the evaluation of linearity based on total harmonic distortions of the signal used in the Section 4.5 was inapplicable. For this reason, the homogeneity principle was employed instead. Accordingly, the CFRA transfer functions were determined twice using two different values of amplitude of the partial pressure inputs. If the resulted spectra were invariant to the change of the input, the linearity condition was assumed to hold in the range of the input amplitude considered.

An example of the application of this procedure is displayed in the Figure 6.1. At first, oxygen pressure perturbations with a maximum amplitude of 2000 Pa were used to measure galvanostatic and voltastatic CFRA transfer functions (red dots). Then, the measurements were repeated by applying a perturbation which the amplitude was half of the previous one (cyan dots). As it can be seen, the obtained CFRA magnitude Bode plots are not affected by the value of the amplitude of the input under both galvanostatic and voltastatic control. An observed slight variation could be be attributed to the decrease of the signal to noise ratio of the input and output signals. The signal to noise ratio, which quantifies the contribution of the ground noise on a measured signal, presents a quadratic and inverse proportional dependence on the value of the amplitude. Therefore, using half amplitude, this parameter lowers of a factor of 0.25 implying that the measurement are more affected by noise interference. According to this, the electric response of the system could be considered linear.

6.1.3   Parameter estimation setting

The experimental spectra were measured at the same steady state conditions considered in Chapter 4 in order to compare them to the previous results of the theoretical study and reproduce kinetic activation, ohmic and mass transport regimes. In this case, classic EIS spectra are used as reference to depict the different dynamics detected.

The developed PEMFC model was employed to fit all the experimental spectra shown in this chapter. The fitted parameters are the same considered in the identifiability analysis reported in the Section 4.3.2. Different ranges for the variation of each parameter were set according to physicochemical considerations in order to perform a meaningful validation analysis. The cathode transfer coefficient α_c was varied with respect to a range of values between 0.2 and 1, as suggested by several reports in the literature [135]. The exchange current density i_0 resulted to have a low impact
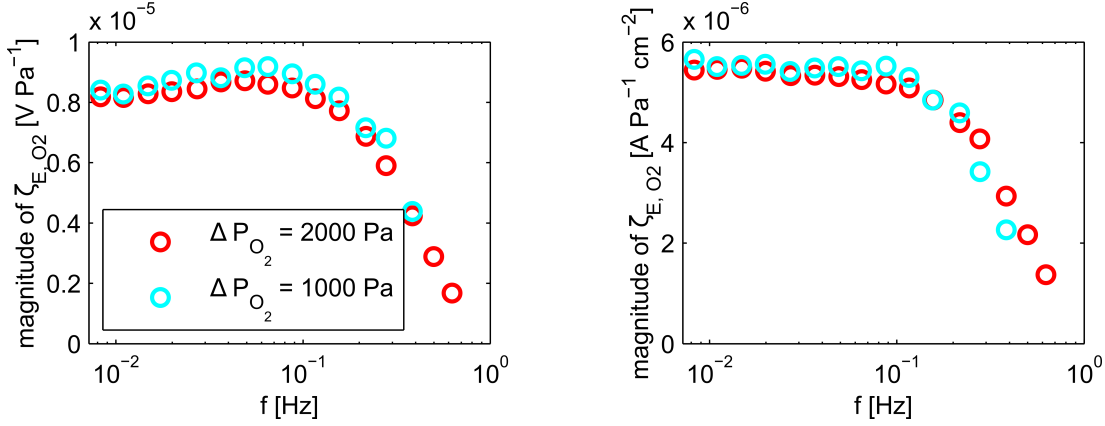
Figure 6.1: Magnitude Bode plots of CFRA measured under galvanostatic (a) and voltastatic (b) control using oxygen partial pressure perturbations using two different values of the input amplitudes.

on the CFRA spectra and, for this reason, its value was fixed. The effective porosities ε_{O_2} and ε_{H_2O} respectively related to the oxygen and water diffusion in the GDL were estimated to quantify the resistance to the gas transport in the electrode on the cathode side. Their values were separately fitted by varying them in a range between 0.03 and 1. The separated estimation of these parameters is physically meaningless, but it allows in practice to evaluate individually the transport resistances related to the two species, which could be significantly different due to accumulation of liquid water in the electrode. Finally, the nominal diffusion coefficient of water in Nafion $D_{H_2O}^{0,M}$ and the electroosmotic drag constant K_{H^+} characterizing the transport of water in the membrane were fitted (Chapter 4). According to the work of Vetter and Schumacher [194, 195], the values of these two parameters are the most uncertain among the ones determining the performance of PEMFCs due to the lack of precise experimental techniques capable to measure them. Their fitting was performed by varying them by a factor in a range between 0.5 and 60 respect to the base case value.

The fitting procedure was performed in order to find a set of parameters for each FRA interpolating the spectra at all the steady state conditions. For this purpose, the MATLAB® function *sqnonlin* was employed to minimize the least square between the experimental magnitude Bode plots and the simulated ones. The estimated optimal parameters for each FRA transfer function are listed in the Table 6.1. It is remarkable that the values of the parameters largely differ in some cases depending of the transfer function fitted to estimate them. An example is the transfer coefficient α_c which the estimated values are scattered from 0.36 to 0.98. The reason of these discrepancies and the quality of parameter estimation are further discussed in the Section 6.2.

Technique	α_c	ε_{O_2}	ε_{H_2O}	$D_{H_2O}^M$	K_{H^+}
EIS	0,43	0,03	0,04	1,01	1
CFRA(O_2) vol.	0.98	0.52	0.59	0.81	2.47
CFRA(O_2) gal.	0.85	0.037	0.93	0.73	0.93
CFRA(H_2O) vol.	0.63	0.15	0.15	0.96	1.13
CFRA(H_2O) gal.	0.36	0.035	1	3.1	3.22

Table 6.1: Set of parameters fitted for the validation of the CFRA techniques. For the parameters $D_{H_2O}^M$ and K_{H^+}, the multiplicative factors with respect to the base case values are reported.

6.1.4 Validation of CFRA spectra obtained by oxygen pressure perturbations

The experimental EIS spectra already shown in the Chapter 4 are newly displayed in the Figure 6.2. Unlike the previous EIS spectra, they are shown in the frequency range below 1 Hz which represents the frequency limit due to the restrictions of the CFRA setup. This frequency range is kept in all the FRA spectra shown in this chapter. EIS spectra are used here as reference case in order to compare the dynamics observed with the ones detected through other FRA techniques. The value of the magnitude of the EIS (Figure 6.2a) around 1 HZ decreases with the increase of the steady state current density indicating an expected lowering of the kinetic resistance. In the considered region of the spectra, the influence of two dynamics with opposite effects on the cell performance are observed: (i) the transport of the oxygen in the cathode channel (frequency range 0.1-1 Hz), (ii) the sorption of the water produced through ORR in Nafion causing an increase of the proton conductivity (frequency below 80 mHz). The two phenomena are also detected in the phase Bode plot (Figure 6.2b) respectively by a positive and a negative angle peak, as well as in the Nyquist plot (Figure 6.2c) where a capacitive arc for the oxygen transport and an inductive loop related to the water transport in Nafion appears. It is noticeable that the impact of the oxygen transport resistance dramatically increases at the highest current density due to higher accumulation of water inside the porous structure of the GDL. As already seen, this phenomenon has only a quantitative impact on the spectra, since the time of the dynamic response is dominated by the slower gas transport in the channel.

The fitted spectra quantitatively underestimate the magnitude of the impedance at the steady state current of 100 mA cm^{-2} and 200 mA cm^{-2}, while the one at 300 mA cm^{-2} matches better the data. The predicted response of membrane hydration is slower and occurs at lower frequencies. The same fitting accuracy is obtained for the Nyquist plot, whereas the phase angle shows a good quantitative agreement at all the steady state current. The reason of these discrepancies is mainly due to the simplicity of the model which is not able to predict the changes of the physical parameters of the cell components along the operating conditions investigated.

The CFRA spectra obtained by oxygen partial pressure perturbations are shown in
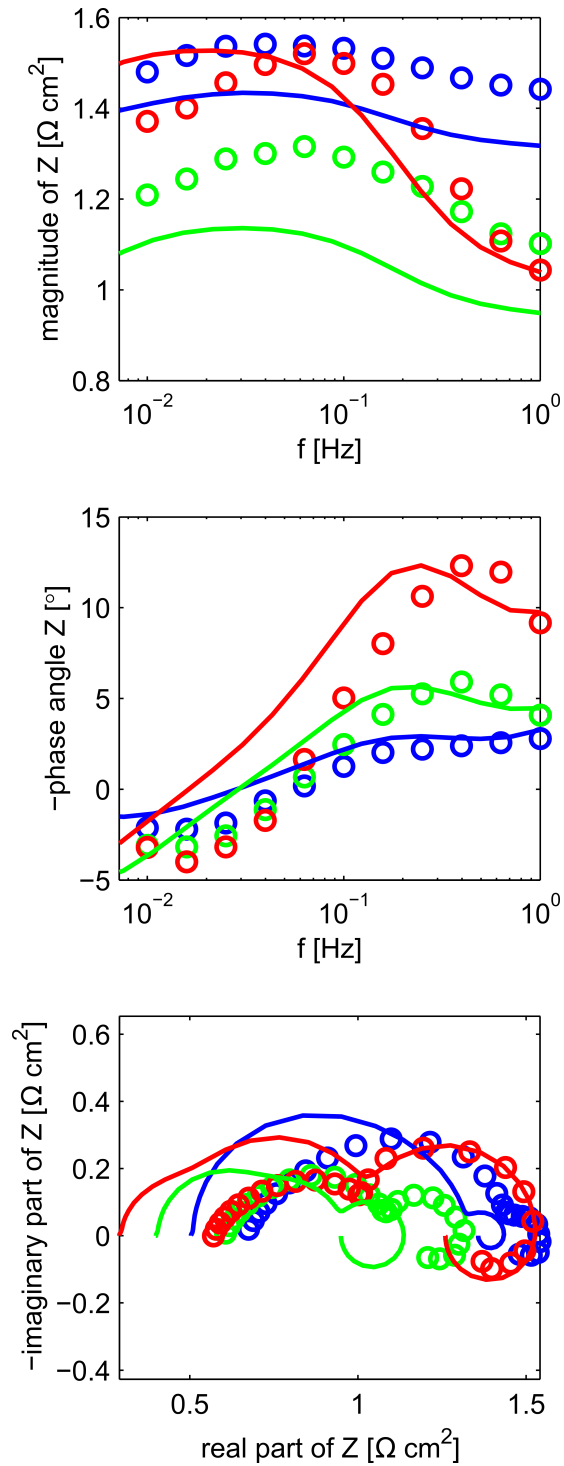
Figure 6.2: Experimental (circle markers) and fitted simulated (solid line) EIS spectra: (a) magnitude Bode plot, (b) phase Bode plot, (c) Nyquist plot.

the Figure 6.3. In the Figure 6.3a, CFRA magnitude Bode plot obtained by periodic oxygen pressure inputs under galvanostatic conditions are displayed. The experimental data match the fitted ones with good accuracy along all the steady state conditions verifying the features predicted in the theoretical studies. All the spectra approach to zero at the frequency around 1 Hz confirming that the effect of the pressure input on the fuel cell electric output is dominated by the time required to the gas to flow in the channel and diffuse in the GDL. For this reason, the effects of transients which are faster than this phenomenon, as for example the charging of the double layer, cannot be detected. The dynamics related to the gas transport in the channel is the only dynamics observed. As predicted by the model, the CFRA magnitude is constant at lower frequency where the effect of the hydration of the Nafion membrane should be detected. Then, it can be confirmed that the rate of water production by ORR and the electroosmotic flux are constant under galvanostatic control, and the water content in the membrane is, consequently, unchanged. For this reason, there is no variation of the ohmic resistance related to the membrane.

A slight decrease of the magnitude is only observed in the spectra collected at 300 mA cm^{-2} in the frequency region between 20 mHz and 70 mHz. This range is higher than the one in which the dynamics of water sorption in Nafion are observed. A phenomenon which could originate such a path is the desorption of intermediate species of the ORR which the effect has been observed in EIS spectra in that frequency region [141]. However, this statement has not been currently proved and further theoretical and experimental studies should be performed in this direction.

The value of the magnitude increases along with the current density showing a proportionality with mass transport resistance. This behaviour is also predicted by the model. Such a relation can also be verified making some remarks on the ORR kinetic. Considering an ORR kinetics of the first order with respect to the oxygen pressure (Equation 4.18) , and assuming that the voltage variation in the CFRA experiments under galvanostatic control are only due to the change in the cathode overpotential ($\Delta \tilde{E} (i\omega) = \Delta \tilde{\eta}_c (i\omega)$), the magnitude at lower frequency reads:

$$| \zeta_{I,O_2} (\omega \to 0) | = \frac{\partial \eta_c}{\partial P_{O_2}} = \frac{RT}{\alpha_c F P_{O_2}^{CL}}. \tag{6.1}$$

It is clear from the Equation 6.1 that the value of the galvanostatic CFRA magnitude is inversely proportional to the oxygen pressure at the catalyst interface. Therefore, this representation of the transfer function can be used as evaluation of the increase of mass transport resistances impeding the path of the oxygen to the catalyst. This monotonic dependence is not verified with classic EIS because of the coupling of the effects of different processes which contributes in different way to the overall value of the impedance.

Unlike the case of galvanostatic control, in the experimental magnitude Bode plot of the volstastatic CFRA (Figure 6.3d), the dynamics related to the hydration of Nafion are detected. After the initial increase of the magnitude in the frequency region associated to gas transport in the channel, another slight increment is observed for the spectra
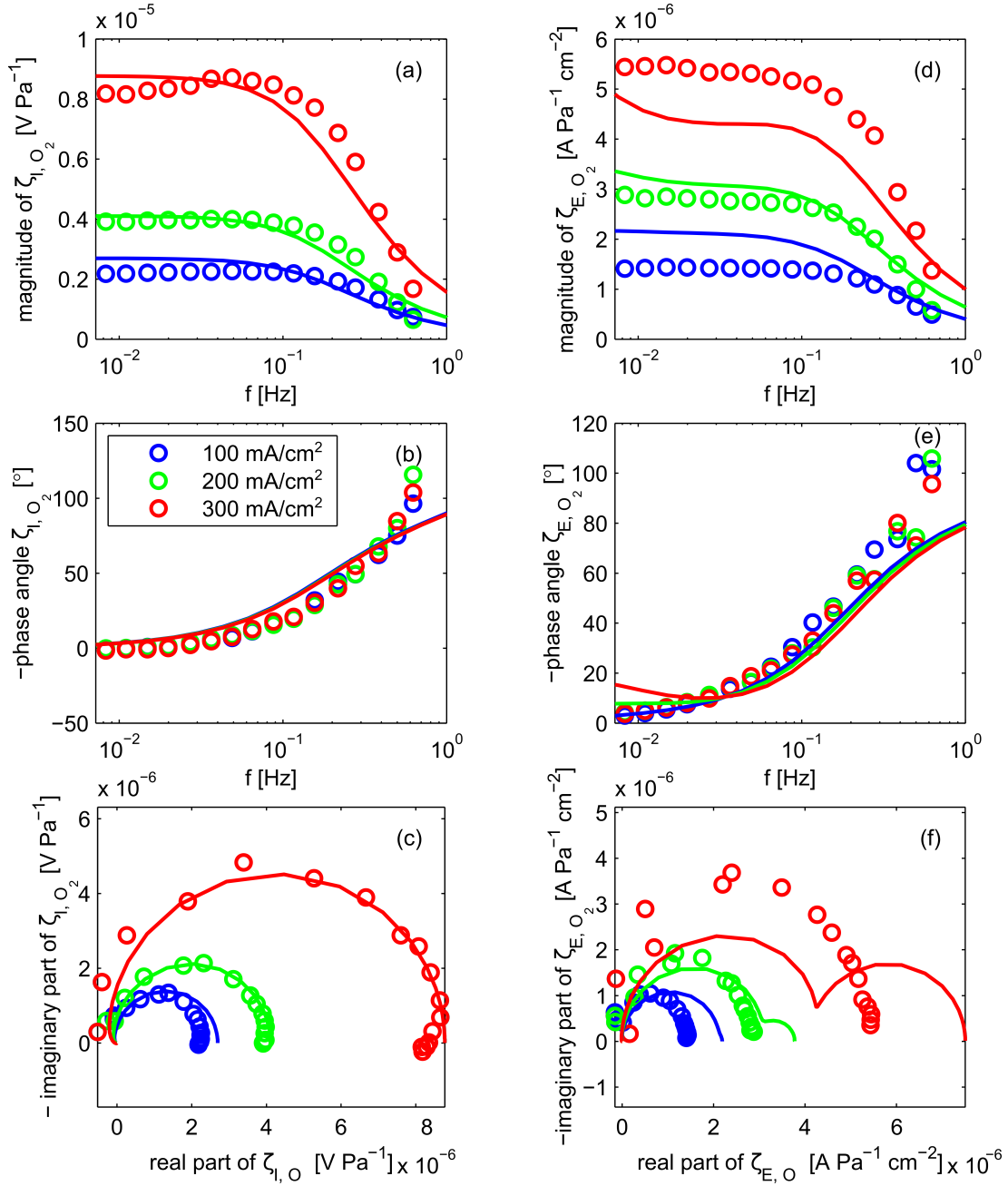
Figure 6.3: CFRA spectra obtained by using oxygen partia pressure inputs at three different steady state conditions: galvanostatic CFRA (a), (b) and (c); voltastatic CFRA (d), (e) and (f).

collected at 200 mA cm^{-2} and 300 mA cm^{-2} below 30 mHz. As seen in the theoretical studies (Figure 4.6), oxygen pressure changes under voltastatic conditions affect the ORR rate leading to a variation of water production which is absorbed in part by the membrane. Because of the beneficial influence of the increase of water content on the

proton transport, the ohmic resistance decreases improving the current response and leading to a consequent rise of the magnitude of the CFRA.

The fitted spectra match the experimental results with a lower accuracy with respect to the galvanostatic ones. Nevertheless, they correctly reproduce the qualitative trend. It is particularly remarkable that the simulated spectra overestimate the contribution of the membrane hydration.This could be due to the inadequacy of the used constitutive equations to describe the dependence of the transport parameters on the water content in the membrane under the experimental conditions considered.

Also in this case, an increase of the magnitude along with the steady state current density is observed. Considering the used kinetic expression of the ORR (Equation 4.18), the value of the spectra at the plateau prior to the contribution of the membrane hydration (frequency range $20 < \omega < 87mHz$) is equivalent to :

$$| \, \zeta_{I,O_2} \, (20 < \omega < 87mHz) \, | = \frac{\partial j}{\partial P_{O_2}^{CL}} = i_0 exp \left(-\frac{F\alpha_c}{RT} \eta_{c,ss} \right). \tag{6.2}$$

The symbol $\eta_{c,ss}$ stands for the steady state cathode overpotential which is negative for cathodic reactions. Since the absolute value of $\eta_{c,ss}$ increases along the current due to the higher mass transport resistance, the magnitude of ζ_{I,O_2} will raise as well.

The experimental phase angle plots (Figures 6.3b, e) are in good qualitative and quantitative agreement with the simulated ones reflecting the typical behaviour of systems characterized by a time delay between the input and the effect on the output. Accordingly, the phase dramatically increases at higher frequencies achieving values larger than $360°$. As explained in the Section 4.2.2, the delay is due the time required to the partial pressure perturbation to propagate in the channel, diffuse in the GDL and achieve the catalyst surface changing the electric response. The different experimental conditions have a negligible effect on the value of the phases which diverge maximum of 5 ° from each other. This suggests that the time delay between the pressure input and the electrical output does not change significantly along with the steady state current densities. Additionally, the value of the phase spectra determined at the lowest frequency is about zero for the galvanostatic CFRA collected at 300 mA cm^{-2} (Figure 6.3b) indicating that no dynamics processes are acting in the corresponding range of time. On the contrary, a phase about $4°$ is observed in voltastatic CFRA spectra (Figure 6.3e) confirming the detection of the membrane hydration process already seen in the magnitude plots.

The shape of the experimental Nyquist plots are consistent with the other representations of the CFRA transfer functions. Only one arc is obtained for all the three experimental conditions under galvanostatic control (Figure 6.3c), as the spectra are affected only by one dynamics (gas transport in the channel). On the other hand, the Nyquist plot of the voltastatic CFRA (Figure 6.3f) presents an additional slight arc better visible at the highest current density which is due to the dynamics related to the membrane hydration.

The spiral predicted by the model at higher frequency is not completely observed in the experimental spectra. In the higher frequency region of the Nyquist plots of

galvanostatic CFRA (Figure 6.4), only the initial part of the spiral is detected, which is visible especially in the spectra registered at 300 mA cm^{-2} (red dots). It can be seen that the experimental diagram enters in the second quadrant with negative real axes approaching to cross it. As previously explained (Section 4), the time constant of the process delaying the input can be estimated by the frequency at which the Nyquist plot cross the real negative axes through the Equation 4.33. The experimental point collected at the highest frequency in the Figure 6.4 can be considered as approximation of this intersection point giving the value of 0.42 s as time delay. This value is significantly larger from the one calculated by the model. This difference can be due to the fact that only the GDL is considered as spatially distributed element in the model, while the channel is assumed to be a lumped element where the transport along the space is immediate. Additionally, the mass transport in the cell is characterized by gradient along axial direction of the the channel which has not been considered in the theoretical studies and could have an influence on this pattern. Moreover, the gas transport in the channel is one generally slower than the one in the GDL contributing the most to the delay of the response [130]. This feature of the CFRA spectra gives the possibility to obtain precise estimation about the time of transport inside the cathode electrode of the fuel cell.
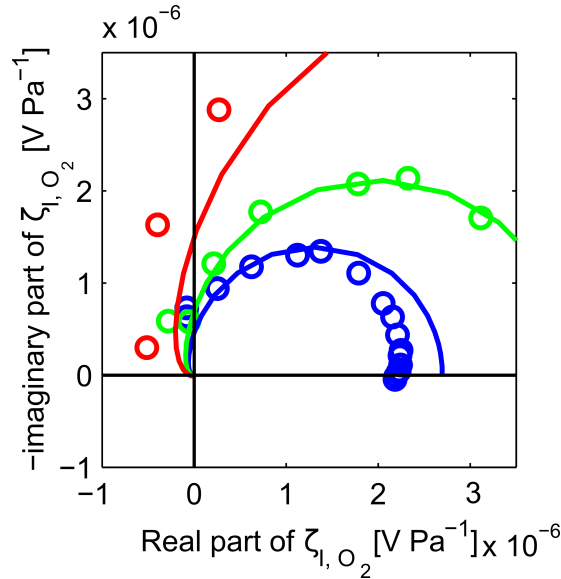
Figure 6.4: Spiral behaviour observed at higher frequencies in the Nyquist plots of galvanostatic CFRA tranfer function obtained by oxygen pressure perturbation.

In order to further prove the inverse relationship between the magnitude of the spectra and the pressure of oxygen at the catalyst interface (Equations 6.1 and 6.2), CFRA experiments were performed using inlet flows with different composition of oxygen. Specifically, the flow rate of the oxygen sent to the cell was increased, while the one of the nitrogen was decreased of the same extent to keep the same value of the total flow rate. Additionally, the same value of the steady state current was set for

all the measurements. In this way, the water content inside the cathode electrode was supposed to be constant along the experiments, as the main parameters influencing the liquid water distribution (the velocity of the gas inside the flow fields and the water production by the ORR at the cathode) were kept unchanged. For this reason, the variation of the mass transport resistance could be assumed to be only due to the different partial pressure in the inlet flow. The spectra so obtained are shown in the Figure 6.5 for both the electric control galvanostatic (Figure 6.5a-b) and voltastatic (Figure 6.5c-d). As it can be seen, the value of the magnitude dramatically decreases as the employed flow rate of oxygen decreases in the two cases confirming the expected trend. Then, it is noticeable that the increase of the volstastatic magnitude spectra (Figure 6.5c) at lower frequency due to the sorption of the water in the Nafion membrane is more visible in the case of the highest flow rate of oxygen. This is could be probably because the effect of this phenomenon is less masked by the gas mass transport which is lower under these conditions and, consequently, more visible. Moreover, it is remarkable that the magnitude spectra converge to zero at higher frequencies. In the voltastatic magnitude at lower oxygen inlet pressure (see cyan and magenta plots in the Figure 6.5), a minimum point at zero seems to be achieved. This patterns are characteristic of resonance phenomena due to the distributed effect of the input perturbation [196]. The discussion of this aspect is postponed to the next section.

The phase plots show a different behaviour depending on the electric control. While they are not influenced from this operating parameter under galvanostatic conditions, a decrease is observed at higher frequencies for the phase related to the lowest value considered for the oxygen flow rate. Additionally, the measured points of the spectra tend to be scattered in this frequency region.

6.1.5 Validation of CFRA spectra obtained by water pressure perturbations

CFRA spectra obtained by water concentration perturbations at the same seady state conditions of the previous ones are displayed in the Figure 6.6. The magnitude Bode plots of the galvanostatic transfer function (Figure 6.6a) match with good agreement the simulated ones at the steady state current of 100 mA cm^{-2} and 200 mA cm^{-2}. The periodic water pressure inputs have a low influence on the electric response at high frequencies. The spectra start to increase significantly below the frequency of 100 mHz selectively detecting the dynamics of the sorption of water in the Nafion membrane as predicted by the model. However, the magnitude registered at 300 mA cm^{-2} presents a maximum peak around 1 Hz prior to the increment at lower frequency. This path is not predicted by the model.

In the case of the magnitude registered under voltastatic control (Figure 6.6d), the simulated spectra reproduce the experimental ones at low frequencies, while the patterns, which have not been predicted, are observed at higher frequencies for all the steady states. Additionally, the spectra are shifted towards lower frequencies with re-
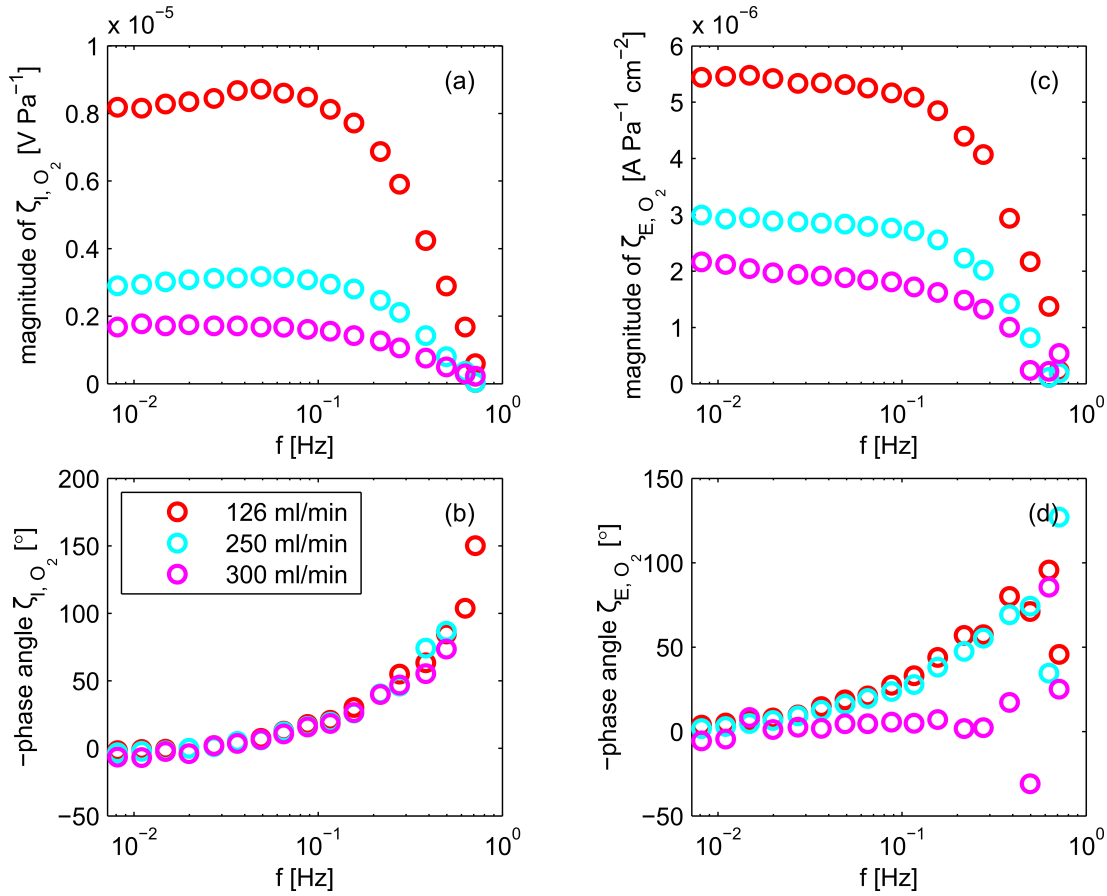
Figure 6.5: Experimental CFRA spectra obtained by oxygen partial pressure measured using different values of oxygen flow rate at a steady state current density of 300 mA cm^{-2} : (a)-(b) magnitude and phase Bode plots of galvanostatic CFRA, (c)-(d) magnitude and phase Bode plots of voltastatic CFRA.

spect to the galvanostatic ones. This trend suggests a slower transport of water in the membrane under voltastatic control. This is probably due to the fact that the current changes consequent to the water pressure perturbation leads to the variation of the electroosmotic drag force in the Nafion under this control regime. As this flux is opposite to the diffusion of the produced water from anode to cathode, it consequently could make the total water flux in the membrane decreasing, slowing down the sorption process. On the other hand, in galvanostatic conditions, the transport of water is mainly driven by the diffusion without changes in the electroosmotic forces and could be faster. This different features in CFRA spectra under voltastatic and galvanostatic control could allow to study separately the transport in the membrane driven by diffusion mechanism and evaluate the impact of the electroosmotic flux on the dynamics of sorption of the water.

As in the case of the magnitude, the fitted phase angle Bode plots agree with the ex-
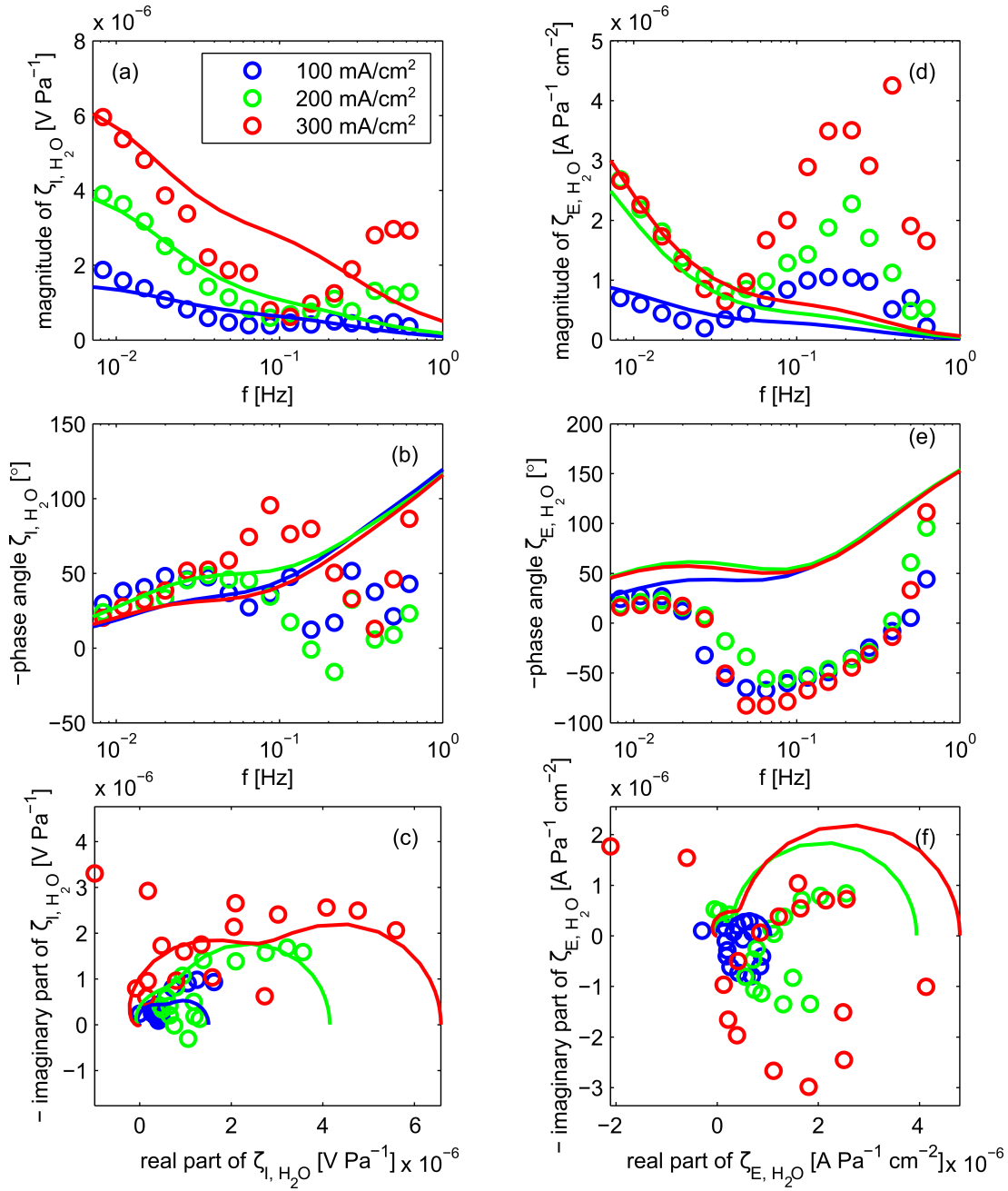
Figure 6.6: CFRA spectra obtained by water partial pressure perturbations under galvanostatic control (a), (c), (e) and voltastatic control (b), (d), (f) at three different steady state current densities.

perimental ones at lower frequencies, while some discrepancies are observed at higher ones. For example, in the galvanostatic phase plot (Figure 6.6b), it is visible a not predicted maximum and minimum respectively at the frequency of 90 mHz and 400 mHz in the spectra collected at 300 mA cm^{-2} (red plot). Similarly, the voltastatic

phase plots (Figure 6.6e) display a minimum around 60 Hz in the negative region of the diagram which is also not reproduced by the model. In both the cases, an increasing asymptotic behaviour is observed at the highest frequencies similar to the one seen in the CFRA phase plots obtained by oxygen perturbation. This pattern indicates an analog delay between input and output which is probably due to the diffusion of the water partial pressure perturbation in the electrode and membrane.

The experimental Nyquist plots (Figure 6.6c, f) are reproduced by the model only at the lower frequencies. As observed in the spectra collected at 300 mA cm^{-2}, the diagram approaches the second quadrant with negative real and positive imaginary axes at high frequencies under galvanostatic control. Under voltastatic control, the Nyquist plots present an additional arc in the fourth quadrant with negative imaginary and positive real axes. In both cases, the collected points are enough to determine the time constant of the the transport of water in Nafion from the characteristic frequencies at the top of the arc at lower frequencies. In this way, the values of 15 mHz and 8 mHz were determined respectively for the galvanostatic and voltastatic case.

Two type of hypothesis are given on the dynamics originating the not predicted patterns at higher frequencies: (i) the action of a two or more contrasting dynamic process with opposite effects on the fuel cell response, (ii) a resonance behaviour due to the spatially distributed effect of the water pressure perturbations.

In the first case, one of the two contrasting dynamics involved in the generation of the pattern could be the water sorption in Nafion which increases the magnitude of the electric response by lowering the ohmic resistance of the fuel cell. The two possible phenomena opposing to this beneficial effects could be the accumulation of the liquid water in the porous structure of the cathode GDL and catalyst layer, or the dehydration of the ionomers on the anode side due to the electroosmotic flux. The change of the water pressure can influence the content of liquid water retained in the GDL which can increase reducing the porosity. As consequence, the free path available for the oxygen to achieve the catalyst layer decreases bringing to an increase of the performance losses due to mass transport. On the other hand, the resulting increase of the current density and of the hydration level of the membrane due to the water perturbations could lead to a temporary dehydration of the ionomer on the anode side [131, 132]. As result, the ohmic resistance increases. As seen in the Section 2.2.3, each of these phenomena occurs in the frequency range in which the unexpected patterns of the CFRA spectra are observed. According to this hypothesis, the minimum observed in the magnitude Bode plot would occur when the effects of the two contrasting processes are equal in their absolute value.

The hypothesis of the resonance behaviour is discussed in the next section.

In the Figure 6.7, CFRA magnitude and phase Bode plots obtained by water partial pressure inputs at different flow rate of oxygen are shown. The operating conditions are the same of the spectra displayed in the Figure 6.5. As it can be seen, the galvanostatic and voltastatic CFRA magnitude is not significantly affected by this parameter at lower frequencies. This trend was expected, since this FRA technique detects the dynamics related to the water sorption in Nafion and, as pointed out previously, the
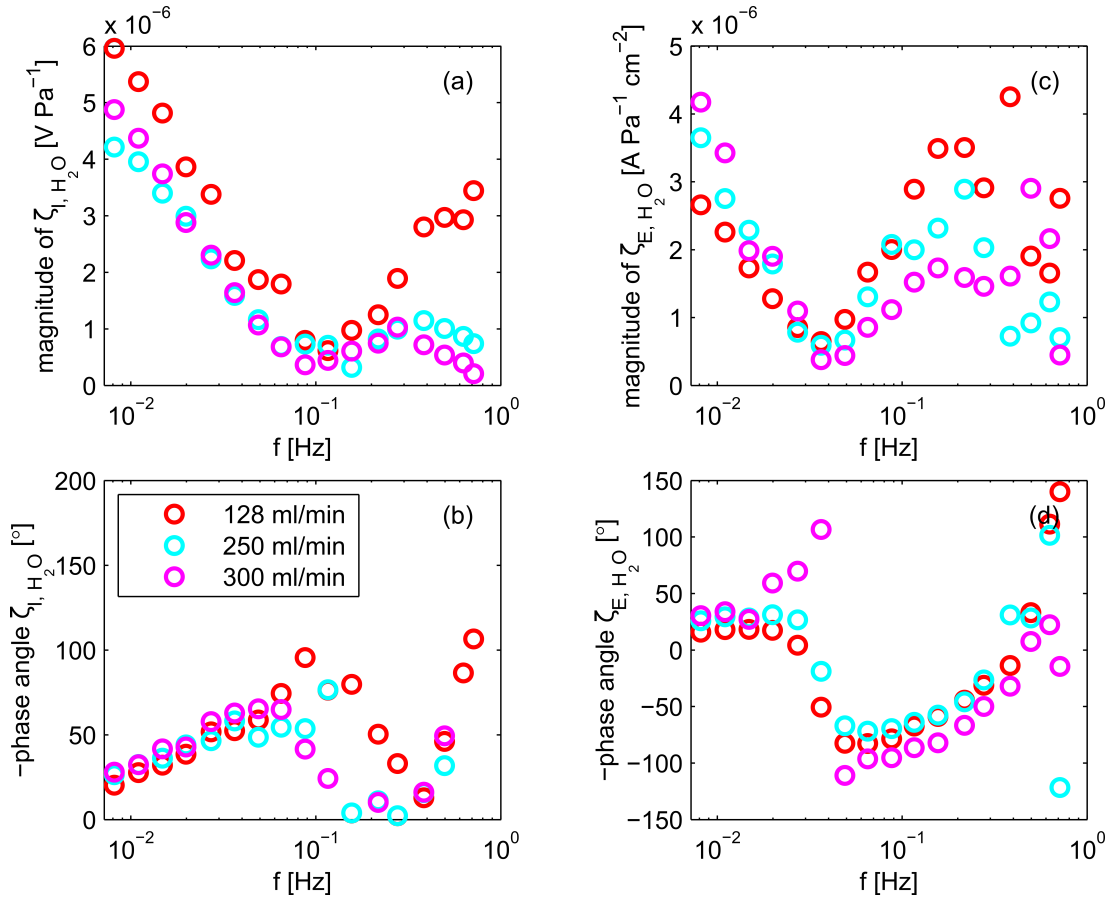
Figure 6.7: Experimental CFRA spectra obtained by water partial pressure inputs measured using different values of oxygen flow rate at 300 mA cm^{-2} : (a)-(b) magnitude and phase Bode plots of galvanostatic CFRA, (c)-(d) magnitude and phase Bode plots of voltastatic CFRA.

distribution of the water in the different layers of the fuel cell along the different measurements is supposed to be unchanged under these conditions. On the other hand, there is a decrease of the value of the maximum point observed at higher frequencies along with increment of oxygen flow rate. This suggests that the phenomena related to this path could be connected to the mass transport resistance of the gas (transport in the channel, liquid water, etc.). The phase Bode plots (Figure 6.5b, d) only present slight quantitative differences between each other, but the patterns are the same ones observed in the previous spectra.

The influence of the humidification of the cathode feed on the CFRA spectra by water pressure input is displayed in the Figure 6.8. Two different dew point temperature values are set for the cathode feeds in the results showed (the base case value of 55 °C in red and 35 °C in black). This parameter has a significant influence on both galvanostatic and voltastatic magnitude Bode plots, but different on the qualitative point
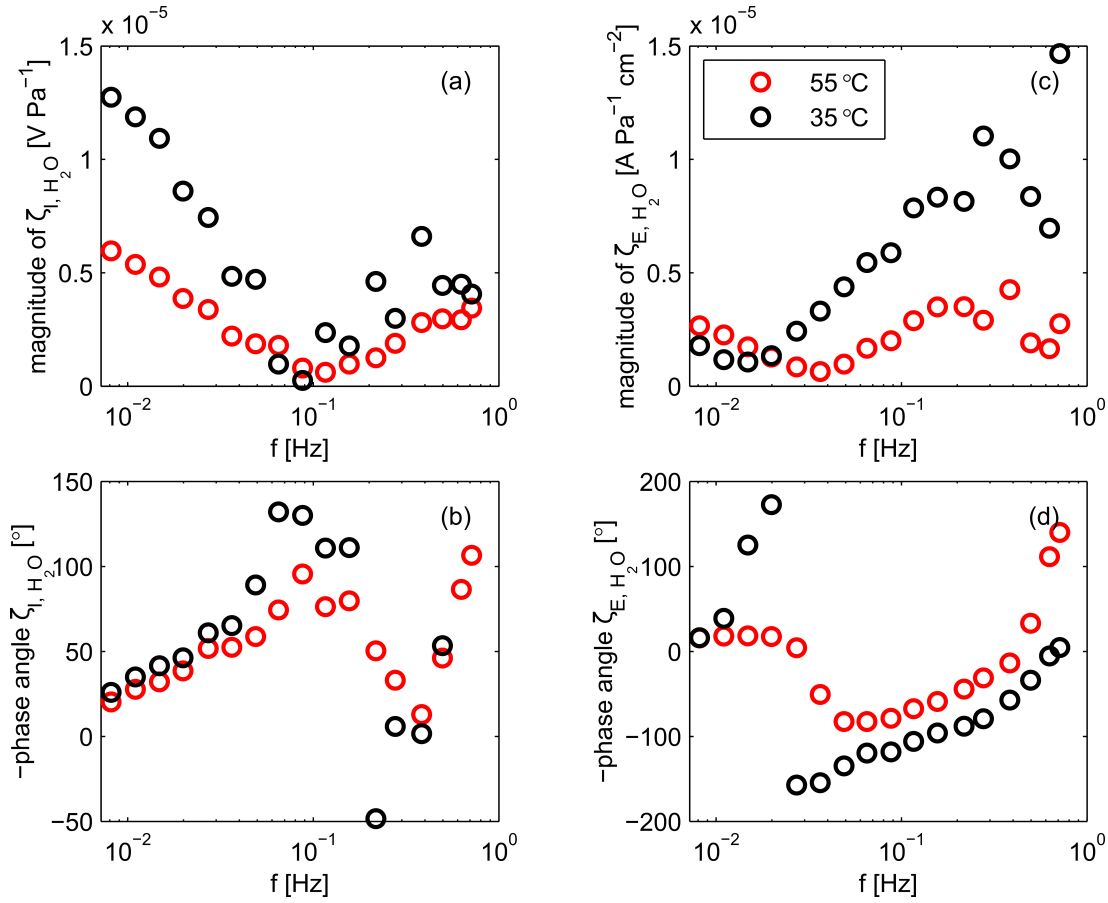
Figure 6.8: Experimental CFRA spectra obtained by water partial pressure inputs measured setting different values of dew point temperature at 300 mA cm^{-2}: (a)-(b) magnitude and phase Bode plots of galvanostatic CFRA, (c)-(d) magnitude and phase Bode plots of voltastatic CFRA.

of view. Higher values are obtained at lower humidification of the feed with respect to the base case under galvanostatic control (Figure 6.8a, c black circle markers). On the contrary, a decrease of magnitude is registered at lower frequencies under voltastatic control. Moreover, the spectra at this control option are shifted at lower frequencies suggesting a slowing down of the dynamics involved. The phase Bode plots are only quantitatively affected by the change of the dew point temperature. Therefore, the two Figures 6.7 and 6.8 confirm the capability of the CFRA by water partial pressure to selectively detect mostly the phenomena related to the transport of water in a PEMFC and monitor the dynamic response of them.

6.1.6 Effect of resonance phenomena in CFRA experiment

As seen in the previous sections, characteristic patterns of resonance phenomena are observed in the experimental CFRA spectra obtained using both oxygen and water partial pressure as input. Resonances occurs when a periodic perturbation has a distributed effect along certain spatial coordinates of a system. They have been widely observed in FRA experiments on heat exchangers involving flow perturbations [196]. Fahidy theoretically predicted in his work [197] the effect of resonance for electrochemical reactors in transfer functions based on concentration inputs. However, no experimental evidence of these phenomena were observed so far to our knowledge.

During the CFRA experiments, the periodic partial pressure perturbation is distributed not only towards the sandwich coordinate, but along the channel as well. Therefore, the global electrical response is given by the integration of the local variations of current and voltage along this direction. In order to verify the rise of resonances due to this spatially distributed response in CFRA by oxygen input and find out if they could be related to the patterns observed, a simplified PEMFC channel model was developed.

The following model aims to describe exclusively the effect of the distribution of the oxygen pressure along the channel on the electric response. For these reasons, most of the dynamics connected to other phenomena are not contemplated. Only variations along the axial coordinate y of the channel are considered. The transport of oxygen is the only one simulated without taking into account effects related to the liquid water. Moreover, the transport in the GDL and catalyst layer, as well as the water sorption in Nafion are neglected. The contribution of the anode to the electric response of the cell is also considered negligible. Then, according to these assumptions, the mass balance of oxygen in the channel reads:

$$\frac{\partial P_{O_2}^{CH}}{\partial t} = -\frac{\partial u P_{O_2}^{CH}}{\partial y} + RT \frac{r_{ORR}(y)}{H^{CH}} \tag{6.3}$$

where u is the velocity of the gas in the channel and H the height of the channel. The boundary conditions required to solve the partial differential equation above are respectively:

$$P_{O_2}^{CH}(t=0,y) = P_{O_2,in}(t) \tag{6.4}$$

$$P_{O_2}^{CH}(t,y=0) = P_{O_2,in} \tag{6.5}$$

$$\tag{6.6}$$

The formulated charge balance at the cathode catalyst interface is a spatially distributed version of the one expressed in the Equation 4.16:

$$C_c^{DL} \frac{\partial \eta_c}{\partial t} = j(y) + 4F r_{ORR}(y). \tag{6.7}$$

As in the previous model, the relation between the cell voltage, the cathode overpotential and the ohmic resistance is expressed by a polarization equation obtained through the application of Kirchhoff's voltage law

$$E = E_{OCP} + \eta_c - j(y) R^M \tag{6.8}$$

The relation between the total current I obtained or imposed to the cell, and the local current densities is expressed by the integration of the latter along the catalyst area:

$$I = W^{CH} \int_0^{L^{CH}} j(y) \, \mathrm{d}y. \tag{6.9}$$

In the Equation 6.10, W^{CH} is the width of the channel while L^{CH} its length.

In the figure 6.9, simulated CFRA magnitude and phase Bode plots under galvanostatic conditons are displayed. The values of the parameters changed with respect ot the other simulations are listed in the Table 6.2. As seen in the experimental spectra (Figures 6.3 and 6.5), the value of the magnitude decreases going from lower to higher frequencies until a certain critical frequency $f_{c,1} = 1.9 Hz$ where it approaches zero. Then, the value starts to oscillate achieving periodically a minimum value at frequencies which are multiple of the critical value (for example $f_{c,2} = 2f_{c,1} = 3.8 Hz$ in the Figure 6.9). This trend was also observed by Fahydi [197]. In the same frequency range, the phase angle also oscillates. This pattern could explain the scattering observed in the phase plot in the Figures 6.5b, d at higher frequencies and the oscillations occurring at lower frequencies in the CFRA phase spectra obtained by water pressure perrturbation (Figure 6.6b, e).

Quantity	Value	Dimension
H^{CH}	26.2×10^{-3}	m
L^{CH}	6.2×10^{-2}	m
$P_{O_2,in}$	21×10^3	Pa
R^M	2×10^{-2}	Ω
W^{CH}	4×10^{-2}	m

Table 6.2: Values of the parameters used for the simulation of the simplified channel model.

In the Figure 6.10, simulated pressure oxygen inputs and related voltage outputs at three different frequencies indicated in the Figure 6.9 are displayed. Specifically, a low frequency value (f_1), the critical frequency ($f_{c,1}$) and the one at which the first maximum of the oscillation is observed are considered. As expected, while the amplitudes of the input are kept constant for each frequency, the one of the voltage output present a minimum at the critical frequency where the oscillations are almost close to disappear or negligible compared to the other case.

The reason of this trend can be explained through the Figure 6.11 where the steady state profile along the axial channel coordinate together with the quasi-steady state
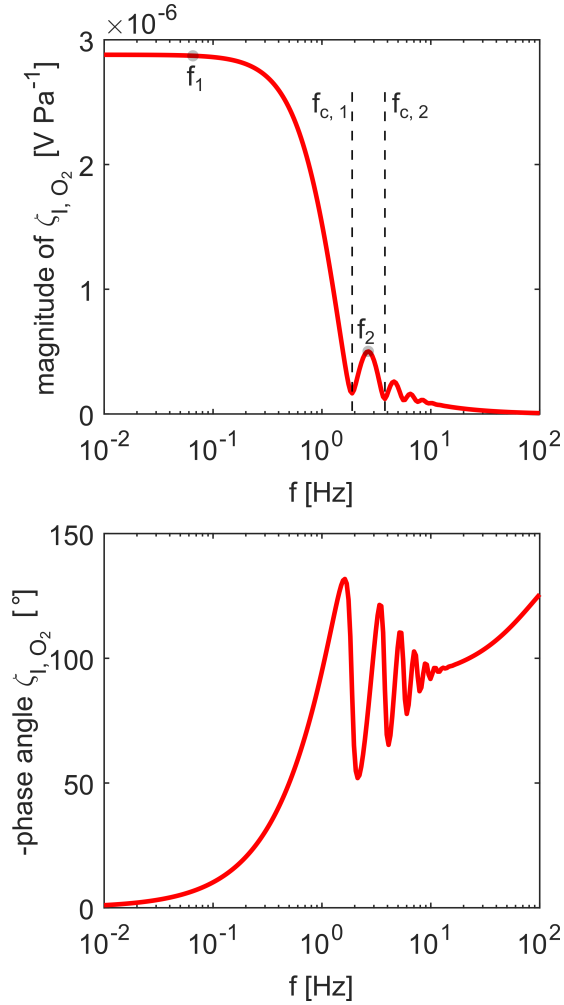
Figure 6.9: Simulated galvanostatic CFRA spectra obtained by oxygen perturbations using the simplified cathode channel model. Steady state current at 300 mA cm^{-2}: (a) magnitude Bode plot, (b) phase Bode plot.

profile during CFRA experiments at the critical frequency of oxygen partial pressure (Figure 6.11a) and cathode overpotential (Figure 6.11b) are displayed. As it can be seen, at this frequency, a complete period of the oxygen pressure perturbation lies along the spatial coordinate. Under such condition, the spatial positive and negative variation of the cathode overpotential compensate each other giving an average change of the overpotential $\overline{\eta_c}$ approximating zero. The situation depicted in the Figure 6.11b can be expressed through the following equation

$$\overline{\eta_c} = \frac{1}{L} \int_0^L \left(\eta_{c,ss} - \eta\left(y\right) \right) \, \mathrm{d}y \approx 0. \tag{6.10}$$

For the reason explained above, the global voltage response to the periodic pressure excitation at this frequency present a low amplitude. Moreover, it can be deduced
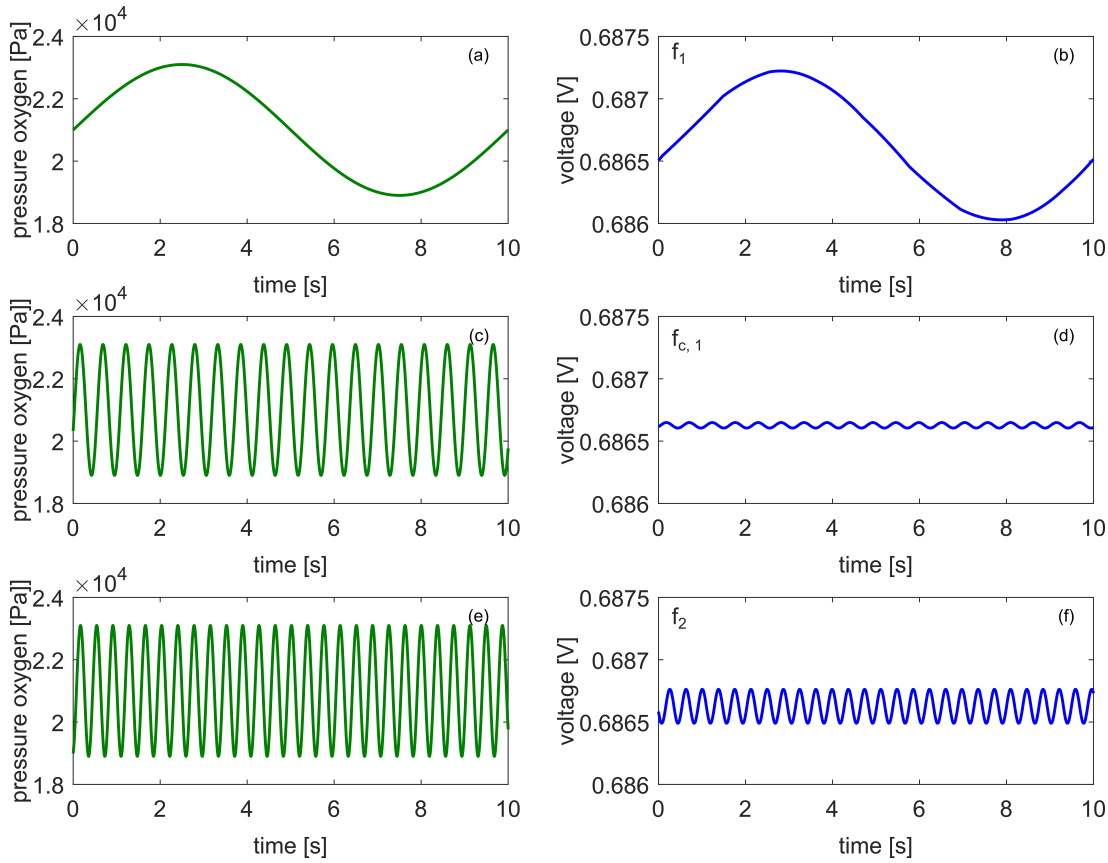
Figure 6.10: Periodic oxygen pressure inputs and voltage outputs simulated by the simplified cathode channel model at different frequencies: (a)-(b) 0.1 Hz, (c)-(d) 1.9 Hz (critical frequency), (e)-(f) 2.8 Hz.

from this theoretical analysis that the value of the critic frequency is dependent on the residence time of the gas and on the inhomogeneities of the voltage or current profile along the channel. Therefore, it be used as value to evaluate these parameters.

The results of these simulations show that the not predicted patterns from the model described in the Chapter 4 and observed in the experimental CFRA spectra could be due to phenomena of resonance. These effects are registered at lower frequencies for the CFRA by water partial pressure input because phenomena slower than the oxygen transport in the channel, like the water sorption in Nafion, could be involved.

6.2 Comparison of parameter estimation by different FRA techniques

The model simulations fitted to the experimental spectra do not reproduce all the data at different steady current densities with the same accuracy by the same set of estimated
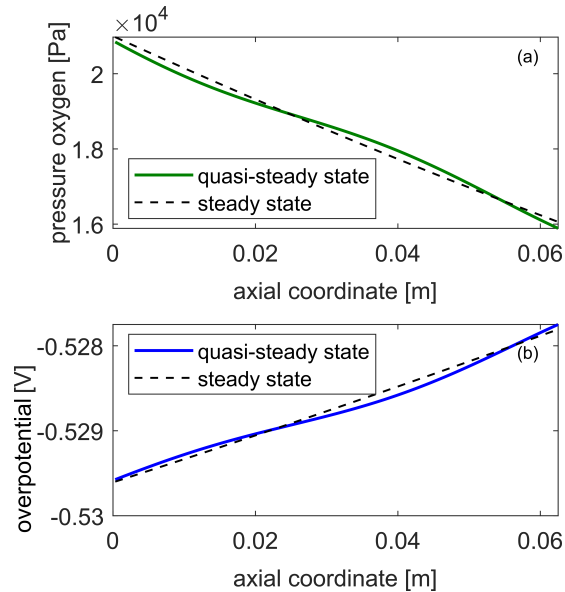
Figure 6.11: Simulated oxygen pressure and cathode overpotential profiles along the channel coordinate at the critical frequencies. The simplified cathode channel model was used for the simulations.

parameters. The main reason can be attributed to the assumptions made in the model which does not include effects of parameters change with operating conditions.

First of all, the rate determining step of the ORR changes by decreasing the voltage of the fuel cell implying a variation of the transfer coefficient from 1 to 0.5 [135]. The simplified one step mechanism used in the model does not predict such a trend, providing an unique value for all the experimental conditions. For this reason, an inaccurate estimation of the kinetic resistance could be performed.

Then, the neglect of the liquid water formation inside the catalyst layer and GDL does not allow to account the increase of the mass transport resistance due to the consequent reduction of the effective porosity along with the steady state current density. This assumption can lead to an underestimation of the concentration polarization at high current densities and to an overestimation at lower ones.

Moreover, the constitutive equations used to express the dependence of the electroosmotic drag coefficient and the diffusivity of water in Nafion on the water content in the membrane could be inadequate to describe correctly their change in all the operating conditions considered. In this regard, it must be also mentioned that equations capable to universally predict the value of these two parameters along all the relative humidity conditions at the membrane interfaces have not been formulated yet [194, 195].

However, the change of these parameters and the related power losses can also be meaningfully evaluated by fitting the model to the single spectra at each steady state. By this way, the trend of the values of the obtained parameters along with the differ-

ent experimental conditions could be monitored and related to specific faulty states allowing the use of the the spectra for diagnosis purposes. As already discussed in the Section 2.2.1, this approach has been used in many onnboard model based diagnostic methodologies recently developed for PEMFCs.

In the Section 4.3.2, a mathematical framework to evaluate the identifiability of parameters and compare the reliability of their estimation using the different FRA techniques was introduced. The results obtained from this analysis are dependent on the frequency range in which the spectra is determined and the number of the measured points per decade. As these settings are different in the experiments from the one considered in the Section4.3.2, in the following, the identifiability analysis is repeated considering the same parameters for these different conditions. Then, the parameters are estimated through model fitting of the spectra of each FRA transfer functions at different steady state. The plausibility of the trend of the parameter changes obtained over the different conditions is analyzed. According to these results, the most suitable FRA technique to be used as online diagnostic tool for PEMFCs is determined.

6.2.1   Comparison of parameter identifiability

The spectra are measured in the constrained frequency region between 8 mHz and 1 Hz collecting 8 points per decade. Considering these specifications, mean square sensitivities of each simulated transfer function at any operating conditions are listed in the Table 6.3. The trends of the values obtained are similar to the ones found in the Chapter 4. The cathode transfer coefficient turns out to have also in this case a high influence on all the FRA spectra, as well as the porosity of the GDL relative to oxygen transport. Moreover, the sensitivity to parameters related to the transport of water (GDL porosity relative to oxygen transport, intrinsic water diffusivity in Nafion, electroosmotic drag constant) is significant only for CFRAs involving water pressure inputs, as previously verified.

On the contrary, some differences from the previous calculations are observed about the collinearity index (Table 6.4). The first consideration to point out concerns the extremely high values of the index related the galvanostatic CFRA by oxygen pressure at all the steady state conditions and for all the parameters subsets. Because of this high correlation implying an undetermined number of parameters sets fitting the data, this FRA methodology cannot give reliable diagnostic information based on a single spectra at this frequency range.

Furthermore, it is noticeable that the value of the collinearity index of the subset 1 containing the charge transfer coefficient and the GDL porosity relative to the oxygen transport largely overcomes the fixed threshold in all the the frequency response methodologies and operating conditions except for the EIS at 100 mA cm^{-2}. Therefore, these two parameters result to be highly correlated and cannot be estimated together by fitting the model to the experimental spectra collected. One of them must be guessed or determined by other experimental techniques and, then, fixed in order to obtain a reliable estimation of the other parameters.

105

Current	Technique	$\delta^{msqr}_{\alpha_C}$	$\delta^{msqr}_{\varepsilon_{O_2}}$	$\delta^{msqr}_{\varepsilon_{H_2O}}$	$\delta^{msqr}_{D^M_{H_2O}}$	$\delta^{msqr}_{K_{H+}}$
100 mA cm^{-2}	EIS	0.58	0.11	0.03	0.004	0.003
	CFRA(O$_2$) vol.	0.4	0.08	0.02	0.01	0.01
	CFRA(O$_2$) gal.	0.99	0.19	0.007	0.008	0.007
	CFRA(H$_2$O) vol.	0.28	0.06	0.51	0.08	0.06
	CFRA(H$_2$O) gal.	0.74	0.14	0.54	0.08	0.07
200 mA cm^{-2}	EIS	0.56	0.34	0.06	0.01	0.01
	CFRA(O$_2$) vol.	0.41	0.26	0.04	0.03	0.02
	CFRA(O$_2$) gal.	0.99	0.62	0.02	0.02	0.01
	CFRA(H$_2$O) vol.	0.32	0.21	0.56	0.13	0.05
	CFRA(H$_2$O) gal.	0.75	0.48	0.66	0.16	0.04
300 mA cm^{-2}	EIS	0.71	1.73	0.12	0.02	0.02
	CFRA(O$_2$) vol.	0.26	0.64	0.03	0.02	0.02
	CFRA(O$_2$) gal.	0.99	2.41	0.1	0.05	0.04
	CFRA(H$_2$O) vol.	0.23	0.61	0.61	0.15	0.07
	CFRA(H$_2$O) gal.	0.85	2.15	0.74	0.13	0.07

Table 6.3: Mean square sensitivities of the different transfer functions at thre steady state currents.

Current	Subset number	Parameters	EIS	CFRA(O$_2$) gal.	CFRA(O$_2$) vol.	CFRA(H$_2$O) gal.	CFRA(H$_2$O) vol.
100 mA cm^{-2}	1	$\alpha_c, \varepsilon_{O_2}$	12.44	61.1	78.37	42.5	27.01
	2	$D^M_{H_2O}, \xi_{el}$	12.76	507.26	12.03	1.39	1.22
	3	$\varepsilon_{O_2}, \varepsilon_{H_2O}, D^M_{H_2O}$	7.88	97.96	113.39	4.74	1.53
	4	$\varepsilon_{O_2}, \varepsilon_{H_2O}, K_{H+}$	7.93	95.33	11.57	3.9	3.66
	5	$\varepsilon_{O_2}, D^M_{H_2O}, K_{H+}$	23.23	582.04	12.72	2.7	1.41
	6	$\varepsilon_{H_2O}, D^M_{H_2O}, K_{H+}$	18.75	517.9	13.48	2.04	1.64
	7	$\varepsilon_{O_2}, \varepsilon_{H_2O}, D^M_{H_2O}, K_{H+}$	23.93	589.7	20	4.81	5.57
200 mA cm^{-2}	1	$\alpha_c, \varepsilon_{O_2}$	19.48	171.94	279.61	120.8	81.47
	2	D_λ, K_{H+}	8.41	668.24	4.81	1.03	1.86
	3	$\varepsilon_{O_2}, \varepsilon_{H_2O}, D^M_{H_2O}$	9.83	464.6	11.6	3.82	2.36
	4	$\varepsilon_{O_2}, \varepsilon_{H_2O}, K_{H+}$	14.63	543.1	9.57	5.41	1.53
	5	$\varepsilon_{O_2}, D^M_{H_2O}, K_{H+}$	15.93	1027.6	6.77	1.62	2.39
	6	$\varepsilon_{H_2O}, D^M_{H_2O}, K_{H+}$	10.61	738.4	7.38	1.98	1.98
	7	$\varepsilon_{O_2}, \varepsilon_{H_2O}, D^M_{H_2O}, K_{H+}$	20.36	1102.6	14.41	5.43	8.37
300 mA cm^{-2}	1	$\alpha_c, \varepsilon_{O_2}$	40.34	447.1	297.21	400.73	249.96
	2	$D^M_{H_2O}, K_{H+}$	15.92	984	7.5	7.5	1.33
	3	$\varepsilon_{O_2}, \varepsilon_{H_2O}, D^M_{H_2O}$	22.21	1943.9	17.9	3.71	195
	4	$\varepsilon_{O_2}, \varepsilon_{H_2O}, K_{H+}$	37.88	3893.4	15.5	9.43	2.62
	5	$\varepsilon_{O_2}, D^M_{H_2O}, K_{H+}$	23.4	2444.8	10.3	3.62	1.7
	6	$\varepsilon_{H_2O}, D^M_{H_2O}, K_{H+}$	18.35	4259.3	10.6	10.06	13.89
	7	$\varepsilon_{O_2}, \varepsilon_{H_2O}, D^M_{H_2O}, K_{H+}$	37.99	4419.6	17.9	10.1	15

Table 6.4: Collinearity index of EIS and CFRA transfer function at three different current densities.

Additionally, voltastatic CFRA by oxygen pressure and the ones performed by water inputs are the only techniques to present a low correlation index for the subset 7 which contains all the transport parameter fitted.

106

Therefore, to summarise, from the analysis of the collinearity index reported above, two main considerations can be deduced about the reliability of the parameter estimation. First, charge transfer coefficient and oxygen diffusivity cannot be determined together by the fitting the collected experimental spectra at one steady state by none of the methodologies examined. This was expected, since both the kinetic transfer and diffusivity influence directly the faradaic efficiency of the ORR reaction (see Equation 4.18). The former changing the free energy required to make the electron transfer occurring at the interface, while the latter changing the oxygen pressure at the catalyst surface. For this reason, their effects are always coupled and impossible to distinguish in one set of measurements in the frequency range in which the experiments were performed. Secondly, voltastatic and galvanostatic CFRA by water pressure are the only experimental techniques to present a tolerable correlation index between the transport parameters which are grouped in the subset 7. Therefore, the model fitting of the spectra obtained through these methodologies should give the most reliable results which could be used to get information on the PEMFC performance losses.

In order to further verify the findings of the identifiability analysis and investigate the plausibility of the parameters obtained, all the spectra were fitted by the model keeping constant the cathode transfer coefficient α_c. Since the IR free steady state voltages of the performed experiments lie between 762 mV and 659 mV, the value of this parameter was fixed to 0.5 as suggested by several studies [135]. The employed fitting algorithm was run four times in order to determine if the the stable solution is achieved. In case of high correlation, the optimal set of parameters obtained by this process changes after any run showing the impossibility to converge to a unique solution or not possible convergence at all. It must be also pointed out that another reason hindering the achievement of a unique solution is the presence of local optimal points close to the global one which the number is independent on the parameters correlation.

Different set of parameters for each run were obtained for the classic EIS, galvanostatic and voltastatic CFRA by oxygen pressure input, and voltastatic CFRA by water pressure. For the first three FRA techniques, this was expected due the high correlation index determined for the set of the fitted parameters not finding a converging solution. Regarding the latter, the fail to reach a stable solution is surprising and could be due to the presence of different local optimal point minimizing the least square objective function. A single optimal set of parameters was obtained after the first algorithm run by the fitting of the galvanostatic CFRA performed by water perturbations, fulfilling the expectation indicated by a low correlation index. Therefore, only the parameters estimated by this technique can be considered reliable.

In the Table 6.5, the parameters estimated after the fourth run of the fitting optimization algorithm are displayed for any spectra. An analysis of the physical plausibility of the results obtained confirms the previous conclusions. Basically, except for the case of the galvanostatic CFRA performed by using water partial pressure perturbations, the trend of the parameters along the different steady states is inconsistent with the expected physicochemical behavior of a PEMFC. As example, the effective

porosity ε_{O_2} related to the oxygen diffusion estimated by the classic EIS increase its value from 0,03 to 0,34 respectively at 100 mA cm^{-2} and 200 mA cm^{-2}, and then decreases again to 0,032 at 300 mA cm^{-2}. This trend is meaningless, since a monotone decrease of effective porosity should be verified as consequence of the increase of the mass transport. Similar situation is observed through the fitting of the spectra of the other FRA techniques except for galvanostatic CFRA by water input for which the value of ε_{O_2} shows the expected descending trend.

Current	Technique	ε_{O_2}	ε_{H_2O}	$D^M_{H_2O}$	K_{H^+}
	EIS	0,03	1	0,1	1,85
	CFRA(O_2) pot	0.59	0.41	0.16	0.13
100 mA cm^{-2}	CFRA(O_2) gal	0.69	0.03	0.1	0.91
	CFRA(H_2O) pot	0.04	0.042	0.99	1.6
	CFRA(H_2O) gal	0.15	0.78	0.6	2.45
	EIS	0.34	0.06	0.01	0.01
	CFRA(O_2) vol.	0.49	0.61	0.01	0.01
200 mA cm^{-2}	CFRA(O_2) gal.	0.8	0.3	0.11	2.98
	CFRA(H_2O) vol.	0.38	0.16	0.87	1.03
	CFRA(H_2O) gal.	0.06	1	1.32	2.3
	EIS	0.032	0.48	1	1
	CFRA(O_2) vol.	0.42	0.41	0.96	0.69
300 mA cm^{-2}	CFRA(O_2) gal.	0.065	0.48	1.7	0.66
	CFRA(H_2O) vol.	0.57	0.062	1.1	1.29
	CFRA(H_2O) pot.	0.045	0.97	2.97	2.42

Table 6.5: Parameters estimated by fitting of the experimetnal magnitude Bode plots.

Discrepancies are verified in the estimated values of the Nafion intrinsic diffusivity $D^M_{H_2O}$ as well. It is noticeable that the fitted value by all the FRA techniques excluding the galvanostatic CFRA by water pressure displays his lowest value at mA cm^{-2} suggesting the presence of a minimum. A higher steady state current implies a larger water content in the membrane which results in a monotone increase of the water diffusivity in Nafion along with this variable till the achievement of a plateau [177, 194]. Therefore, these estimations cannot be considered realistic. On the other hand, the increasing trend of the intrinsic Nafion diffusivity obtained by the fitting of galvanostatic spectra of CFRA by water perturbations reproduce the expected scenario.

The estimated electroosmotic drag constant is expected to be unchanged along the steady state current as well established in the literature [3, 194]. Once again, this condition is only fulfilled by the fitting of the of the spectra obtained from the galvanostatic CFRA by water perturbation which the value of K_{H^+} slightly changes from an average one of 2,37. Then, the parameters estimated through this FRA technique using the formulated model are characterized not only by good identifiability parameters, but also from a physical plausibility. For this reason, it can be considered suitable for the

employment as onboard diagnostic tool among the others.
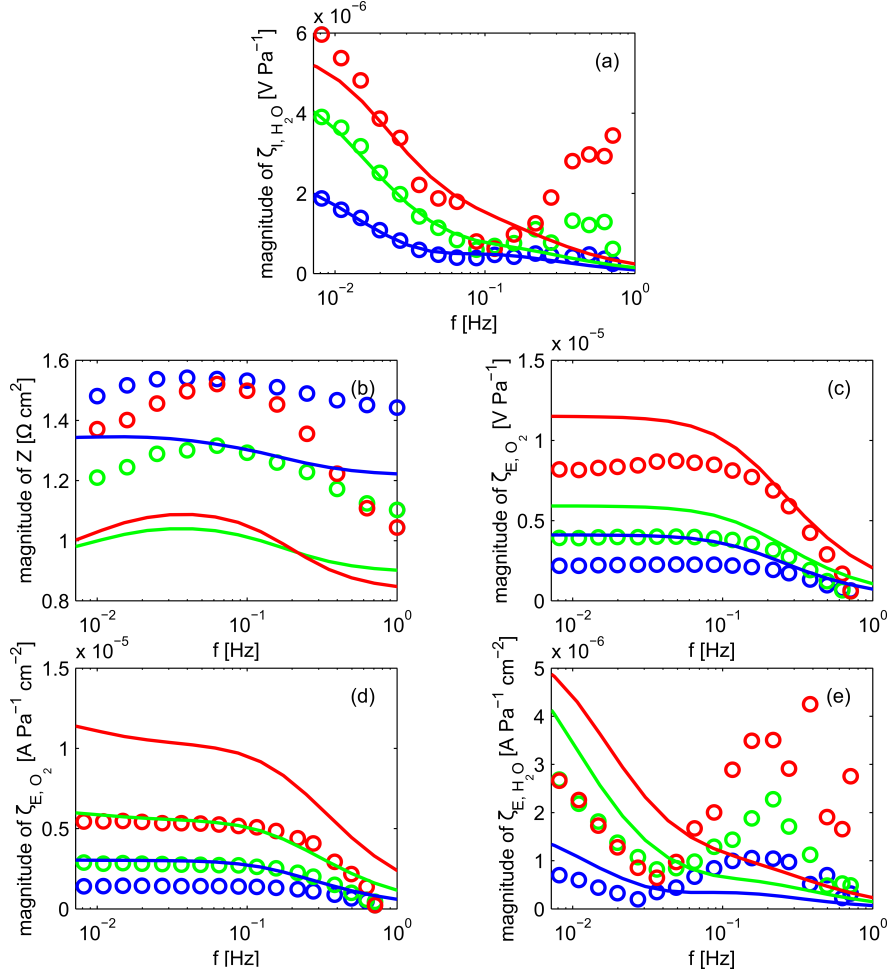
Figure 6.12: Experimental magnitude Bode plots (circle markers) together with simulated ones (solid lines) using the parameter set obtained by fitting of the galvanostatic CFRA performed by water pressure perturbations: (a) galvanostatic CFRA by water pressure perturbations, (b) impedance, (c) galvanostatic CFRA by oxygen pressure perturbations, (d) voltastatic CFRA by oxygen pressure perturbations, (e) voltastatic CFRA by water pressure perturbations.

In the Figure 6.12, it has been been showed the capability of the parameters extrapolated from the model fitting of the spectra of CFRA by water inputs to match the patterns observed by the other FRA methodologies. Simulated magnitude Bode plots using the fitted set of transport parameters and experimental ones are displayed for comparison purpose. The simulations which replicate the spectra of CFRA by water perturbations with a good accuracy, quantitatively overestimate the magnitude plots of all the other CFRA techniques, while the ones of the EIS are underestimated. The reason of these discrepancies can be probably attributed to the effects of not accounted

phenomena in the model. This can have a different impact on the response depending on the input considered. Nevertheless, it is remarkable that a good qualitative agreement is verified.

6.3 Conclusion

Using the setup and the experimental procedure described in the Chapter 5, CFRA spectra were experimentally determined at different experimental conditions. The obtained CFRA spectra obtained by using oxygen pressure inputs reflected all the features observed in the theoretical ones shown in the Chapter 4. Therefore, the capability to detect selectively the contribution of the mass transport in the channel was confirmed. The spectra related to the CFRA by water perturbations replicated the simulated ones only at lower frequencies, while they showed some patterns at higher ones which were not predicted. These differences were associated to phenomena not accounted in the model. For example, the transport of the liquid water in the GDL produced on the cathode could originate such a path. On the other hand, phenomena of resonance could give the same response on the spectra. Signs of resonances were observed in the CFRA spectra obtained using both the partial pressures as input. They were assumed to due the distribution of the effect of the pressure waves along the channel. In order to verify this hypothesis, a simplified model of the cathode channel accounting for spatial variations along the axes was developed. The simulations reproduced the ambiguous patterns at higher frequencies confirming the possibility of the influence of resonance processes.

The quality of the parameter estimation performed by fitting a single experimental CFRA and EIS spectra with the model was evaluated in order to compare the results obtained through the different FRA techniques. The main purpose of this analysis was about evaluating which techniques were the most suitable to be applied in model based onboard diagnostic tool. The analysis was based on the concept of mean square sensitivity and coillinearity coefficient. It was found that transfer coefficient and oxygen effective diffusivity cannot be estimated correctly together considering the frequency range and the data points set because extremely correlated. Among all techniques, CFRA performed by water perturbation showed the best reliability of parameters estimated.

Chapter 7

Coupled CFRA transfer functions

In this chapter, the concept of coupled CFRA transfer function is introduced and its use as diagnostic tool is discussed. First, the mathematical definition and the experimental procedure to measure the novel transfer function are respectively described in the Sections 7.1 and 7.2. Then, experimental and theoretical coupled CFRA spectra are compared to identify the phenomena related to the patterns observed (Section 7.2). Finally, the capabilities to isolate faulty conditions due to reactants starvation is demonstrated (Section 7.2.3).

7.1 Definition of coupled CFRA transfer function

As in the case of the normal CFRA, the coupled CFRA transfer function is based on the perturbation of the cell through a simultaneous change of oxygen and water partial pressure. As seen in the Chapter 5, this double perturbation is produced by the periodic addiction of a small flow of dried oxygen to the cathode cell feed at different time intervals. In this way, not only a periodic variation of the oxygen pressure is obtained, but a variation of water vapour pressure as well. Basically, an increment of the oxygen partial pressure excites a complementary decrement of the partial pressure of water and viceversa, resulting in a simultaneous periodic stimulation where the two pressure inputs (O_2 and H_2O) are in antiphase. The relation between the inputs and the resulting electrical output of the cell is described in terms of frequency response transfer function by the equation 5.3. Dividing this equation by the measured variation of oxygen at different frequencies $\tilde{P}_{O_2}(i\omega)$, the following coupled CFRA transfer functions under galvanostatic $\zeta_{I,O_2}\prime$ and voltastatic conditions $\zeta_{E,O_2}\prime$ are determined:

$$\zeta_{I,O_2}\prime(i\omega) = \frac{\tilde{I}(i\omega)}{\tilde{P}_{O_2}(i\omega)} = \zeta_{I,O_2}(i\omega) + \beta\zeta_{I,H_2O}(i\omega) \tag{7.1}$$

$$\zeta_{E,O_2}\prime(i\omega) = \frac{\tilde{E}(i\omega)}{\tilde{P}_{O_2}(i\omega)} = \zeta_{E,O_2}(i\omega) + \beta\zeta_{E,H_2O}(i\omega) \tag{7.2}$$

Basically, a linear combination of the two "pure" CFRA transfer functions is obtained. The variable $\beta = \frac{\tilde{P}_{H_2O}(i\omega)}{\tilde{P}_{O_2}(i\omega)}$ quantifies the fraction of the CFRA transfer function obtained by water pressure input overlapping with the one determined by using oxygen pressure perturbations. The value of β depends on the specification of the main flow and it is assumed to be constant over all the frequencies. Since $\tilde{P}_{O_2}(i\omega)$ and $\tilde{P}_{H_2O}(i\omega)$ have opposite signs, the value of β is negative and the contribution of the CFRA transfer function by water is subtractive. In case of the use of additional flow of nitrogen to create the pressure perturbations, the value of β is positive since the inputs are in phase (see Section 5.2.1). However, this is not considered here and we restrict our study only to oxygen based coupled CFRA transfer function.

7.2 Experimental and theoretical study

7.2.1 Experimental operating conditions

The setup described in the Chapter 5 was used to perform the experiments shown in the following. Additionally, the same spectral analysis procedure and protocol were used to determine the inputs and outputs in frequency domain.

A feed of pure hydrogen with a flow rate fixed at 800 ml/min was supplied to the anode, while the cathode was fed with 250 ml/min of nitrogen and oxygen. Dew point temperatures of 60 °C and 40 °C were respectively set for the cathode and anode feed stream. These conditions of wet cathode/almost dry anode were chosen to induce a significant backwards permeation of water in the membrane. The fuel cell was already described in Section 5.1.2. The MEA used in these experiments was prepared in house using Nafion 117 membrane and catalyst ink containing platinum black (Alpha Aesar).

7.2.2 Coupled CFRA spectra

Experimental voltastatic and galvanostatic coupled CFRA spectra recorded at three different steady states are displayed in the Figure 7.1. As can be seen, at frequency higher than 0.1 Hz, the magnitude of CFRA (Figure 7.1a-b) presents the same features seen in the normal CFRA in both the electric controls applied. A steep increment up to the achievement of a plateau is observed, indicating the dynamics of the gas transport in the cathode. Also in this case, the value at the plateau increases along with the steady state current suggesting a proportional relation with the concentration polarization. Moreover, the value of the spectra at the highest frequency detected (f≈ 1 Hz) results to be almost independent on the steady state conditions and approaching the valuo of zero. This behaviour, observed already in the not coupled oxygen CFRA spectra, is due to resonance phenomena caused by the spatial distribution of the oxygen pressure fluctuation along the channel which annul their concentration polarization contribution to the response at a certain frequency (see Section 6.1.6). The time constant of the gas transport in the PEMFC channel can be estimated from the minimum
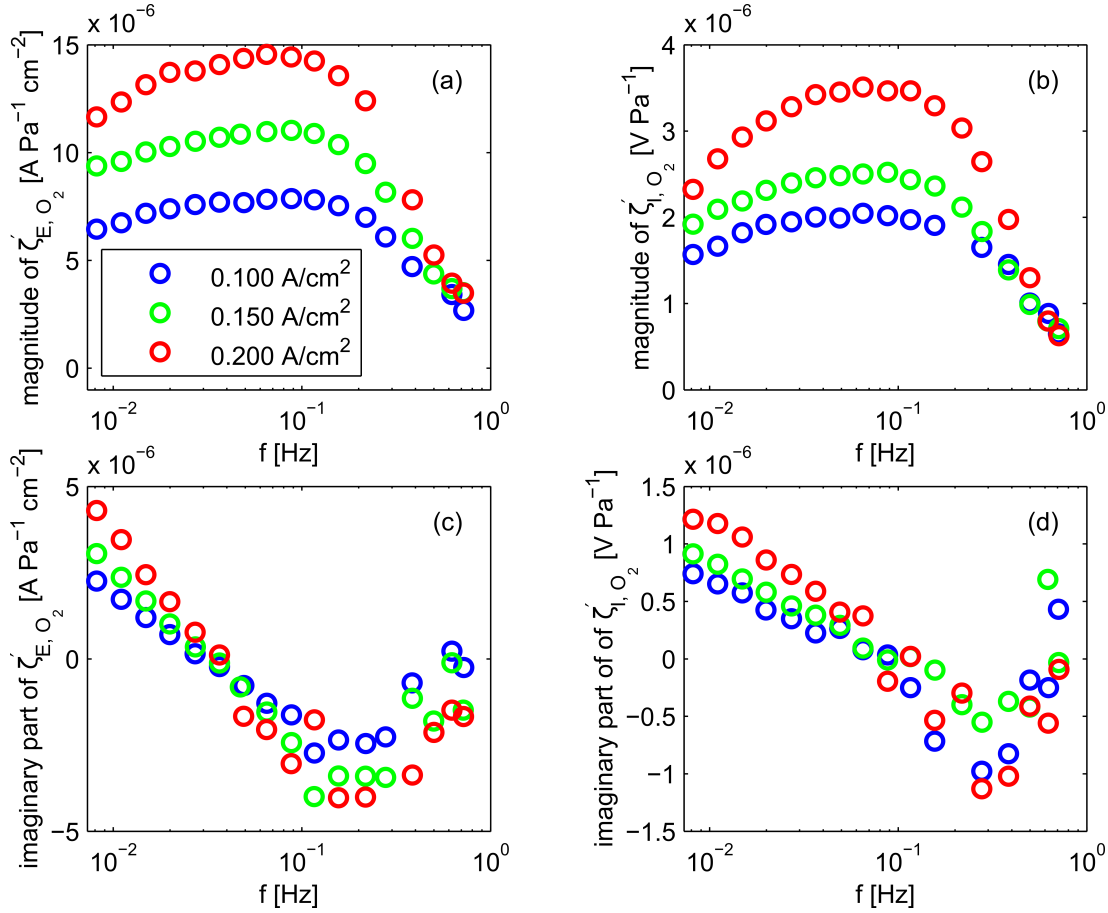
Figure 7.1: Magnitude (top) and imaginary part (bottom) spectra of voltastic CFRA (a, c) and galvanostatic CFRA (b, d). β=0,45.

points of the imaginary part plots of the coupled transfer function (Figure 7.1c-d). At lower frequencies, differencies are verified between the coupled and the pure CFRA spectra As seen in the figure 6.3, an increase of the magnitude is observed at such frequencies under voltastic conditions, while a constant value is kept under galvanostatic conditions. On the contrary, both coupled CFRA spectra present a decrease for both the cases which is slighter for the voltastic control and more pronunced in the galvanostatic one. This discrepancies are mainly assigned to the subtractive contribution of the CFRA transfer function by water pressure input which is more prominent in the low frequency range. As result of the water perturbation during two simulataneous inputs CFRA experiments, the amplitude of the current and voltage outputs change due to membrane hydration and consequent lowering of the ohmic resistance.. This contribution is mostly contained in the pure water transfer function ζ_{H_2O} which is subtractive in the coupled CFRA and, therefore, a decrement is obtained in the magnitude (see Equations 7.1 and 7.2).

This hypothesis is confirmed in the simulated spectra through the developed PEMFC

model shown in the Figure 7.2. Specifically, magnitudes of CFRA oxygen transfer function (Figures 7.2 a-b) are compared to the coupled ones (Figures 7.2 c-d) which were obtained by simulating a simultaneous oxygen and water perturbation in antiphase and by applying the Equations 7.1 and 7.2. As expected, the oxygen CFRA transfer function under voltastatic condition shows an increment at lower frequencies due the hydration of membrane, while the one at galvanostatic control is contant due to the constant current production. On the contrary, the simulated coupled CFRA transfer functions are characterized by a decrease like the experimental ones due to the subtractive contribution of CFRA transfer function by water pressure input.
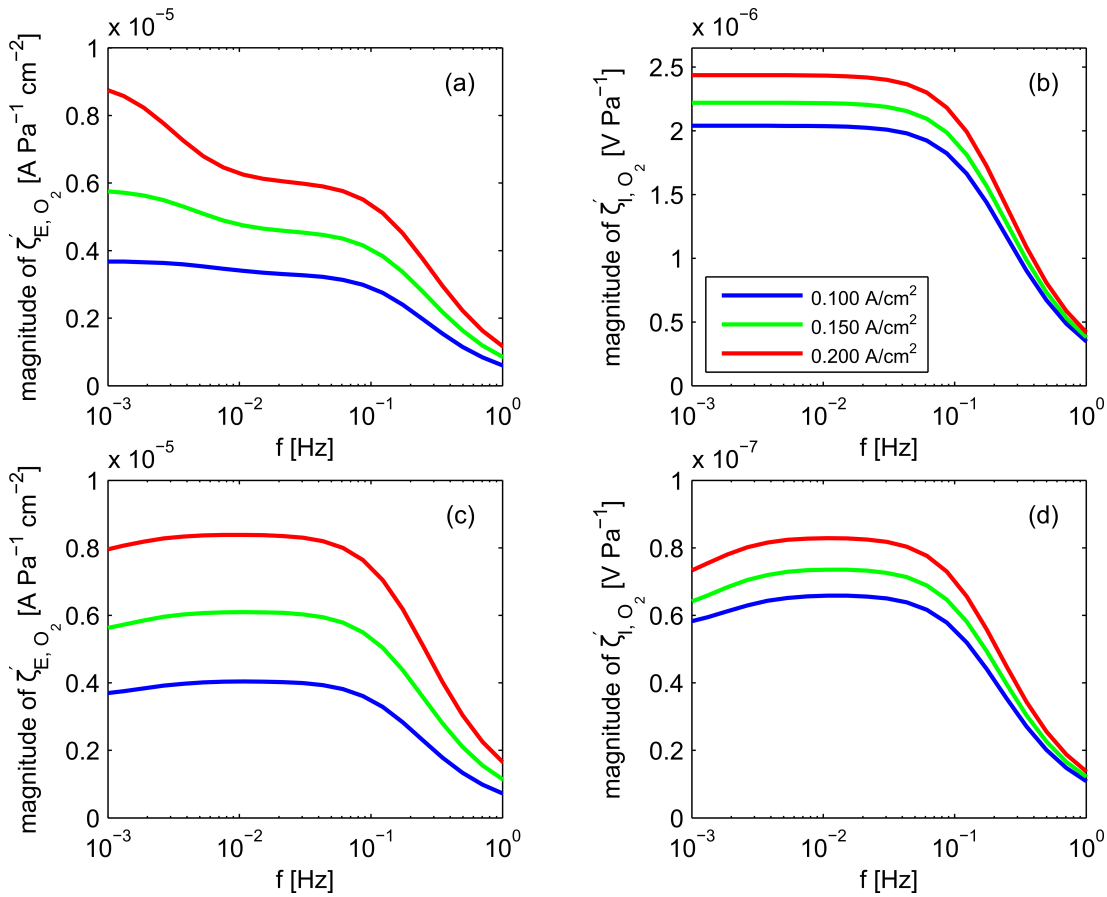
Figure 7.2: Simulated magnitude plots of the CFRA transfer function obtained by oxygen pressure perturbations: a) voltastatic CFRA transfer function, b) galvanostatic CFRA transfer function, c) voltastatic coupled CFRA transfer function, d) galvanostatic coupled CFRA transfer function.

7.2.3 Coupled transfer function analysis for diagnosis of reactant starvation

As mentioned previously, the value of β, which quantifies the contribution of the water transfer function to the coupled one, changes with the specification of the main feed. This feature was found to be helpful for diagnosis of reactant starvation, especially to identify low humidification of the feed.

Voltastatic CFRA and EIS spectra were recorded experimentally at a steady state current density of 100 mA cm^{-2} using two different experimental conditions with asymmetric dew point temperature values of the feed, named a dry anode/wet cathode configuration, and a dry anode/dry cathode configuration. In the first case, the fraction of the CFRA transfer function by water input β is 0.45, while the second case is characterized by a lower value of β equal to 0.15. Unlike EIS spectra (Figure 7.3a) which cannot differentiate between two cathode states (in both cases, strong membrane hydration results in lowering the EIS magnitude at low frequencies), the voltastatic CFRA method shows a qualitative difference of the magnitude spectra at low frequencies. Namely, for the voltastatic CFRA, an increment is observed with the dry anode/dry cathode configuration, while a decrement of the magnitude is obtained with the dry anode/wet cathode configuration (Figure 7.3a). This is due to the fact that the contribution of the transfer function by water pressure input is smaller at lower β values and has a minimized impact on the increment of the oxygen transfer function due to membrane hydration registered at low frequancies in voltastatic control. This diagram demonstrates that coupled CFRA under voltastatic control can be used as complementary technique to the classic EIS for identification of dehydrated faulty condition due to malfunctioning of the humidification system of the cathode of PEMFC. Therefore, this method can be considered suitable for implementation of FDI diagnostic algorithms to isolate reactants starvation problems.

7.2.4 Conclusions

The concept of coupled CFRA transfer function was defined and an experimental procedure for its measurement described. Experimental coupled cFRA spectra results to be affected by oxygen transport in the channel and water sorption of water in the membrane under both galvanostatic and voltastatic control. The latter dynamics is observed through a lowering of the magnitude at low frequencies. The theoretical simulations showed that such a decrease is due to the subtractive contribution of a fraction β of the CFRA transfer function obtained by water pressure perturbations. Finally, it was verified that coupled CFRA under voltastatic control can be used as a complementary technique to the classic EIS for isolation of dehydration faulty conditions due to malfunctioning of the humidification system of the PEMFC system.
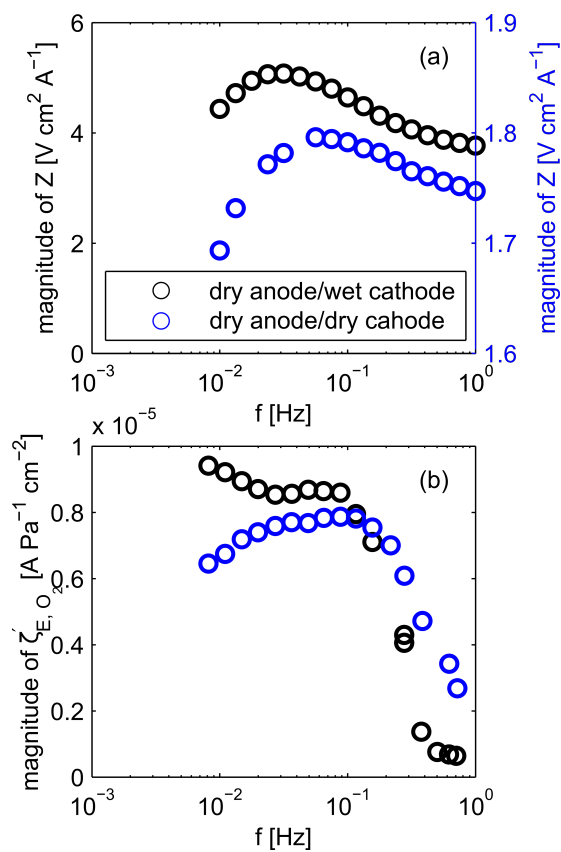
Figure 7.3: Magnitude spectra of EIS (a) and of voltastatic coupled CFRA (b) at a steady state current of $100 \, \text{mA} \, \text{cm}^{-2}$ for dry anode/wet cathode (dew point temperature anode and cathode feed respectively $40 \, ^\circ\text{C}$ and $60 \, ^\circ\text{C}$) and dry anode/dry cathode configurations (dew point temperature of anode and cathode feed at $30 \, ^\circ\text{C}$).

Chapter 8

Summary and Conclusions

In this work, a novel FRA methodology based on concentration inputs alternative to the EIS was developed to study PEMFC dynamics. The aim was to overcome limitations of the EIS with respect to identification and diagnosis of PEMFCs. EIS often fails to separate contributions of different processes due to the coupling in the frequency spectra of the effects of various dynamic phenomena with similar time constants. The proposed technique, named concentration-alternating frequency response analysis (abbreviated CFRA), utilizes periodic inputs of partial pressure of one or more feed components at different frequencies to probe PEMFC dynamics. The electric output obtained, current or voltage, depends on the control regime applied to the fuel cell which would be respectively voltastatic or galvanostatic.

According to the linear system theory, by changing the type of input and/or output, the impact related to a specific dynamic process could be more detectable than others leading to more selective information contained in the transfer function. Following this principle, the primary motivation of using partial pressure inputs was to verify the possibility to separate contributions of overlapping dynamics to PEMFC performance losses which would be coupled to other ones in EIS spectra or not detected at all.

As first step, the capabilities of the CFRA were theoretically investigated through the development of a PEMFC one dimensional dynamic model spatially distributed along the sandwich coordinate including the main physical processes influencing the transient performance, i.e. the charging/discharging of the double layer at the electrode interface acting in parallel to electrochemical reactions, mass transport of gaseous reactants in flow channels and in the porous electrode layers, and water sorption in the Nafion membrane. Prior to the theoretical analysis, the model was successfully validated through comparison to experimental EIS spectra. CFRA experiments involving periodic perturbations of oxygen and water partial pressure sent to the cathode side of the fuel cell under galvanostatic and voltastatic conditions were performed. Therefore, four CFRA transfer functions were determined, i.e. CFRA transfer functions based on oxygen and water pressure inputs for both galvanostatic and voltastatic conditions. The simulations confirmed the capability of CFRA to detect selectively only specific dynamics depending on the input/output configuration used. Transfer functions based

on oxygen pressure inputs under galvanostatic conditions contained only dynamics related to the mass transport of the oxygen inside the channel. On the contrary, the additional dynamics of the water sorption into Nafion membrane were observed in spectra under voltastatic condition. Both the techniques were insensitive to the dynamics of double layer charging and any other phenomenon with time constants lower than the transport of gas in the channel. Additionally, the values of the magnitudes increased with the increase of the mass transport resistance. This trend makes CFRA by oxygen pressure inputs suitable for the evaluation of the impact of cathode flooding.

Transfer functions based on water pressure inputs were mostly influenced by dynamics related to the water sorption in Nafion. Additionally, the proportionality between the water content in the membrane and the magnitude of the transfer functions under galvanostatic conditions makes CFRA by water pressure perturbations an instrument usable to determine conditions of membrane dehydration.

Then, an identifiability analysis regarding the main parameters influencing the performance of the fuel cell was performed. It was demonstrated that CFRA offers more reliable parameter estimation than EIS. In this regard, CFRAs based on water pressure perturbations showed the best performance with respect to parameter estimation. This makes this method especially suitable for application as onboard diagnostic tool.

In order to validate the theoretical findings, an experimental setup capable to produce simultaneous periodic perturbations of oxygen and water was designed. Since the shape of the pressure inputs replace a periodic square wave instead of a sinusoidal, a spectral analysis different from the one applied in the theoretical studies was established which was based on the detection of the fundamental harmonics of the signal. Moreover, it was established an experimental protocol to decouple the contribution to the electric responses of the two simultaneous partial pressure perturbations and determine the CFRA transfer functions.

Using the setup and the established experimental procedure, CFRA spectra were experimentally determined in the same steady state conditions which were considered in the theoretical study. The CFRA spectra obtained by using oxygen pressure inputs reproduced all the features observed in the theoretical ones, confirming the capability to selectively detect the contribution of the mass transport in the channel. On the other hand, the use of water pressure inputs allowed to detect mostly the dynamics of water sorption in Nafion, as also observed in the simulations. However, all the collected experimental CFRA spectra showed patterns at higher frequencies which were not predicted. These features were assumed to be due to phenomena not accounted in the model. For example, the transport of the liquid water produced on the cathode could cause such patterns. On the other hand, phenomenon of resonance due the distribution of the effect of the partial pressure waves along the axial direction in the channel could be also responsible for such features. The latter hypothesis was supported by simulations performed by using a simplified PEMFC channel model distributed along the axial coordinate.

The reliability of the parameters estimation performed by fitting a single CFRA and EIS spectra with the model was compared. The main purpose was to evaluate

which technique was the most suitable to be applied in model based onboard diagnostic tool. For this, the identifiability analysis based on the same concepts used in the theoretical study was repeated considering the setting of the experiments. It was found that charge transfer coefficient and oxygen effective diffusivity cannot be estimated correctly together because they are extremely correlated in all the cases. Moreover, CFRAs performed by water perturbation were confirmed to be most reliable techniques for parameters estimation.

Finally, the concept of coupled transfer function was advanced which is defined as a linear combination of CFRA transfer functions obtained by two simultaneous partial pressure inputs. Due to the different qualitative shape of the spectra depending on the humidification of the fuel cell feed, the coupled transfer functions were found to be helpful in the detection of drying out of the membrane which could be caused by malfunctioning of external humidification systems.

To conclude, CFRA proved to be an experimental technique complementary to EIS capable to discriminate the contributions of gas transport and water sorption in Nafion from the overall performance. These features candidate it as a promising onboard diagnostic tool, overcoming the ambiguities of the EIS. However, some challenges must be solved to make the methodology implementable. First of all, a faster and automated procedure to measure CFRA transfer functions on a large frequency range should be designed. A possibility to perform the measurements faster could be to collect all the harmonics of the square wave input signal. This would allow to determine the value of the transfer function at different frequencies applying a periodic input at a single fundamental frequency and, thus, save time. Additionally, a theoretical investigation employing more detailed two-dimensional model including spatial distribution along the sandwich coordinate and the channel, liquid water transport, ORR mechanism contemplating adsorption/desorption of intermediate steps and a more detailed description of the catalyst layer should be performed to examine further the unexpected patterns observed in the experiments.

Literatur

[1] International Energy Agency. *CO2 emissions from Fuel Combustion-Highlights 2019*.

[2] O. Gröger, H. A. Gasteiger, and J. P. Suchsland. Review—electromobility: Batteries or fuel cells? *Journal of The Electrochemical Society*, 162(14):A2605–A2622, 2015.

[3] M. Eikerling and A. Kulikovsky. *Polymer Electrolyte Fuel Cells: Physical Principle of Materials and Operations*. CRC Press, 1st edition, 2014.

[4] F. Babir. *PEM Fuel Cells: Theory and Practice*. Elsevier, 2nd edition, 2012.

[5] E. Engebretsen, T. J. Mason, P. R. Shearing, G. Hinds, and D. J. L. Brett. Electrochemical pressure impedance spectroscopy applied to the study of polymer electrolyte fuel cells. *Electrochemistry Communications*, 75:60 – 63, 2017.

[6] E. Engebretsen, J. B. Robinson, O. Obeisun, T. Mason, D. Finegan, G. Hinds, P. R. Shearing, and D. J. L. Brett. Electrothermal impedance spectroscopy applied to an open-cathode polymer electrolyte fuel cell. *Journal of Power Sources*, 302:210 – 214, 2016.

[7] O. S. Ijaodola, Z. El-Hassan, E. Ogungbemi, F.N. Khatib, T. Wilberforce, J. Thompson, and A.G. Olabi. Energy efficiency improvements by investigating the water flooding management on proton exchange membrane fuel cell (PEMFC). *Energy*, 179:246 – 267, 2019.

[8] G. Wang, Y. Yu, H. Liu, C. Gong, S. Wen, X. Wang, and Z. Tu. Progress on design and development of polymer electrolyte membrane fuel cell systems for vehicle applications: A review. *Fuel Processing Technology*, 179:203 – 228, 2018.

[9] Q. Li, J. Gong, S. Peng, S. Lu, P. C. Sui, N. Djilali, and Y. Xiang. Theoretical design strategies of bipolar membrane fuel cell with enhanced self-humidification behavior. *Journal of Power Sources*, 307:358 – 367, 2016.

[10] W. Dai, H. Wang, X. Z. Yuan, J. J. Martin, D. Yang, J. Qiao, and J. Ma. A review on water balance in the membrane electrode assembly of proton exchange membrane fuel cells. *International Journal of Hydrogen Energy*, 34(23):9461 – 9478, 2009.

[11] A. Z. Weber and J. Newman. Transport in polymer-electrolyte membranes. *Journal of The Electrochemical Society*, 150(7):A1008, 2003.

[12] A. Z. Weber and J. Newman. Transport in polymer-electrolyte membranes. *Journal of The Electrochemical Society*, 151(2):A311, 2004.

[13] S. Kim and M.M. Mench. Investigation of temperature-driven water transport in polymer electrolyte fuel cell: Thermo-osmosis in membranes. *Journal of Membrane Science*, 328(1):113 – 120, 2009.

[14] R. Zaffou, J. S. Yi, H. Russell Kunz, and J. M. Fenton. Temperature-driven water transport through membrane electrode assembly of proton exchange membrane fuel cells. *Electrochemical and Solid-State Letters*, 9(9):A418, 2006.

[15] T. Ous and C. Arcoumanis. Degradation aspects of water formation and transport in proton exchange membrane fuel cell: A review. *Journal of Power Sources*, 240:558 – 582, 2013.

[16] P. Deevanhxay, T. Sasabe, S. Tsushima, and S. Hirai. Investigation of water accumulation and discharge behaviors with variation of current density in PEMFC by high-resolution soft X-ray radiography. *International Journal of Hydrogen Energy*, 36(17):10901 – 10907, 2011.

[17] H. Li, Y. Tang, Z. Wang, Z. Shi, S. Wu, D. Song, J. Zhang, K. Fatih, J. Zhang, H. Wang, Z. Liu, R. Abouatallah, and A. Mazza. A review of water flooding issues in the proton exchange membrane fuel cell. *Journal of Power Sources*, 178(1):103 – 117, 2008.

[18] U. Pasaogullari and C. Y. Wang. Liquid water transport in gas diffusion layer of polymer electrolyte fuel cells. *Journal of The Electrochemical Society*, 151(3):A399, 2004.

[19] L. Xing, S. Du, R. Chen, M. Mamlouk, and K. Scott. Anode partial flooding modelling of proton exchange membrane fuel cells: Model development and validation. *Energy*, 96:80 – 95, 2016.

[20] J. Park, X. Li, D. Tran, T. Abdel-Baset, D.S. Hussey, D.L. Jacobson, and M. Arif. Neutron imaging investigation of liquid water distribution in and the performance of a PEM fuel cell. *International Journal of Hydrogen Energy*, 33(13):3373 – 3384, 2008.

[21] K. Seidenberger, F. Wilhelm, T. Schmitt, W. Lehnert, and J. Scholta. Estimation of water distribution and degradation mechanisms in polymer electrolyte membrane fuel cell gas diffusion layers using a 3D monte carlo model. *Journal of Power Sources*, 196(12):5317 – 5324, 2011.

[22] H. Li, Y. Tang, Z. Wang, Z. Shi, S. Wu, D. Song, J. Zhang, K. Fatih, J. Zhang, H. Wang, Z. Liu, R. Abouatallah, and A. Mazza. A review of water flooding issues in the proton exchange membrane fuel cell. *Journal of Power Sources*, 178(1):103 – 117, 2008.

[23] S. Ge and C. Y. Wang. Liquid water formation and transport in the PEFC anode. *Journal of The Electrochemical Society*, 154(10):B998, 2007.

[24] N. Holmström, J. Ihonen, A. Lundblad, and G. Lindbergh. The influence of the gas diffusion layer on water management in polymer electrolyte fuel cells. *Fuel Cells*, 7(4):306–313, 2007.

[25] W. R. Baumgartner, P. Parz, S.D. Fraser, E. Wallnoefer, and V. Hacker. Polarization study of a PEMFC with four reference electrodes at hydrogen starvation conditions. *Journal of Power Sources*, 182(2):413 – 421, 2008.

[26] R. Borup, J. Meyers, and B. Pivovar. Scientific aspects of polymer electrolyte fuel cell durability and degradation. *Chemical Reviews*, 107(1):2904 – 3952, 2007.

[27] M. Schulze, N. Wagner, T. Kaz, and K.A. Friedrich. Combined electrochemical and surface analysis investigation of degradation processes in polymer electrolyte membrane fuel cells. *Electrochimica Acta*, 52(6):2328 – 2336, 2007.

[28] A. Taniguchi, T. Akita, K. Yasuda, and Y. Miyazaki. Analysis of degradation in PEMFC caused by cell reversal during air starvation. *International Journal of Hydrogen Energy*, 33(9):2323 – 2329, 2008.

[29] Z. Liu, L. Yang, Z. Mao, W. Zhuge, Y. Zhang, and L. Wang. Behavior of PEMFC in starvation. *Journal of Power Sources*, 157(1):166 – 176, 2006.

[30] N. Yousfi-Steiner, Ph. Moçotéguy, D. Candusso, and D. Hissel. A review on polymer electrolyte membrane fuel cell catalyst degradation and starvation issues: Causes, consequences and diagnostic for mitigation. *Journal of Power Sources*, 194(1):130 – 145, 2009.

[31] Garland N., Benjamin T., and Kopasz J. Materials issues in polymer electrolyte membrane fuel cells. *Journal of Power Sources*, 194(1):130 – 145, 2009.

[32] Y. Shao, G. Yin, and Y. Gao. Understanding and approaches for the durability issues of Pt-based catalysts for PEM fuel cell. *Journal of Power Sources*, 171(2):558 – 566, 2007.

[33] Xingwen Yu and Siyu Ye. Recent advances in activity and durability enhancement of Pt/C catalytic cathode in PEMFC: Part II: Degradation mechanism and durability enhancement of carbon supported platinum catalyst. *Journal of Power Sources*, 172(1):145 – 154, 2007.

[34] N. F. Büchi. *Polymer Electrolyte Fuel Cell Durability*. Springer, 2009.

[35] P. W. Voorhees. The theory of ostwald ripening. *Electrochemical and Solid-State Letters*, 9(4):A183, 1985.

[36] T. W. Patterson and R. M. Darling. Damage to the cathode catalyst of a PEM fuel cell caused by localized fuel starvation. *Electrochemical and Solid-State Letters*, 9(4):A183, 2006.

[37] R. M. Darling and J. P. Meyers. Kinetic model of platinum dissolution in PEMFCs. *Journal of The Electrochemical Society*, 150(11):A1523, 2003.

[38] R. M. Darling and J. P. Meyers. Mathematical model of platinum movement in PEM fuel cells. *Journal of The Electrochemical Society*, 152(1):A242, 2005.

[39] K. J.J. Mayrhofer, J. C. Meier, S. J. Ashton, G. K.H. Wiberg, F. Kraus, M. Hanzlik, and M. Arenz. Fuel cell catalyst degradation on the nanoscale. *Electrochemistry Communications*, 10(8):1144 – 1147, 2008.

[40] A. V. Virkar and Y. Zhou. Mechanism of catalyst degradation in proton exchange membrane fuel cells. *Electrochemical and Solid-State Letters*, 10(5):B101, 2007.

[41] E. Guilminot, A. Corcella, F. Charlot, F. Maillard, and M. Chatenet. Detection of Pt ions and Pt nanoparticles inside the membrane of a used PEMFC. *Journal of The Electrochemical Society*, 154(1):B96, 2007.

[42] W. Bi, G. E. Gray, and T. F. Fuller. PEM fuel cell pt c dissolution and deposition in nafion electrolyte. *Electrochemical and Solid-State Letters*, 10(5):B101, 2007.

[43] T. W. Patterson and R. M. Darling. Damage to the cathode catalyst of a PEM fuel cell caused by localized fuel starvation. *Electrochemical and Solid-State Letters*, 9(4):A183, 2006.

[44] D. A. Stevens, M. T. Hicks, G. M. Haugen, and J. R. Dahn. Ex situ and in situ stability studies of PEMFC catalysts. *Journal of The Electrochemical Society*, 152(12):A2309, 2005.

[45] L. M. Roen, C. H. Paik, and T. D. Jarvi. Electrocatalytic corrosion of carbon support in PEMFC cathodes. *Electrochemical and Solid-State Letters*, 7(1):A19, 2004.

[46] C. A. Reiser, L. Bregoli, T. W. Patterson, J. S. Yi, J. D. Yang, M. L. Perry, and T. D. Jarvi. A reverse-current decay mechanism for fuel cells. *Electrochemical and Solid-State Letters*, 8(6):A273, 2005.

[47] J. P. Meyers and R. M. Darling. Model of carbon corrosion in PEM fuel cells. *Journal of The Electrochemical Society*, 153(8):A1432, 2006.

[48] M. L. Perry, T. Patterson, and C. Reiser. Systems strategies to mitigate carbon corrosion in fuel cells. *ECS Transactions*, 3(1):783–795, 2019.

[49] K. D. Kreuer, S. Paddison, E. Spoh, and M. Schuster. Transport in proton conductors for fuel-cell applications: Simulations, elementary reactions, and phenomenology. *Chemical Reviews*, 104(14):4637–78, 2004.

[50] A. K. Mauritz and R. B Moore. State of understanding of nafion. *Chemical Reviews*, 104(10):4535–85, 2004.

[51] M. Cappadonia, J.W. Erning, and U. Stimming. Proton conduction of Nafion 117 membrane between 140 K and room temperature. *Journal of Electroanalytical Chemistry*, 376(1):189 – 193, 1994.

[52] A. S. Davydov. *Solitons in Molecular Systems*. Dordrecht London, 1991.

[53] G. Gebel, P. Aldebert, and M. Pineri. Swelling study of perfluorosulphonated ionomer membranes. *Polymer*, 34(2):333–339, 1993.

[54] T. Kinumoto, M. Inaba, Y. Nakayama, K. Ogata, R. Umebayashi, A. Tasaka, Y. Iriyama, T. Abe, and Z. Ogumi. Durability of perfluorinated ionomer membrane against hydrogen peroxide. *Journal of Power Sources*, 158(2):1222 – 1228, 2006.

[55] A. Laconti, H. Liu, C. Mittelsteadt, and R. McDonald. Polymer electrolyte membrane degradation mechanisms in fuel cells - findings over the past 30 years and comparison with electrolyzers. *ECS Transactions*, 1(8):199–219, dec 2019.

[56] V. Mittal, H. R. Kunz, and J. M. Fenton. Membrane degradation mechanisms in PEMFCs. *ECS Transactions*, 3(1):507–517, dec 2019.

[57] N. Miyake, M. Wakizoe, E. Honda, and T. Ohta. High durability of asahi kasei aciplex membrane. *ECS Transactions*, 1(8):249–261, dec 2019.

[58] A. Kusoglu, A. M. Karlsson, M. H. Santare, S. Cleghorn, and W. B. Johnson. Mechanical response of fuel cell membranes subjected to a hygro-thermal cycle. *Journal of Power Sources*, 161(2):987 – 996, 2006.

[59] A. Kusoglu, A. M. Karlsson, M. H. Santare, S. Cleghorn, and W. B. Johnson. Mechanical behavior of fuel cell membranes under humidity cycles and effect of swelling anisotropy on the fatigue stresses. *Journal of Power Sources*, 170(2):345 – 358, 2007.

[60] J. Yu, T. Matsuura, Y. Yoshikawaand, M. Nazrul Islam, and M. Hori. Lifetime behavior of a PEM fuel cell with low humidification of feed stream. *Phys. Chem. Chem. Phys.*, 7:373–378, 2005.

[61] C. Chen and T. F. Fuller. The effect of humidity on the degradation of nafion membrane. *Polymer Degradation and Stability*, 94(9):1436 – 1447, 2009.

[62] D. Natarajan and T. Van Nguyen. Current distribution in PEM fuel cells. part 1: Oxygen and fuel flow rate effects. *AIChE Journal*, 51(9):2587–2598, 2005.

[63] B. Wahdame, D. Candusso, X. François, F. Harel, M. C. Péra, D. Hissel, and J. M. Kauffmann. Comparison between two PEM fuel cell durability tests performed at constant current and under solicitations linked to transport mission profile. *International Journal of Hydrogen Energy*, 32(17):4523 – 4536, 2007.

[64] M. Bodner, A. Schenk, D. Salaberger, M. Rami, C. Hochenauer, and V. Hacker. Air starvation induced degradation in polymer electrolyte fuel cells. *Fuel Cells*, 17(1):18–26, 2017.

[65] J. J. Baschuk and X. Li. Modelling CO poisoning and O2 bleeding in a PEM fuel cell anode. *International Journal of Energy Research*, 27(12):1095–1116, 2003.

[66] H.S. Chu, C.P. Wang, W.C. Liao, and W.M. Yan. Transient behavior of co poisoning of the anode catalyst layer of a PEM fuel cell. *Journal of Power Sources*, 159(2):1071 – 1077, 2006.

[67] L. Y. Sung, B. J. Hwang, K. L. Hsueh, and F. H. Tsau. Effects of anode air bleeding on the performance of co poisoned proton exchange membrane fuel cells. *Journal of Power Sources*, 195(6):1630 – 1639, 2010.

[68] H. Li, C. Song, J. Zhang, and J. Zhang. *Catalyst Contamination in PEM Fuel Cells*, pages 331–354. Springer London, London, 2008.

[69] R. Halseid, P. J.S. Vie, and R. Tunold. Effect of ammonia on the performance of polymer electrolyte membrane fuel cells. *Journal of Power Sources*, 154(2):343 – 350, 2006.

[70] R. Mohtadi, W. K. Lee, and J.W. Van Zee. Assessing durability of cathodes exposed to common air impurities. *Journal of Power Sources*, 138(1):216 – 225, 2004.

[71] G. Hinds. In situ diagnostics for polymer electrolyte membrane fuel cells. *Current Opinion in Electrochemistry*, 5(1):11 – 19, 2017.

[72] T. Mennola, M. Mikkola, M. Noponen, T. Hottinen, and P. Lund. Measurement of ohmic voltage losses in individual cells of a PEMFC stack. *Journal of Power Sources*, 112(1):261 – 272, 2002.

[73] X. Yuan, H. Wang, J. C. Sun, and J. Zhang. Ac impedance technique in PEM fuel cell diagnosis - a review. *Internationa Journal of Hydrogen Energy*, 32(7):4365 – 4380, 2007.

[74] S. M. Rezaei Niya and M. Hoorfar. Study of proton exchange membrane fuel cells using electrochemical impedance spectroscopy technique - a review. *Journal of Power Sources*, 240(8):281 – 293, 2013.

[75] C. Gabrielli. *Identification of electrochemical processes by frequency response analysis*. Schlumberger Farnborough, 1980.

[76] M. Orazem and B. Tribollet. *Electrochemical impedance spectroscopy*. Wiley, 2008.

[77] Andrea Baricci, Riccardo Mereu, Mirko Messaggi, Matteo Zago, Fabio Inzoli, and Andrea Casalegno. Application of computational fluid dynamics to the analysis of geometrical features in PEM fuel cells flow fields with the aid of impedance spectroscopy. *Applied Energy*, 205:670 – 682, 2017.

[78] Xiaohui Yan, Cheng Guan, Yao Zhang, Kaicheng Jiang, Guanghua Wei, Xiaojing Cheng, Shuiyun Shen, and Junliang Zhang. Flow field design with 3D geometry for proton exchange membrane fuel cells. *Applied Thermal Engineering*, 147:1107 – 1114, 2019.

[79] Y. Bultel, K. Wiezell, F. Jaouen, P. Ozil, and G. Lindbergh. Investigation of mass transport in gas diffusion layer at the air cathode of a pemfc. *Electrochimica Acta*, 51(3):474 – 488, 2005.

[80] R. W. Atkinson, J. A. Rodgers, M. W. Hazard, R. O. Stroman, and B. D. Gould. Influence of cathode gas diffusion media porosity on open-cathode fuel cells. *Journal of The Electrochemical Society*, 165(11):F1002–F1011, 2018.

[81] J. Ihonen, M. Mikkola, and G. Lindbergh. Flooding of gas diffusion backing in PEFCs. *Journal of The Electrochemical Society*, 151(8):A1152, 2004.

[82] Y. Liu, C. Ji, W. Gu, D. R. Baker, J. Jorne, and H. A. Gasteiger. Proton conduction in PEM fuel cell cathodes: Effects of electrode thickness and ionomer equivalent weight. *Journal of The Electrochemical Society*, 157(8):B1154, 2010.

[83] Y. C. Lai, K. L. Huang, C. H. Tsai, W. J. Lee, and Y. L. Chen. Sputtered Pt loadings of membrane electrode assemblies in proton exchange membrane fuel cells. *International Journal of Energy Research*, 36(8):918–927, 2012.

[84] R. B. Moghaddam and E. B. Easton. Impedance spectroscopy assessment of catalyst coated nafion assemblies for proton exchange membrane fuel cells. *Electrochimica Acta*, 292:292 – 298, 2018.

[85] M. A. Haque, A. B. Sulong, R. E. Rosli, E. H. Majlan, L. K. Shyuan, and M. A. A. Mashud. Measurement of hydrogen ion conductivity through proton exchange membrane. In *2015 IEEE International WIE Conference on Electrical and Computer Engineering (WIECON-ECE)*, pages 552–555, 2015.

[86] E. E. Abdel-Hady, M. O. Abdel-Hamed, S. Awad, and M.F.M. Hmamm. Characterization and evaluation of commercial poly (vinylidene fluoride)-g-sulfonatedpolystyrene as proton exchange membrane. *Polymers for Advanced Technologies*, 29(1):130–142, 2018.

[87] F. Ciucci. Modeling electrochemical impedance spectroscopy. *Current Opinion in Electrochemistry*, 13:132 – 139, 2019.

[88] G. Li and P. G. Pickup. Ionic conductivity of PEMFC electrodes. *Journal of the Electrochemical Society*, 150(11):C745, 2003.

[89] E. B. Easton and P. G. Pickup. An electrochemical impedance spectroscopy study of fuel cell electrodes. *Electrochimica Acta*, 50(12):2469 – 2474, 2005.

[90] R. Petrone, Z. Zheng, D. Hissel, M.C. PÃ©ra, C. Pianese, M. Sorrentino, M. Becherif, and N. Yousfi-Steiner. A review on model-based diagnosis methodologies for PEMFCs. *International Journal of Hydrogen Energy*, 38(17):7077 – 7091, 2013.

[91] N. Fouquet, C. Doulet, C. Nouillant, G. Dauphin-Tanguy, and B. Ould-Bouamama. Model based PEM fuel cell state-of-health monitoring via ac impedance measurements. *Journal of Power Sources*, 159(2):905 – 913, 2006.

[92] A. Narjiss, D. Depernet, D. Candusso, F. Gustin, and D. Hissel. Online diagnosis of pem fuel cell. *2008 13th International Power Electronics and Motion Control Conference*, 1(1):734–739, 2008.

[93] A. Z. Weber, R. L. Borup, R. M. Darling, P. K. Das, T. J. Dursch, W. Gu, D. Harvey, A. Kusoglu, S. Litster, M. M. Mench, R. Mukundan, J. P. Owejan, J. G. Pharoah, M. Secanell, and I. V. Zenyuk. A critical review of modeling transport phenomena in polymer-electrolyte fuel cells. *Journal of The Electrochemical Society*, 161(12):F1254–F1299, 2014.

[94] S. Chevalier, B. Auvity, J. C. Olivier, C. Josset, D. Trichet, and M. Machmoum. Detection of cells state-of-health in PEM fuel cell stack using EIS measurements coupled with multiphysics modeling. *Fuel Cells*, 14(3):416–429, 2014.

[95] T. E. Springer. Characterization of polymer electrolyte fuel cells using AC impedance spectroscopy. *Journal of The Electrochemical Society*, 143(2):587, 1996.

[96] V. A. Paganin, C. L. F. Oliveira, E. A. Ticianelli, T. E. Springer, and E. R. Gonzalez. Modelistic interpretation of the impedance response of a polymer electrolyte fuel cell. *Electrochimica Acta*, 43(24):3761 – 3766, 1998.

[97] M. Ciurenau and R. Roberge. Parameter identifiability analysis and visualization in large-scale kinetic models of biosystems. *Journal of Physical Chemistry B*, 105(17):3531 – 3539, 2001.

[98] N. Holmström, K. Wiezell, and G. Lindbergh. Studying low humidity effects in PEMFCS using EIS experiments. *Journal of The Electrochemical Society*, 159(8):F369–F378, 2012.

[99] A. Parthasarathy. The platinum microelectrode/nafion interface: An electrochemical impedance spectroscopic analysis of oxygen reduction kinetics and nafion characteristics. *Journal of The Electrochemical Society*, 139(6):1634, 1992.

[100] P. Kurzweil and H. J. Fischle. A new monitoring method for electrochemical aggregates by impedance spectroscopy. *Journal of Power Sources*, 127(1):331 – 340, 2004.

[101] T. Soboleva, Z. Xie, Z. Shi, E. Tsang, T. Navessin, and S. Holdcroft. Investigation of the through-plane impedance technique for evaluation of anisotropy of proton conducting polymer membranes. *Journal of Electroanalytical Chemistry*, 622(2):145 – 152, 2008.

[102] M. F. Mathias and S. A. Grot. System and method for controlling humidity level of a fuel cell, U.S. Patent 6376111B1, 1990.

[103] I. Nitta, O. Himanen, and M. Mikkola. Contact resistance between gas diffusion layer and catalyst layer of PEM fuel cell. *Electrochemistry Communications*, 10(1):47 – 51, 2008.

[104] S. Asghari, A. Mokmeli, and M. Samavati. Study of PEM fuel cell performance by electrochemical impedance spectroscopy. *International Journal of Hydrogen Energy*, 35(17):9283 – 9290, 2010.

[105] F. A. Uribe, S. Gottesfeld, and T. A. Zawodzinski. Effect of ammonia as potential fuel impurity on proton exchange membrane fuel cell performance. *Journal of The Electrochemical Society*, 149(3):A293, 2002.

[106] M Eikerling and A.A Kornyshev. Electrochemical impedance of the cathode catalyst layer in polymer electrolyte fuel cells. *Journal of Electroanalytical Chemistry*, 475(2):107 – 123, 1999.

[107] M. C. Lefebvre. Characterization of ionic conductivity profiles within proton exchange membrane fuel cell gas diffusion electrodes by impedance spectroscopy. *Electrochemical and Solid-State Letters*, 2(6):259, 1999.

[108] R. Makharia, M. F. Mathias, and D. R. Baker. Measurement of catalyst layer electrolyte resistance in PEFCs using electrochemical impedance spectroscopy. *Journal of The Electrochemical Society*, 152(5):A970, 2005.

[109] M. Cimenti, D. Bessarabov, M. Tam, and J. Stumper. Investigation of proton transport in the catalyst layer of PEM fuel cells by electrochemical impedance spectroscopy. *ECS Transactions*, 28(23):147–157, dec 2019.

[110] H. Nara, S. Tominaka, T. Momma, and T. Osaka. Impedance analysis counting reaction distribution on degradation of cathode catalyst layer in PEFCs. *Journal of The Electrochemical Society*, 158(9):B1184, 2011.

[111] I. Pivac, D. Bezmalinovic, and F. Barbir. Catalyst degradation diagnostics of proton exchange membrane fuel cells using electrochemical impedance spectroscopy. *International Journal of Hydrogen Energy*, 43(29):13512 – 13520, 2018.

[112] H. Kuhn, A. Wokaun, and G.G. Scherer. Exploring single electrode reactions in polymer electrolyte fuel cells. *Electrochimica Acta*, 52(6):2322 – 2327, 2007.

[113] K. Wiezell, P. Gode, and G. Lindbergh. Steady-state and EIS investigations of hydrogen electrodes and membranes in polymer electrolyte fuel cells. *Journal of The Electrochemical Society*, 153(4):A749, 2006.

[114] K. Wiezell, P. Gode, and G. Lindbergh. Steady-state and EIS investigations of hydrogen electrodes and membranes in polymer electrolyte fuel cells. *Journal of The Electrochemical Society*, 153(4):A759, 2006.

[115] T. J. P. Freire and E. R. Gonzalez. Effect of membrane characteristics and humidification conditions on the impedance response of polymer electrolyte fuel cells. *Journal of Electroanalytical Chemistry*, 503(1):57 – 68, 2001.

[116] B. Andreaus, A. J. McEvoy, and G. G. Scherer. Analysis of performance losses in polymer electrolyte fuel cells at high current density by impedance spectroscopy. *Electrochimica Acta*, 47(13-14):2223 – 2229, 2002.

[117] M. Boillot, N. Jatroudakis, P. Carre, S. Didierjean, and F. Lapicque. Effect of gas dilution on PEM fuel cell performance and impedance response. *Fuel Cells*, 6(1):31 – 37, 2006.

[118] K. C. Neyerlin, H. A. Gasteiger, C. K. Mittelsteadt, J. Jorne, and W. Gu. Effect of relative humidity on oxygen reduction kinetics in a PEMFC. *Journal of The Electrochemical Society*, 152(6):A1073, 2005.

[119] J. M. Le Canut, R. M. Abouatallah, and D. A. Harrington. Detection of membrane drying, fuel cell flooding, and anode catalyst poisoning on PEMFC stacks by electrochemical impedance spectroscopy. *Journal of The Electrochemical Society*, 153(5):A857, 2006.

[120] I. A. Schneider, D. Kramer, A. Wokaun, and G. G. Scherer. Oscillations in the gas channels - the forgotten player in impedance spectroscopy in polymer electrolyte fuel cells A. exploring the wave. *ECS Transactions*, 3(1):1001–1010, 2006.

[121] I. A. Schneider, S. A. Freunberger, D. Kramer, A. Wokaun, and G. G. Scherer. Oscillations in gas channels. *Journal of The Electrochemical Society*, 154(4):B383, 2007.

[122] I. A. Schneider, D. Kramer, A. Wokaun, and G. G. Scherer. Oscillations in gas channels. *Journal of The Electrochemical Society*, 154(8):B770, 2007.

[123] G. Maranzana, J. Mainka, O. Lottin, J. Dillet, A. Lamibrac, A. Thomas, and S. Didierjean. A proton exchange membrane fuel cell impedance model taking into account convection along the air channel: On the bias between the low frequency limit of the impedance and the slope of the polarization curve. *Electrochimica Acta*, 83:13 – 27, 2012.

[124] A.A. Kulikovsky. The effect of stoichiometric ratio on the performance of a polymer electrolyte fuel cell. *Electrochimica Acta*, 49(4):617 – 625, 2004.

[125] A. Kulikovsky and O. Shamardina. A model for PEM fuel cell impedance: Oxygen flow in the channel triggers spatial and frequency oscillations of the local impedance. *Journal of The Electrochemical Society*, 162(9):F1068–F1077, 2015.

[126] T. Kurz, A. Hakenjos, J. Kraemer, M. Zedda, and C. Agert. An impedance-based predictive control strategy for the state-of-health of pem fuel cell stacks. *Journal of Power Sources*, 180(2):742 – 747, 2008.

[127] M. Bautista, Y. Bultel, and P. Ozil. Polymer electrolyte membrane fuel cell modelling: d.c. and a.c. solutions. *Chemical Engineering Research and Design*, 82(7):907 – 917, 2004.

[128] M. Chandesris, C. Robin, M. Gerard, and Y. Bultel. Investigation of the difference between the low frequency limit of the impedance spectrum and the slope of the polarization curve. *Electrochimica Acta*, 180:581 – 590, 2015.

[129] S. Chevalier, C. Josset, A. Bazylak, and B. Auvity. Measurements of air velocities in polymer electrolyte membrane fuel cell channels using electrochemical impedance spectroscopy. *Journal of The Electrochemical Society*, 163(8):F816–F823, 2016.

[130] S. Keller, T. Oezel, A. C. Scherzer, D. Gerteisen, U. Gross, C. Hebling, and Y. Manoli. Characteristic time constants derived from low frequency arc of impedance of fuel cell stack. *Journal of the Electrochemical Energy Conversion and Storage*, 15(2):1 – 10, 2018.

[131] I. A. Schneider, M. H. Bayer, A. Wokaun, and G. G. Scherer. Impedance response of the proton exchange membrane in polymer electrolyte fuel cells. *Journal of The Electrochemical Society*, 155(8):B783, 2008.

[132] K. Wiezell, N. Holmstroem, and G. Lindbergh. Studying low humidity effects in PEMFCs using EIS modeling. *Journal of The Electrochemical Society*, 159(8):F379–F392, 2012.

[133] I. Pivac and F. Barbir. Inductive phenomena at low frequencies in impedance spectra of proton exchange membrane fuel cells: A review. *Journal of Power Sources*, 326:112 – 119, 2016.

[134] O. Antoine, Y. Bultel, and R. Durand. Oxygen reduction reaction kinetics and mechanism on platinum nanoparticles inside Nafion. *Journal of Electroanalytical Chemistry*, 499(1):85 – 94, 2001.

[135] N. M. Markovic, T. J. Schmidt, V. Stamenkovic, and P. N. Ross. Oxygen reduction reaction on Pt and Pt bimetallic surfaces: A selective review. *Fuel Cells*, 1(2):105–116, 2001.

[136] A. A. Franco and M. Tembely. Transient multiscale modeling of aging mechanisms in a PEMFC cathode. *Journal of The Electrochemical Society*, 154(7):B712, 2007.

[137] S. K. Roy, M. E. Orazem, and B. Tribollet. Interpretation of low-frequency inductive loops in PEM fuel cells. *Journal of The Electrochemical Society*, 154(12):B1378, 2007.

[138] M. Inaba, H. Yamada, J. Tokunaga, and A. Tasaka. Effect of agglomeration of Pt C catalyst on hydrogen peroxide formation. *Electrochemical and Solid-State Letters*, 7(12):A474, 2004.

[139] S. Cruz-Manzo, C. Perezmitre Cruz, P. Greenwood, and R. Chen. An impedance model for analysis of EIS of polymer electrolyte fuel cells under platinum oxidation and hydrogen peroxide formation in the cathode. *Journal of Electroanalytical Chemistry*, 771:94 – 105, 2016.

[140] N. Wagner and M. Schulze. Change of electrochemical impedance spectra during CO poisoning of the Pt and Pt Ru anodes in a membrane fuel cell (PEFC). *Electrochimica Acta*, 48(25):3899 – 3907, 2003.

[141] B. P. Setzler and T. F. Fuller. A physics-based impedance model of proton exchange membrane fuel cells exhibiting low-frequency inductive loops. *Journal of The Electrochemical Society*, 162(6):F519–F530, 2015.

[142] C. Bao and W. G. Bessler. Two dimensional modeling of a polymer electrolyte membrane fuel cell with long flow channel. part 2 physics based electrochemical impedance analysis. *Journal of Power Sources*, 278:675 – 682, 2015.

[143] C. Gabrielli and B. Tribollet. A transfer function approach for a generalized electrochemical impedance spectroscopy. *Journal of the Electrochemical Society*, 141(5):1147 – 1146, 1994.

[144] D. D. Macdonald, E. Sikora, and G. Engelhardt. Characterizing electrochemical systems in the frequency domain. *Electrochimica Acta*, 43(1):87 – 107, 1998.

[145] J. R. Collet-Lacoste. The electrochemical impedance spectroscopy and associated transfer functions: non-equilibrium thermodynamics consideration. *Electrochimica Acta*, 49(5):4967 – 4977, 2004.

[146] Z. Gajic. *Linear dynamic systems and signals*. Prentice Hall, 1980.

[147] K. S. Suresh Kumar. *Electric circuits and networks*. Pearson Education, 2008.

[148] M. Athans, P. Kapasouris, E. Kappos, and H. A. Spang. Linear-quadratic gaussian with loop-transfer recovering methodology for the F-100 engine. *Journal of Guidance Control and Dynamics*, 9(1):45 – 52, 1986.

[149] H. G. Bock, T. Carraro, W. Jäger, S. Körkel, R. Rannacher, and J. P. Sclöder. *Model based parameter estimation*. Springer, 2013.

[150] B. Sanchez, C. R. Rojas, G. Vandersteen, R. Bragos, and J. Schoukens. On the calculation of the D-optimal multi-sine excitation power spectrum for broadband impedance spectroscopy measurements. *Measurement Science and Technology*, 23:1 – 15, 2012.

[151] O. Bohnke, B. Vuillemin, C. Gabrielli, M. Keddam, H. Perrot, H. Takenouti, and R. Torresi. An electrochemical quartz crystal microbalance study of lithium insertion into thin films of tungsten trioxide I. Modeling of the ionic insertion mechanism. *Electrochimica Acta*, 40(17):2755 – 2764, 1995.

[152] C. Gabrielli, M. Keddam, F. Minouflet, and H. Perrot. Ac electrogravimetry contribution to the investigation of the anodic behaviour of iron in sulfuric medium. *Electrochimica Acta*, 41(7):1217 – 1222, 1996. Electrochemical Impendance Spectroscopy.

[153] D. Benito, C. Gabrielli, J.J. Garcia Jareno, M. Keddam, H. Perrot, and F. Vicente. An electrochemical impedance and ac electrogravimetry study of PNR films in aqueous salt media. *Electrochemistry Communications*, 4(8):613 – 619, 2002.

[154] C. Gabrielli, J.J. Garciia Jareno, M. Keddam, H. Perrot, and F. Vicente. AC electrogravimetry study to electroactive thin films. *Journal of Physical Chemistry B*, 106(1):3182 – 3191, 2002.

[155] B. Tribollet. The modulated flow at a rotating disk electrode. *Journal of Electrochemical Society*, 130(10):2016 – 2026, 1983.

[156] K. Tokuda, S. Bruckenstein, and B. Miller. The frequency response of limiting current to sinusoidal speed modulation at a rotating disk electrode. *Journal of Electrochemical Society*, 122(10):1316 – 1321, 1975.

[157] C. Deslouis and B. Tribollet. Recent developments in the electro-hydrodynamic (EHD) impedance technique. *Journal of Electroanalytical Chemistry*, 572(2):389 – 398, 2004.

[158] A. Olivier, E. Merienne, J. P. Chopart, and O. Aaboubi. Thermoelectrochemical impedances 1. A new experimental device to measure thermoelectrochemical transfer functions. *Electrochimica Acta*, 37(11):1945 – 1950, 1992.

[159] J. L. Valdes and B. Miller. Thermal modulation of rotating disk electrode: frequency and transient response. *Journal of Electrochemical Society*, 135(9):2223 – 1231, 1988.

[160] O. Aaboubi and A. Housni. Thermoelectrochemical study of silver electrodeposition from nitric and tartaric solutions. *Journal of Electroanalytical Chemistry*, 677-680:63 – 68, 2012.

[161] A. Goossens and D. D. Macdonald. A photoelectrochemical passive study of passive tungsten. *Journal of Electroanalytical Chemistry*, 352(1):65 – 81, 1993.

[162] H. Song and D. D. Macdonald. Photoelectrochemical impedance spectroscopy: validation of the transfer function by Kramers-Kronig transformation. *Journal of Electrochemical Society*, 138(5):1408 – 1410, 1991.

[163] C. Gabrielli and B. Tribollet. Analytical model for light modulating impedance spectroscopy (LIMIS) in all-solid-state p-n junction solar cells at open-circuit. *Aplied Physics Letters*, 116(1):013901, 2020.

[164] A. M. Niroumand, W. Merida, M. Eikerling, and M. Saif. Pressure voltage oscillations as a diagnostic tool for PEMFC cathodes. *Electrochemistry Communications*, 12(1):122 – 124, 2010.

[165] A. M. Niroumand, W. Merida, and M. Saif. PEM fuel cell low flow FDI. *Journal of Process Control*, 21(4):602 – 612, 2011.

[166] D. Grüebl, J. Janek, and W. G. Bessler. Electrochemical pressure impedance spectroscopy (EPIS) as diagnostic method for electrochemical cells with gaseous reactants: A model-based analysis. *Journal of The Electrochemical Society*, 163(5):A599–A610, 2016.

[167] P. Hartman, H. Sommer, D. Grüebl, J. Janek, W. Bessler, and P. Adelhem. Pressure dynamics in metal oxygen batteries. *Journal of Physical Chemistry C*, 118(3):1461 – 1471, 2014.

[168] L. Rasha, J.I.S. Cho, T.P. Neville, A. Corredera, P.R. Shearing, and D. J. L. Brett. Water distribution mapping in polymer electrolyte fuel cells using lock-in thermography. *Journal of Power Sources*, 440:227160, 2019.

[169] Y. Wu, Q. Meyer, F. Liu, L. Rasha, J.I.S. Cho, T.P. Neville, J. Millichamp, R. Ziesche, N. Kardjilov, P. Boillat, H. Markötter, I. Manke, M. Cochet, P. Shearing, and D. J. L. Brett. Investigation of water generation and accumulation in polymer electrolyte fuel cells using hydroelectrochemical impedance imaging. *Journal of Power Sources*, 414:272 – 277, 2019.

[170] A. Turhan, K. Keller, J. S. Brenizer, and M. M. Mench. Passive control of liquid water storage and distribution in a PEFC through flow field design. *Journal of Power Sources*, 180:773–783, 2008.

[171] J. Zhang, D. Kramer, R. Shimoi, Y. Ono, E. Lehmann, A. Wokaun, K. Shinohara, and G. Scherer. In situ diagnostic of two-phase flow phenomena in polymer electrolyte fuel cells by neutron imaging part b - material variations. *Electrochimica Acta*, 51:2715–2727, 2006.

[172] A. Z. Weber and J. Newman. Transport in polymer electrolyte membranes: mathematical model. *Journal of Electrochemical Society*, 51(2):A311–A325, 2005.

[173] Y. Bultel, K. Wiezell, F. Jaouen, P. Ozil, and G. Lindbergh. Investigation of mass transport in gas diffusion layer at the air cathode of PEMFC. *Electrochimica Acta*, 51:474 – 488, 2005.

[174] J. Benziger, E. Kimball, R. Mejia-Ariza, and I. Kevekidis. Oxygen mass transport limitations at the cathode of polymer electrolyte membrane fuel cells. *AIChe*, 57(9):2505–2517, 2011.

[175] M. Lindstrom and B. Wetton. A comparison of Fick and Maxwell-Stefan diffusion formulations in PEMFC gas diffusion layers. *Heat and Mass Transfer*, pages 1 – 8, 2016.

[176] D. F. Fairbanks and C. R. Wilke. Diffusion coefficients in multicomponent gas mixtures. *Chemical Engineering Progress*, 46:95 – 104, 1950.

[177] T. E. Springer, T. A. Zawodzinski, and S. Gottesfeld. Polymer electrolyte fuel cell model. *Journal of the Electrochemical Society*, 138(8):2334 – 2342, 1991.

[178] M. Eikerling, Y. I. Kharkats, A. A. Kornyshev, and Y. M. Volfkovich. Phenomenological theory of electro-osmotic effect and water management in polymer electrolyte proton-conducting membranes. *Journal of Electrochemical Society*, 145(8):2684–2699, 1998.

[179] T. F. Fuller. *PhD Thesis*. University of California, Berkeley edition, 1992.

[180] T. A. Zawodzinski, M. Neeman, L. O. Sillerud, and S. Gottesfeld. Determination of water diffusion coefficients in perfluorosulfonate ionomeric membranes. *Journal of Physical Chemistry*, 95:6040–6044, 1991.

[181] Y. Wang and C. Y. Wang. Simulation of flow and transport phenomena in a polymer electrolyte fuel cell under low-humidity operation. *Journal of Power Sources*, 147(1-2):148 – 161, 2005.

[182] J. Zhang and R. Datta. Sustained potential oscillations in proton exchange membrane fuel cell with PtRu as anode catalyst. *Journal of the Electrochemical Society*, 149(11):A1423 – A1431, 2002.

[183] R. Hanke-Rauschenbach, M. Mangold, and K. Sundmacher. Bistable current-voltage characteristics of PEM fuel cells operated with reduced feed stream humidification. *Journal of Electrochemical Society*, 155(2):B97 – B107, 2008.

[184] K. Wiezell and P. Gode G. Lindberg. Steady state and EIS investigations of hydrogen electrodes and membrane in polymer electrolyte fuel cells. *Journal of the Electrochemical Society*, 153(4):A749 – A758, 2006.

[185] J. P. Corriou. *Process control: theory and application*. Springer, 2004th edition, 2004.

[186] Roland Brun, Martin Kuehni, Hansruedi Siegrist, Willi Gujer, and Peter Reichert. Practical identifiability of ASM2D parameter systematic selection and tuning of parameter subsets. *Water Research*, 36(16):4113 – 4127, 2002.

[187] A. Gabor, A. Villaverde, and J. Banga. Parameter identifiability analysis and visualization in large-scale kinetic models of biosystems. *BMC Systems Biology*, 54(11):1 – 16, 2017.

[188] R. Pintelon and J. Schoukens. *System identification: a frequency domain approach*. Wiley-IEEE Press, 1980.

[189] K. Vanhoenacker, J. Schoukens, J. Schwevers, and D. Vaes. Summary and comparing overview of techniques for the detection of nonlinear distortion. *Proceeding of ISMA 2002*, 2:1241 – 1252, 2002.

[190] Q. Mao and U. Krewer. Total harmonic distortion analysis of oxygen reduction reaction in proton exchange membrane fuel cells. *Electrochimica Acta*, 103:188 – 198, 2013.

[191] J. J. Giner-Sanz, E. M. Ortega, and V. Perez-Herranz. Total harmonic distortion based method for linearity assessment in electrochemical system in the contest of EIS. *Electrochimica Acta*, 186:598 – 612, 2015.

[192] T. Kadyk, R. Hanke-Rauschenbach, and K. Sundmacher. Nonlinear frequency response analysis of PEM fuel cells for diagnosis of dehydration, flooding and co-poisoning. *Journal of Electroanalytica Chemistry*, 630:19 – 27, 2009.

[193] O. S. Wolfbeis. Luminescent sensing and imaging of oxygen: Fierce competition to the Clark electrode. *BioEssays*, 37(8):921–928, 2015.

[194] R. Vetter and J. O. Schumacher. Experimental parameter uncertainty in proton exchange membrane fuel cell modeling. part I: Scatter in material parameterization. *Journal of Power Sources*, 438:227018, Oct 2019.

[195] R. Vetter and J. O. Schumacher. Experimental parameter uncertainty in proton exchange membrane fuel cell modeling. part II: Sensitivity analysis and importance ranking. *Journal of Power Sources*, 439:126529, 2019.

[196] W. Cohen and E. T. Johnson. Dynamic characteristics of double pipe heat exchangers. *Industrial Engineering Chemistry*, 48(6):1031 – 1034, 1956.

[197] T. Z. Fahidy. Frequency response of plug-flow electrochemical reactors. *Journal of The Electrochemical Society*, 132(7):1575, 1985.

[198] A. Sorrentino, T. Vidakovic-Koch, R. Hanke-Rauschenbach, and K. Sundmacher. Concentration-alternating frequency response: A new method for studying polymer electrolyte membrane fuel cell dynamics. *Electrochimica Acta*, 243:53 – 64, 2017.

[199] A. Sorrentino, T. Vidakovic-Koch, and K. Sundmacher. Studying mass transport dynamics in polymer electrolyte membrane fuel cells using concentration-alternating frequency response analysis. *Journal of Power Sources*, 412:331 – 335, 2019.

[200] A. Sorrentino, K. Sundmacher, and T. Vidakovic-Koch. Guide to concentration alternating frequency response analysis of fuel cells. *Journal of Visualized Experiments*, 154(1-2):e60129, 2019.

[201] A. Sorrentino, K. Sundmacher, and T. Vidakovic-Koch. Polymer electrolyte fuel cell degradation mechanisms and their diagnosis by frequency response analysis methods: a review. *Energy*, 13(21):5825, 2020.

[202] A. Sorrentino, K. Sundmacher, and T. Vidakovic-Koch. Decoupling PEMFC dynamics through frequency response analysis based on concentration inputs. *Electrochimica Acta*, 390:53, 2021.

[203] A. Sorrentino, T. Vidakovic-Koch, R. Hanke-Rauschenbach, and K. Sundmacher. Concentration-induced electrochemical impedance spectroscopy (cEIS) for the analysis of PEM fuel cells. European Congress of Chemical Engineering, Nice, France, 27 September - 2 October 2015. (Oral Presentation).

[204] A. Sorrentino, T. Vidakovic-Koch, and K. Sundmacher. Concentration frequency response analysis: a new method for the study of the dynamics in PEM fuel cells. International Symposium on Electrochemical Impedance Spectroscopy, A Toxa, Spain, 19 - 24 June 2016. (Oral Presentation).

[205] A. Sorrentino, T. Vidakovic-Koch, and K. Sundmacher. Studying mass transport dynamics in PEMFCs using concentration-alternating frequency response analysis. Annual Meeting of the International Electrochemical Society, Bologna, Italy, 2 - 7 September 2018. (Poster).

[206] A. Sorrentino, K. Sundmacher, and T. Vidakovic-Koch. Concentration-alternating frequency response analysis: a tool to unravel the complex dynamics of PEMFCs. Symposium on Modeling and Experimental Validation of Electrochemical Energy Technology, Braunschweig, Germany, 12 - 13 March 2019. (Poster).

[207] A. Sorrentino, K. Sundmacher, and T. Vidakovic-Koch. Concentration-alternating frequency response analysis of polymer electrolyte fuel cells: experimental validations. International Symposium on Electrochemical Impedance Spectroscopy, Lege Cap Ferret, France, 2 - 7 June 2019. (Oral Presentation).

[208] A. Sorrentino, K. Sundmacher, and T. Vidakovic-Koch. System identification of PEMFCs through EIS and cFRA: a comparative study. Annual Meeting of the International Electrochemical Society, Belgrade, Serbia, 30 August - 4 September 2020. (Poster).

Publications and statements of authorship

Journal Articles

A. Sorrentino, T. Vidakovic-Koch, R. Hanke-Rauschenbach, and K. Sundmacher. Concentration-alternating frequency response: A new method for studying polymer electrolyte membrane fuel cell dynamics. *Electrochimica Acta*, 243:53 – 64, 2017.
Antonio Sorrentino developed the model, carried out the simulations, analyzed the results and wrote the paper.

A. Sorrentino, T. Vidakovic-Koch, and K. Sundmacher. Studying mass transport dynamics in polymer electrolyte membrane fuel cells using concentration-alternating frequency response analysis. *Journal of Power Sources*, 412:331 – 335, 2019.
Antonio Sorrentino designed the experimental setup, performed the experiments, carried out the simulations, analyzed the results and wrote the paper.

A. Sorrentino, K. Sundmacher, and T. Vidakovic-Koch. Guide to concentration alternating frequency response analysis of fuel cells. *Journal of Visualized Experiments*, 154(1-2):e60129, 2019.
Antonio Sorrentino designed the experimental setup, performed the experiments, and wrote the paper.

A. Sorrentino, K. Sundmacher, and T. Vidakovic-Koch. Polymer electrolyte fuel cell degradation mechanisms and their diagnosis by frequency response analysis methods: a review. *Energy*, 13(21):5825, 2020.
Antonio Sorrentino made the literature research and wrote the paper.

A. Sorrentino, K. Sundmacher, and T. Vidakovic-Koch. Decoupling PEMFC dynamics through frequency response analysis based on concentration inputs. *Electrochimica Acta*, 390:53, 2021.
Antonio Sorrentino designed the experimental setup, performed the experiments, carried out the simulations, analyzed the data and wrote the paper.

Conference Talks and Posters

1 A. Sorrentino, T. Vidakovic-Koch, R. Hanke-Rauschenbach, and K. Sundmacher. Concentration-induced electrochemical impedance spectroscopy (cEIS) for the analysis of PEM fuel cells. European Congress of Chemical Engineering, Nice, France, 27 September - 2 October 2015. (Oral Presentation)

A. Sorrentino, T. Vidakovic-Koch, and K. Sundmacher. Concentration frequency response analysis: a new method for the study of the dynamics in PEM fuel cells. International Symposium on Electrochemical Impedance Spectroscopy, A Toxa, Spain, 19 - 24 June 2016. (Oral Presentation)

A. Sorrentino, T. Vidakovic-Koch, and K. Sundmacher. Studying mass transport dynamics in PEMFCs using concentration-alternating frequency response analysis. Annual Meeting of the International Electrochemical Society, Bologna, Italy, 2 - 7 September 2018. (Poster)

A. Sorrentino, K. Sundmacher, and T. Vidakovic-Koch. Concentration-alternating frequency response analysis: a tool to unravel the complex dynamics of PEM-FCs. Symposium on Modeling and Experimental Validation of Electrochemical Energy Technology, Braunschweig, Germany, 12 - 13 March 2019. (Poster)

A. Sorrentino, K. Sundmacher, and T. Vidakovic-Koch. Concentration-alternating frequency response analysis of polymer electrolyte fuel cells: experimental validations. International Symposium on Electrochemical Impedance Spectroscopy, Lege Cap Ferret, France, 2 - 7 June 2019. (Oral Presentation)

A. Sorrentino, K. Sundmacher, and T. Vidakovic-Koch. System identification of PEMFCs through EIS and cFRA: a comparative study. Annual Meeting of the International Electrochemical Society, Belgrade, Serbia, 30 August - 4 September 2020. (Poster)